2007

Computing and analyzing gravitational radiation in black hole simulations using a new multi-block approach to numerical relativity

Ernst Nils Dorband
Louisiana State University and Agricultural and Mechanical College, dorband@cct.lsu.edu

COMPUTING AND ANALYZING GRAVITATIONAL RADIATION IN BLACK HOLE SIMULATIONS USING A NEW MULTI-BLOCK APPROACH TO NUMERICAL RELATIVITY

A Dissertation

Submitted to the Graduate Faculty of the
Louisiana State University and
Agricultural and Mechanical College
in partial fulfillment of the
requirements for the degree of
Doctor of Philosophy

in

The Department of Physics and Astronomy

by
Ernst Nils Dorband
Vordiplom, Julius-Maximilians-Universität, Würzburg, 1999
M.S., Rutgers - The State University of New Jersey, 2001
May 2007

Acknowledgements

I want to thank my adviser Manuel Tiglio. With his deep knowledge of physics and numerical analysis, he gave me a whole new perspective about numerical relativity. He always took his time to discuss projects and problems and motivated me to go on during occasionally frustrating times. Over the last years, he became a precious friend.

Regards go to Ed Seidel who supported me since I first started to work in the field and pulled a lot of strings in the background to make my move to Louisiana possible.

I am grateful to my parents Monika and Immo for everything they do for me, which is more than would fit on this page.

Thanks to my lovely girlfriend Jee Yeoun. You were always there for me and made my final year in Baton Rouge a very special one.

A work like this can only be done within a strong collaboration and I was lucky to work closely together with many talented scientists. I explicitly want to mention Emanuele Berti, Peter Diener, Alessandro Nagar, Carlos Palenzuela, Enrique Pazos and Erik Schnetter. Thanks to all of them for contributing to the research presented here.

I thank Steve Brandt, Vitor Cardoso, Mark Carpenter, Barrett Deris, Heinz-Otto Kreiss, Luis Lehner, José M. Martín-García, Ken Mattsson, Frank Muldoon, Harald Pfeiffer, Jorge Pullin, Olivier Sarbach, Magnus Svärd, Saul Teukolsky, Jonathan Thornburg and Burkhard Zink for many helpful discussions and suggestions.

Special thanks go to Jorge Pullin for help with organizational issues at the department of physics and to Bernd Brügmann, who introduced me to the field of numerical relativity back in 2001.

I want to acknowledge Saul Teukolsky and the relativity group at Cornell University for their hospitality. Some crucial parts of this work were accomplished during a number of research retreats that were held there.

This research was supported in part by NSF grants PHY-0505761, PHY-0244699, PHY-0326311, PHY-0554793, NASA grant NAG5-1430, and the National Center for Supercomputer Applications grant MCA02N014 to Louisiana State University. It also employed the resources

of the Center for Computation & Technology at Louisiana State University, which is supported by funding from the Louisiana legislature's Information Technology Initiative.

The numerical calculations used the Cactus framework [1, 2] with a number of locally developed thorns, the LAPACK [3] and BLAS [4] libraries from the Netlib Repository [5], and the LAM [6, 7, 8] and MPICH [9, 10, 11] MPI [12] implementations.

Table of Contents

Abstract

Numerical simulations of Kerr black holes are presented and the excitation of quasinormal modes is studied in detail. Issues concerning the extraction of gravitational waves from numerical space-times and analyzing them in a systematic way are discussed.

A new multi-block infrastructure for solving first order symmetric hyperbolic time dependent partial differential equations is developed and implemented in a way that stability is guaranteed for arbitrary high order accurate numerical schemes. Multi-block methods make use of several coordinate patches to cover a computational domain. This provides efficient, flexible and very accurate numerical schemes.

Using this code, three dimensional simulations of perturbed Kerr black holes are carried out. While the quasinormal frequencies for such sources are well known, until now little attention has been payed to the relative excitation strength of different modes. If an actual perturbed Kerr black hole emits two distinct quasinormal modes that are strong enough to be detected by gravitational wave observatories, these two modes can be used to test the Kerr nature of the source. This would provide a strong test of the so called no hair theorem of general relativity. A systematic method for analyzing ringdown waveforms is proposed. The so called *time shift problem*, an ambiguity in the definition of excitation amplitudes, is identified and it is shown that this problem can be avoided by looking at appropriately chosen *relative* mode amplitudes. Rotational mode coupling, the relative excitation strength of co- and counter rotating modes and overtones for slowly and rapidly spinning Kerr black holes are studied.

A method for extracting waves from numerical space-times which generalizes one of the standard methods based on the Regge-Wheeler-Zerilli perturbation formalism is presented. Applying this to evolutions of single perturbed Schwarzschild black holes, the accuracy of the new method is compared to the standard approach and it is found that the errors resulting from the former are one to several orders of magnitude below the ones from the latter. It is demonstrated that even at large extraction radii ($r = 80M$), the

standard extraction approach produces errors that are dominantly of systematic nature and not due to numerical inaccuracies.

1 Introduction

1.1 Background and Outline

Gravitational wave astronomy – the detection and systematic observation of gravitational waves – has the potential to open a new window to our universe. Einstein's theory of general relativity [13, 14], which is the standard theory of gravity today, postulates that the gravitational interaction between two masses acts with finite speed, the velocity of light. This is one of the fundamental differences to Newtonian gravity for which the gravitational field generated by a mass changes instantaneously everywhere in the universe if the mass is for example accelerated. A related consequence of general relativity is the existence of gravitational waves. If a massive body is accelerated, it will generate fluctuations in space-time that propagate as waves with the speed of light. These waves transport energy and will therefore reduce the energy content of their source. For example a binary star systems binding energy is dissipated via gravitational radiation, with the effect of a shrinking orbital radius.

Gravitational waves have the remarkable property that due to their weak interaction with all known matter, they do not get absorbed or scattered significantly as they propagate through the universe. This makes them interesting for answering questions in cosmology about very distant objects. The generation of gravitational waves is fundamentally different from generation of electromagnetic radiation, on which virtually all astronomical observations are based today. Therefore it is expected that formerly unobservable astronomical processes will become visible, if gravity waves can be systematically observed and interpreted.

With gravitational wave observatories like LIGO now operating at design sensitivity [15] and more sensitive next generation detectors like advanced LIGO or the space based LISA [16] in planning, chances are good that first detections will be possible during the next decade. This progress causes an increased interest in numerical relativity.

Numerical relativity is a discipline of gravitational physics that attempts to solve the Einstein equations numerically. Its importance is due to the very limited number of closed analytic solutions to the non-linear but also to linearized Einstein equations, especially solutions that describe actual astrophysically interesting systems. One of its primary goals in the context of gravitational wave physics is to provide waveform templates that will help to filter actual signals out of the background noise in the data streams from the observatories. It also tries to give some insight into the physical properties of the sources that could become observable. Typical questions are how, for a given source, the spectrum of the radiation would look like and how it depends on physical parameters of the source or how much energy, linear and angular momentum is radiated. The hope is that numerical relativity will help to understand what processes will generate what kind of waveforms.

There are numerous possible sources for detectable gravitational waves. Among them are binary neutron star or black hole systems that inspiral and finally merge due to binding energy carried away by gravitational radiation, stellar collapse and supernovae explosions.

A long standing project in numerical relativity is to solve the two body problem, i.e. the final orbits and the merger of two black holes, a process that is among the strongest expected sources of gravitational waves and therefore a likely candidate for detection. This turned out to be an extremely complicated problem that requires very specific formulations of the Einstein equations, well chosen coordinate conditions and large amounts of computational resources. Contrary to Newtonian physics, there are no analytic solutions to this problem.

This thesis attempts to shine some light on how to extract physical relevant information from simulations like this by looking at some issues concerning gravitational radiation: What is the spectrum of certain types of sources, how strong is the presence of different modes and how accurately can gravitational waves be computed from numerical data. These questions are difficult to pose in an unambiguous way since the answers will depend

on details of the physical model and the numerical methods. Therefore a very specific test case namely a single perturbed Kerr black hole is studied. While the complexity involved in for example binary black hole simulations is avoided, looking at single black holes gives answers that are still relevant for more general situations. The argument is that the end product of a binary black hole or black hole - neutron star collision always is a single perturbed black hole. Perturbed black holes emit gravitational waves with a characteristic spectrum that is composed of the so called quasinormal modes. A consequence of the so called no-hair theorem of general relativity is that the frequencies of these modes depend only on the black hole parameters, namely the mass, the spin and the electrical charge, where the latter is not expected to play a role for astrophysical relevant objects, which are generally expected to be electrically neutral [17]. The existence of quasinormal modes makes perturbed black holes very interesting for observations, since one can in principle extract the physical quantities of the black hole by analyzing the spectrum (see introduction to Chap. 4).

For the computational work presented here, a new multi-block infrastructure for numerical relativity was developed, which allows to cover the computational domain with several non-singular coordinate patches. This is analogous to differential geometry that in general has to use multiple patches to define a regular coordinate system for a whole manifold. One of the original motivations for multi-block methods was that they allow for domains with smooth, especially spherical, boundaries in finite differencing and spectral simulations. Also non-trivial topologies can be realized with them. It turns out though that for the work presented here, the main advantage of multi-block is that it makes the use of coordinates possible, that are well adapted to the physics that is modeled. Compared to methods based on Cartesian grids, this makes three dimensional simulations of single black holes computational more efficient in terms of performance and memory requirements and simplifies wave extraction algorithms. High order (up to order eight) accurate finite differencing operators were implemented and applied in a way that numerical

stability is guaranteed. The infrastructure was realized using the Cactus computational toolkit [18] and extending Carpet [19], a driver for Cactus. This choice ensures that the new code is modular, efficient and flexible.

The single perturbed black hole simulations shown in this thesis are only a first step in using multi-block methods for numerical relativity. The infrastructure is general enough that it can handle more complicated physical situations. Attempts to use it for binary black hole simulations are undertaken currently.

This thesis is organized as follows. In Chap. 2 a description of the newly developed and implemented numerical methods is given. These include an infrastructure for doing multi-block simulations (Chap. 2.2), inter block boundary conditions (Chap. 2.3.2), high order accurate finite differencing operators (Chap. 2.3) and time integration (Chap. 2.4).

In Chap. 3 accuracy and convergence of the methods described in Chap. 2 are tested in actual non-trivial numerical simulations.

Chap. 4 is a thorough numerical study of the quasinormal mode excitation for scalar perturbations of Kerr black holes. A systematic way of extracting physical quantities like quasinormal frequencies and excitation strength from numerical waveforms in a very accurate manner is proposed. Rotational mode mixing, relative excitation amplitudes of co- and counter-rotating modes and extraction of overtones for rapidly spinning black holes is studied in detail.

In Chap. 5 different wave extraction methods for numerical space-times are described and the question is raised, how far an observer has to be located from the black hole to obtain a certain accuracy in the waveform. This is done by solving the full non-linear field equations in a generalized harmonic formulation. Initial data that represent a single perturbed Schwarzschild black hole are evolved. These initial data are constructed in a way that they satisfy the linearized constraints. The wave extraction methods used are all based on the Regge-Wheeler (RW) formalism, and the comparison is done between the standard RW extraction using different assumptions about the background space-time

and a new generalized approach that allows for a more general form of the background metric. The multi-block technique is especially well suited for such tests since, due to its efficiency, waves can be extracted at larger radii than it is possible with current state of the art mesh refinement codes. It is shown that standard assumptions about the background metric produce errors in the extracted waveforms which are larger than the numerical ones.

Detailed introductions to each of these topics are given in the beginning of the corresponding chapters.

1.2 Notation and Conventions

Unless explicitly mentioned otherwise, the following notation is used throughout this thesis:

Abstract index notation is used for vectors and tensors. The number of indices indicates the rank of a tensor, lower indices denote covariant and upper indices contravariant components. Greek indices $(\mu, \nu, ...)$ are used for four dimensional objects and run from 0 to 3. The index value 0 typically labels a time like and (1,2,3) space like directions. Latin indices $(i, j, ...)$ label components of three dimensional purely space like objects and run from 1 to 3. In places where four and three dimensional objects can be confused easily, the latter are sometimes marked by an additional superscript $^{(3)}$ in front of the corresponding symbol. The four dimensional metric is denoted by $g_{\mu\nu}$, the three dimensional one intrinsic to a space-like hypersurface by γ_{ij}.

Throughout this thesis, frequent use of Einsteins summation convention is made: if the same index appears twice in the same term, once as a lower and once as an upper index, summation over this index is implied. For example $A^i B_i = \sum_{i=1}^{3} A^i B_i$. The range of the summation should be obvious from the context. Most of the time, Greek indices are summed from 0 to 3 and Latin indices from 1 to 3.

Partial and covariant derivative operators are represented by the standard symbols ∂ and ∇ respectively. Discrete derivative operators (finite differencing) are denoted by D.

There are two different unit normal vectors that are used frequently and that are not to be confused. One is four dimensional, time like and is normal to three dimensional space like hyper surfaces. The symbol $\bar{n}^\mu$ is used for it. The second one is a three dimensional, space like vector that is orthogonal to a boundary of a three dimensional domain. It is called n^i.

The *geometrized unit system* is used throughout this thesis. In geometric units the speed of light c and the gravitational constant G equal one.

2 A Multi-Block Infrastructure for Numerical Relativity

2.1 Introduction

A major part of the work that went into this thesis was to develop and implement high order accurate multi-block methods for solving time dependent partial differential equations and apply them to numerical relativity. This chapter gives an overview of these techniques.

The paradigm here is to stick as closely to mathematically robust methods as possible. Most of the statements about stability for the continuum and discrete equations are valid for completely general linear symmetric hyperbolic equations, even with variable coefficients. In the vacuum Einstein equations, no shocks are expected and it can be argued through a localization procedure that if a discretization is stable for the linear, variable coefficients problem, the non-linear case is stable as well. This is justified because the evolution equations can be formulated in quasilinear form

$$\partial_t u^\alpha = A^{i\alpha}{}_\beta(u)\partial_i u^\beta + \text{lower order terms.} \tag{1}$$

for a state vector u^α and the principal part $A^{i\alpha}{}_\beta$ that depends only on the field variables but not their spatial derivatives.

That the stability proofs are not rigorous manifests itself in high frequency instabilities that can show up in numerical solutions, but the pragmatic approach to suppress them using a small amount of artificial high order numerical dissipation which vanishes with increasing resolution, has been successful.

Some of the most advanced numerical relativity codes today use finite differencing or spectral methods on structured grids. While it does not seem to be necessary to switch to completely unstructured grids, for the reasons given later in this chapter and the

introduction to this thesis, the semi-structured grids that multi-block methods provide are a promising approach.

Due to the extensive experience with them, finite differencing methods are applied here, where high order accurate operators and boundary conditions that allow for proofs of numerical stability are used. A so called multi-block method that allows to cover the computational domain with an arbitrary number of coordinate patches is implemented. By doing that one gains the flexibility to better adapt coordinates to specific physical models and to set up domains with arbitrarily shaped boundaries. The numerical inter block boundary conditions are formulated in a way that global stability is guaranteed.

Chap. 2.2 gives an overview of what multi-block methods are, which kind of choices one has when implementing them and explains details about the multi-block scheme that was implemented for this thesis. How interblock numerical boundary conditions are applied in a stable way using the penalty method is described in Chap. 2.3.2. Details about the finite differencing operators and their implementation are given in Chap. 2.3.1 and 2.3.3. Chap. 2.3.4 describes two possible ways of adding artificial dissipation compatible to the finite differencing operators to the system. Issues about the time integration are described in Chap. 2.4 and finally a short overview of the actual implementation, parallelization and infrastructure is given in Chap. 2.5. A detailed description of the implementation is published in [20].

2.2 Topologies and Coordinate Systems for Multi-Block Simulations

2.2.1 How Can Numerical Relativity Profit from Multi-Block Methods?

A multi-block system is a set of touching or overlapping computational grids that, taken together, cover the whole simulation domain. Each single one of these grids can be looked at as an independent computational mesh on which numerical solutions are found using standard methods like for example finite differencing. Information can propagate through the interface between neighboring blocks, by applying suitable boundary conditions. The

main ingredients of a multi-block code as opposed to a single block one are these boundary conditions together with the definition of the topology of blocks, i. e. the information which faces of each block are connected to which faces of other blocks. In addition to that coordinates need to be defined on each block and, if possible, it can be useful to specify the geometry of the multi-block grid structure in a global coordinate system. This chapter describes several motivations for implementing such an infrastructure.

Many of the space-times of interest in numerical relativity are asymptotically flat. Ideally a domain for these has its outer boundaries at infinity. In practice often one has to place the boundaries at a finite but as large as possible distance. For initial boundary value problems to be well posed, generally smooth boundaries are required [21]. In many applications of numerical relativity a natural shape for the boundary is a sphere. Spherical boundaries have not yet been successfully implemented using Cartesian grids, but there have been attempts to approximate them, for example by the *blending method* for the outer boundary [22, 23].

A second type of boundary that is frequently needed in numerical relativity is the so called *excision boundary*. Excision is a method to avoid pathological behavior at black hole singularities by cutting regions that contain the singularities out of the computational domain. A proper chosen excision region lies within the event horizon of the black hole and has a boundary at which all characteristic modes are pointing out of the computational domain and therefore no boundary conditions have to be applied. Since the region outside of the event horizon is causally disconnected from the inside part of the space-time, excising a region that is contained by the horizon will not affect the results outside of the black hole. Still non-physical modes (gauge modes) can escape the black hole region and a badly chosen excision treatment can lead to instabilities. This technique was first applied by Thornburg [24]. On cartesian grids, a natural choice is to excise a cubical region. However there are several connected causality problems [25, 26, 27]. For Schwarzschild in Eddington-Finkelstein coordinates it was shown that the excision region has to be very

small to guarantee purely outgoing characteristics. For a Kerr space-time in Kerr-Schild coordinates for most spin parameters there is no cubical excision region that guarantees causality. Dynamical space-times make the situation even more difficult. For that reason excision boundaries are often constructed to approximate a sphere on the cartesian grid by excising all grid points that are within a certain distance from the singularity. The resulting excision region resembles a sphere built out of Lego blocks [23, 28, 29, 30]. Some numerical problems are attributed to that complicated shape [31]. It is especially not fully understood yet how to construct stable discretization schemes for a case like that.

A spherical coordinate system with the standard coordinates (r, θ, ϕ) would provide a truly spherical excision region and spherical outer boundaries. Unfortunately these coordinates are singular along the z-axis. This is a manifestation of the fact that in general it is not possible to cover a differentiable manifold with just a single regular coordinate system. On the other hand this is always possible using multiple coordinate patches.

One of the original motivations for introducing multi-block methods to numerical relativity is that they can provide smooth outer and excision boundaries while avoiding coordinate singularities. Each constituent of a multi-block grid structure has it's own local coordinate system. Therefore one can create any geometry and cover it with regular coordinate systems, including domains with spherical outer boundaries and any number of spherical excision regions.

Besides providing smooth boundaries, multi-block methods come with a number of additional advantages. These are closely related to multi-block systems adapted to some of the most common space-times and matter configurations that are studied by numerical relativity, namely compact sources for gravitational waves and the near and far wave zones. Sources can be a large variety of very different objects like black hole or neutron star binaries, collapsing stars, supernovae, accretion discs etc.. Each of these will require its own complicated numerical model as well as computational grids that adapt to its

specifics either by mesh refinement, multiple blocks or smart coordinate transformations. Once the radiation is leaving the zone close to the central source, it is not expected to develop new features especially in the directions normal to its propagation, i.e. the angular directions. In the wave zone it is therefore sufficient if the surfaces of spheres with different radii are resolved by the same number of grid points. Standard spherical coordinates are capable of doing that, but – as mentioned before – they have a coordinate singularity along the z-axis. Using multi-block this singularity can be avoided while keeping coordinates that have the desirable property of constant angular resolution. Such coordinates will be called *quasi spherical* in the following text. In standard Cartesian coordinates on the other hand, the number of grid points on constant radius spheres scales like r^2. Effectively this means that if a reasonably high resolution is chosen close to the center of the grid, the angular part of the radiation will be over-resolved at large radii and computational resources are wasted that could otherwise be used to either increase the radial resolution or to move the outer boundaries to a larger radius. While in some situations this effect can be weakened by using adaptive mesh refinement, the principal problem persists. For example, with the computational resources available today, simulations as presented in Chap. 5 could not have been done with a comparable accuracy on a cartesian grid. Multi-block and quasi spherical coordinates offer a simple, efficient and elegant solution for a numerical treatment of systems like these.

A related issue that is solved in an elegant and efficient way by quasi spherical coordinates, is related to rotating coordinate systems. Rotating coordinate systems are used in numerical relativity mainly to prevent orbiting black holes from moving on the grid. The hope is that holding the excision regions fixed will avoid numerical problems. The velocity of grid points on a rotating mesh is proportional to the distance from the rotation axis and can get large, even super luminal in some regions. While conceptually this is unproblematic, stability will require a Courant factor that decreases linearly with the coordinate speed. The Courant factor λ determines how the global time step scales with

the spatial grid spacing by the relation $\Delta t = \lambda \Delta x$. On a quasi spherical grid, the grid spacing in angular direction grows linearly with the radius and therefore with the coordinate velocity. The effect is that as λ has to be decreased, Δx increases at the same rate so that Δt stays constant. On the other hand, on a Cartesian grid where Δx is constant, the time step decreases with λ, slowing down the effective simulation speed (evolved physical time per wall clock time).

Finally it should be pointed out that with quasi spherical multi-block systems, the radial resolution can be adapted easily without distorting the coordinates. Together with the constant angular resolution this can make the use of the principally more flexible but also more complicated mesh refinement obsolete in many situations.

Considering these points it is clear that a large group of problems in numerical relativity are handled in a very efficient way by multi-block methods. One can even think of cases with non-trivial topologies that cannot be immersed in cartesian grids at all and therefore require multi-block or a similar approach. There are of course situations where other methods are preferable. For example, to track shocks in a star, adaptive mesh refinement provides more flexibility and simplicity. Hybrid methods could potentially be interesting in some cases. A Cartesian grid with mesh refinement could be used for a hydro simulation, a quasi spherical multi-block system could be connect to the outer boundary to propagate the gravitational radiation to large radii or even to null infinity.

Methods using multiple grid patches in numerical relativity were pioneered in 1987 by Thornburg [24, 32], where he also introduced excision as inner boundary conditions for black holes. Gómez et al. [33] implemented two overlapping stereographic patches to discretize the angular direction using the *eth* formalism. This was later used by Gómez et al. [34] to evolve a single, non-stationary black hole in a stable manner in three dimensions with a characteristic formulation. Thornburg [27] evolved a stationary Kerr black hole in three dimensions with the BSSN formalism using multiple grid patches. Unfortunately that code does not yet run in parallel and therefore cannot be used efficiently on parallel

machines. With a similar approach Reisswig et al applied multi-block methods to a characteristic formulation of the Einstein equations [35]. Kidder, Pfeiffer, and Scheel [36] have developed a multi-block pseudo-spectral code to evolve first-order hyperbolic systems on conforming (neighboring patches share grid points), touching, and overlapping patches. Scheel et al. [37] used this method with multiple radial grid patches to evolve a scalar field on a Kerr background. Kidder et al. [38] applied it to multiple radial grid patches for evolutions of a distorted Schwarzschild black hole and black hole binaries (Scheel et al. [39]). This code uses overlapping grids (see Chap. 2.2.2) and most of the computational time is spent for the interpolation operations necessary to apply inter-block boundary conditions. Work in axisymmetry was done by Calabrese et al who evolved a scalar field around boosted Schwarzschild and Kerr black holes [40, 25].

The code developed for the project described here distinguishes itself by being completely parallelized, efficient due to the lack of overlapping grids (interpolation is not needed) and guaranteed numerical stability for arbitrary high order schemes, whenever the evolution equations are symmetric hyperbolic. All of these points are discussed in detail in the following chapters.

2.2.2 Design Choices for Multi-Block Grid Structures

As stated in the previous chapter, the core of a multi-block method is how the different grids are connected and how information is propagated from one block to its neighbor. There are two basic methods to arrange the blocks, each one with it's own distinct advantages and disadvantages: overlapping and touching grids. At this point it should be mentioned that in the literature different names are used for these different methods. In this text the convention is adapted to use multi-block for touching and multi-patch for overlapping grids.

If the boundary region of each grid reaches into the domain covered by its neighbor grid, one talks about overlapping grids or multi-patch schemes (Fig. 1 (a)). Applying inter-patch boundary conditions is conceptually simple. Ghost zones are added to the

computational grid on each patch. Values of all the fields in the ghost zones are provided by interpolating from the interior of the adjacent patches. Obviously this boundary treatment requires the patches to overlap at least by the size of their ghost zones. Simplicity and flexibility are the advantages of overlapping grids. Since the inter-patch boundaries are simply a number of interpolation operations, ignorant of the specifics of the equations that are solved, this scheme can be used naively with any hyperbolic and even elliptic set of equations. Creating multi-patch systems, i.e. finding a topology of grids and coordinate systems is in principle simple and flexibility is high because there are almost no restrictions to the way the grids are allowed to overlap. A disadvantage of applying boundary conditions via interpolation is that even for linear equations it was not yet possible to show stability. This is especially an issue whenever the discretization method is changed. It is for example known that instabilities can show up when going to higher order finite differencing operators.

An interesting application of overlapping grids was described and tested by Calabrese and Neilsen [40, 25]. A moving spherical excision region is realized by a spherical patch that is moving together with the black hole on a Cartesian background grid. The Cartesian grid is again surrounded by a number of patches that taken together have a spherical outer boundary.

It is possible to construct schemes that provide more insight into their mathematical and numerical properties. Furthermore numerical stability can be guaranteed for arbitrary high order differencing operators. This is done by setting up touching grids and was first used for numerical relativity by Lehner, Reula and Tiglio [26]. As mentioned before this approach is called multi-block method.

One talks about touching grids, if apart from coinciding faces there are no overlaps between the domains covered by neighboring blocks. Inter-block communication could be done by adding ghost zones and interpolating from the boundary region of one block into the ghost zones of its neighbor (Fig. 1 (b)). This would be very similar to the overlapping

grids approach, with all of its advantages and disadvantages. Thornburg was able to do stable evolutions of single black holes with this method [27] using the Baumgarte-Shapiro-Shibata-Nakamura (BSSN) system, a second order in space formulation of the Einstein equations [41, 42]. Reisswig et al did evolutions with a harmonic formulation on the same grid structure [35]. To show global stability, a different approach has to be taken, by letting the boundary grid points coincide with boundary grid points from the neighbor block (Fig. 1 (c)) and computing derivatives utilizing asymmetric finite differencing stencils that do not reach across inter block boundaries. Boundary conditions are applied by communicating information from the outgoing characteristic modes on one block to the corresponding incoming modes on its neighbor. One can construct a method – the so called penalty method – to do that for which in the case of linear equations with variable coefficients stability can be shown with the energy method [43, 44, 45] (see also App. A). A requirement for stability is a symmetric hyperbolic set of evolution equations. Setting up the multi-block topology and coordinates is – compared to overlapping grids – conceptually a more involved procedure because block boundaries and grid points on them have to match up perfectly between blocks. On the other hand, with tools like GridPro [46] for constructing multi-block grid structures available, it is easy to set up any desired geometry. It should be noted that, from the computational point of view, the touching blocks approach is more efficient, since due to the lack of ghost zones and overlapping grid points, less operations are involved in evolving to the next time step. It is also more robust since stability is guaranteed for arbitrary high order finite differencing operators. For these reasons, in this thesis, the touching blocks approach is followed.

2.2.3 Examples for Multi-Block Grid Structures

A variety of multi-block systems for the most common problems in numerical relativity have been coded within this effort.

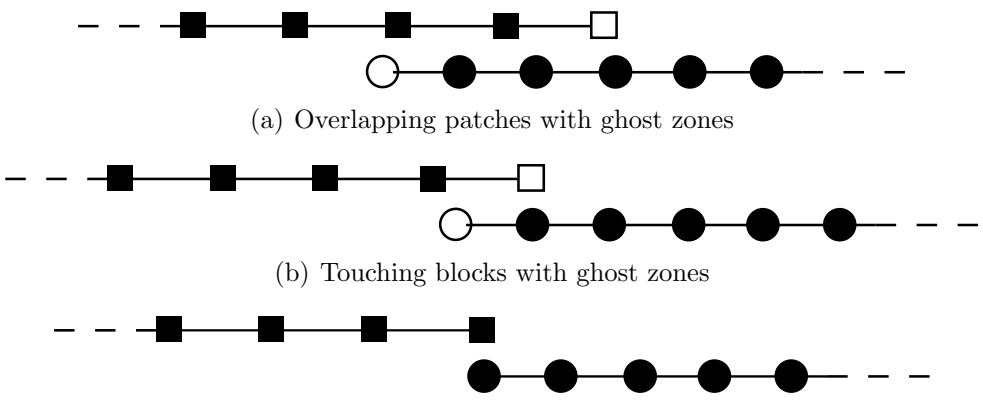

(a) Overlapping patches with ghost zones

(b) Touching blocks with ghost zones

(c) Touching blocks without ghost zones

Figure 1: The three basic configurations for multi-patch and multi-block grid structures. Panel (a) shows overlapping patches. Boundary conditions are applied through ghost zones that are updated by interpolating from the interior points of the neighbor patch. The same type of boundary condition is applied to the touching blocks that are shown in panel (b). The difference here is that the interior points of the grids do not overlap. Panel (c) shows touching blocks, for which only the boundary points coincide. These points are updated using one sided finite differencing stencils , so that no ghost zones are needed. Information is propagated through the interface between blocks via the penalty method.

The most simple multi-block systems were designed for testing and debugging of the code and consist of a single Cartesian block with periodic boundaries for some of the faces. The periodic boundaries can be applied via penalty terms.

The number of excision regions needed and the spherical shape of the outer boundary determine the design of the more complicated grid structures for actual physics simulations. For immediate and near future projects, grids with zero, one or two excision regions are in use, depending on the number of black holes that are present.

The block system of choice for single black hole evolutions consists of six blocks arranged like the faces of a cube that is then deformed to a sphere. It has one spherical excision region in the center. Since this is the multi-block system used for almost all of the work in this thesis, Chap. 2.2.4 is dedicated to it. A sketch of an equatorial cut through this system is shown in Fig. 2.

If no excision is needed, a seventh block is added to the center that covers the formerly excised region. To avoid a coordinate singularity at the origin, Cartesian coordinates are used for the central block and the coordinates of the surrounding six blocks are distorted so that they connect to the now cubical central block. Note that the outer boundary is still spherical. This system can be useful for example in simulations of massive stars without singularity or in simulations where the space-time is compactified and the outer boundary represents null infinity (which has spherical topology). It was also used extensively for evolutions of the scalar wave equation for testing of the infrastructure and the finite differencing methods in Chap. 3. Fig. 3 illustrates that system.

For binary black holes, two excision regions are needed and the grid structure becomes considerately more complicated. An example is shown in Fig. 4. The general strategy to follow is to surround each excision region by six blocks, just like in the single excision case, and then glue together the two six block systems by a number of additional coordinate blocks. The example in Fig. 4 consists of 27 different blocks and was generated using GridPro, a commercial grid generation software [46]. Tools like that become necessary for systems with a large number of blocks that make it more and more difficult to keep track by hand of how the different blocks connect to each other. Another advantage of these tools is that they automatically distribute grid points evenly throughout the domain to avoid clustering.

2.2.4 The Cubed Sphere Coordinates

This chapter gives a more detailed description of the six block system and the cubed sphere coordinates, used for evolutions describing single black holes. As in [26], a six-block setup with a global topology of $S^2 \times R^+$, referred to as *cubed sphere* coordinates is applied. This topology and the corresponding coordinates on each block are well adapted for modeling a single central object and the outgoing radiation that is generated at or close to that object. The outer and the excision boundary are both spherical.

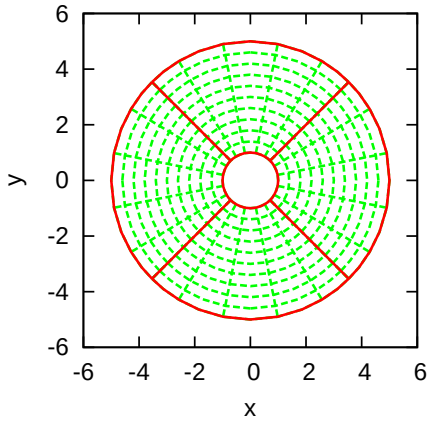

Figure 2: A cut in the equatorial plane of six blocks, in which four blocks are visible. The outer and inner domain boundaries are spheres. There is one radial coordinate spanning r = const surfaces, and two angular coordinates perpendicular to that. The radial coordinate is smooth across block boundaries.

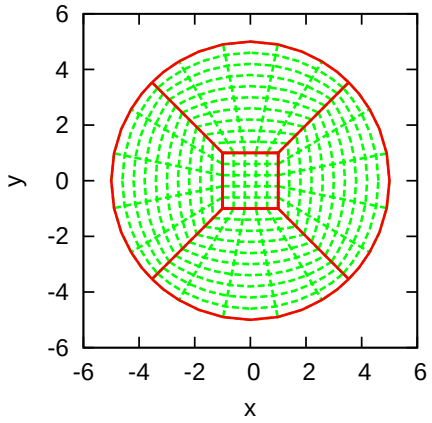

Figure 3: A cut in the equatorial plane of seven blocks, in which five blocks are visible. The outer boundary is a sphere, the inner block is a cube. There is again one radial coordinate, but it does not span r = const surfaces and it is not smooth across block boundaries except at the outer boundary. The two angular coordinates are the same as in the six-block system.

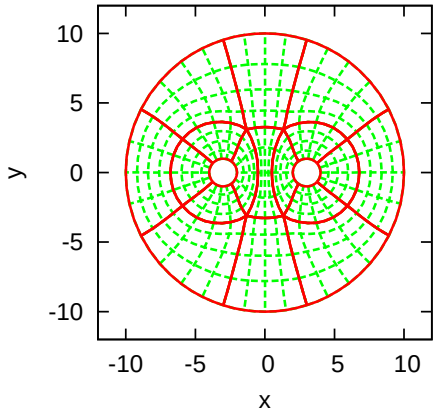

Figure 4: A cut in the equatorial plane of the imported binary black hole block system. The outer and inner boundaries are spheres. Near the boundaries, the coordinate system is similar to spherical coordinates, i.e., there is one coordinate direction perpendicular to and two direction tangential to the boundary.

Each block has local coordinates a, b and c, as opposed to the Cartesian global coordinates, here called x, y, z. The local coordinates are scaled in a way that all three of them range from -1 to +1. Coordinate c is a scaled radial coordinate $c = (-2r + r_{\rm min} + r_{\rm max})(r_{\rm min} - r_{\rm max})^{-1}$ with $r = \sqrt{x^2 + y^2 + z^2}$. $r_{\rm min}$ is the radius of the excision region, $r_{\rm max}$ the radius of the outer boundary. The blocks are denoted by numbers between 0 to 5. Block number 0 and 2 cover the neighborhood of $x = \pm 1$, block number 1 and 3 the neighborhood of $y = \pm 1$ and block number 4 and 5 the neighborhood of $z = \pm 1$. The angular coordinates are explicitly given by

$$\text{block } 0: \quad a = z/x, \quad b = y/x \tag{2}$$

$$\text{block } 1: \quad a = z/y, \quad b = -x/y \tag{3}$$

$$\text{block } 2: \quad a = -z/x, \quad b = y/x \tag{4}$$

$$\text{block } 3: \quad a = -z/y, \quad b = -x/y \tag{5}$$

$$\text{block } 4: \quad a = -x/z, \quad b = y/z \tag{6}$$

$$\text{block } 5: \quad a = -x/z, \quad b = -y/z \tag{7}$$

The inverse transformation is given by

$$\text{block } 0: \quad x = c/F, \quad y = cb/F, \quad z = ac/F \tag{8}$$

$$\text{block } 1: \quad x = -bc/F, \quad y = c/F, \quad z = ac/F \tag{9}$$

$$\text{block } 2: \quad x = -c/F, \quad y = -cb/F, \quad z = ac/F \tag{10}$$

$$\text{block } 3: \quad x = bc/F, \quad y = -c/F, \quad z = ac/F \tag{11}$$

$$\text{block } 4: \quad x = -ac/F, \quad y = cb/F, \quad z = c/F \tag{12}$$

$$\text{block } 5: \quad x = ac/F, \quad y = cb/F, \quad z = -c/F \tag{13}$$

with $F := \sqrt{1 + a^2 + b^2}$.

Fig. 5 shows the angular distribution of grid points on a constant radius sphere, an equatorial cut with data from a scalar wave evolution and the inter block boundary planes and a zoom to the excision region.

Cubed spheres are also used in climate research to model the spherical surface of the earth [47]. In that reference a related definition of the cubed sphere coordinates is given.

2.2.5 Coordinates and Tensor Bases

If the manifold that underlies the physics that is modeled has a non-trivial topology, it can be impossible to embed the computational domain in a cartesian one. In this case it is necessary to use multi-block methods. On the other hand, if this embedding is actually possible, it is convenient to define a global coordinate system that covers the whole domain. This makes it easy to set up initial data and to interpret and visualize output for coordinate dependent quantities like vectors and tensors. In addition to that, a graphical representation of the location of the grid points in a common coordinate frame is often necessary to get an intuitive picture about properties of the simulation.

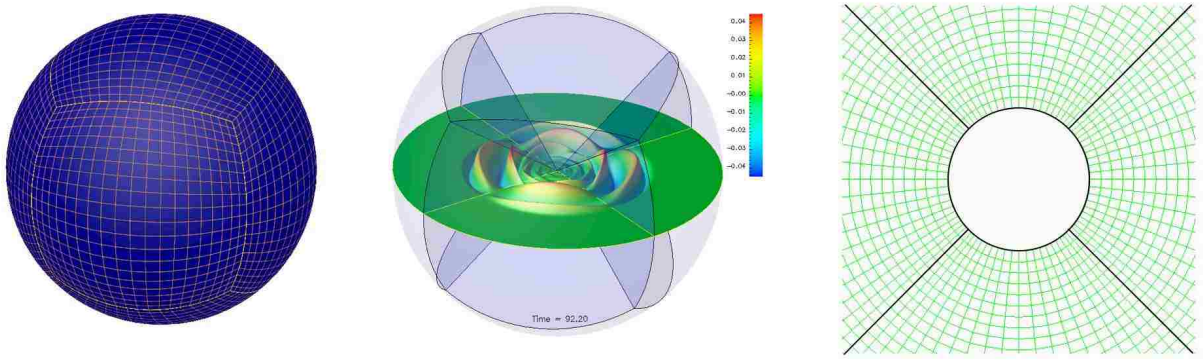

Figure 5: Illustration of the six-block grid structure and the cubed sphere coordinates that are used for the simulations in this thesis. The left panel shows the distribution of grid points on a sphere of constant radius. The central panel shows a snapshot from a scalar wave evolution on an equatorial cut. The plot refers to an $\ell = m = 2$ mode on the background of a Kerr black hole with spin $j = 0.9$ at $t = 92.2M$ (these simulations are described in detail in Chap. 4). Also shown are the locations of the inter-block boundaries. The right panel magnifies the central region of the domain in the equatorial plane, showing the grid structure around the spherical excision boundary. The four dark lines mark the interfaces between blocks.

On the other hand there always are multiple local coordinate systems, one on each block, which do not necessarily coincide among each other or with the global coordinates. They are adapted to the block geometry and the underlying physical models. That was a crucial feature of the whole multi-block construction.

The global and the patch-local coordinates are two natural choices for a coordinate basis in which vector and tensor components are expressed. Since it is known how to evolve a system on a single block, using the patch-local basis reduces the multi-block method to a fancy way of applying boundary conditions. At the inter-block boundaries coordinate transformations into a common coordinate system for both blocks are necessary. These transformations are very complicated, since formulations of Einstein's equations used in numerical relativity are in general not covariant. Therefore, by using different coordinates on each block, the characteristic variables on each side of an interblock boundary are different, even at the continuum level. The part of the code that defines the evolution

variables would not only have to provide the characteristic variables but also specify how they behave under coordinate transformations.

Using a global tensor basis makes almost all of those coordinate transformations unnecessary when applying boundary conditions. Not only is the implementation more transparent, it is also more efficient due to the reduced number of necessary operations needed for transformations between coordinate systems. Instead, only the time evolution equations have to be modified as described next.

The local coordinate indices are labeled by the letters (a, b, c) and the global coordinates by (i, j, k). When the partial derivatives are computed by finite differencing they are given in the patch-local coordinate basis, since the derivatives are naturally taken along the local coordinate lines. If one wants to express the evolution equations in a global coordinate basis, a transformation of the derivatives by inserting Jacobians in the correct places needs to be done. Since the right hand sides of the evolution equations contain only first derivatives, these are the only objects that need to be transformed in that manner. The change to the actual code is straight forward. The partial derivative operators ∂_a are redefined as

$$\partial_i = \frac{\partial x^a}{\partial x^i} \partial_a. \tag{14}$$

While the implementation of this transformation is trivial, one has to be aware of the fact that it effectively changes the system of evolution equations. It was found that when evolving in the global basis this can manifest itself in high frequency instabilities, which can be suppressed by small amounts of high order numerical dissipation (see Chap. 2.3.4).

In Chap. 3 and 4 for solving the scalar wave equation a patch-local basis was used. Chap. 3.5 shows a comparison between both coordinate choices. For the non-linear Einstein equations described in Chap. 5 a switch to a global coordinate frame was done to simplify the code and minimize debugging during the development phase.

2.3 Stable Discretization of Hyperbolic Partial Differential Equations

2.3.1 The Summation by Parts Condition

A scalar product of two discrete functions u_i and v_i (the index is labelling grid points) can be defined by a matrix σ as

$$\langle u, v \rangle = h \sum_{i,j=1}^{n} u_i v_i \sigma_{ij} \tag{15}$$

The scalar product or norm is called *diagonal* if

$$\sigma_{ij} = \sigma_{ij} \delta_{ij} \tag{16}$$

and it is said to be *restricted full* if for points at the boundary, here denoted by i_b it satisfies

$$\sigma_{i_b j} = \sigma_{i_b i_b} \delta_{i_b j}, \tag{17}$$

that is σ_{ij} is diagonal on the boundary but does not need to be diagonal in the interior.

A finite differencing operator D is said to satisfy summation by parts (SBP) with respect to a positive definite scalar product σ if, on a computational domain $[a, b]$, it satisfies the condition

$$\langle u, Dv \rangle + \langle v, Du \rangle = (uv) \,|_a^b \tag{18}$$

for all grid functions u and v. Summation by part can be seen as the discrete version of integration by parts that is obtained by exchanging integrals by finite sums and partial derivatives by finite differencing operators.

The motivation for using summation by parts finite differencing operators comes from the way stability is shown for a set of symmetric hyperbolic equations using the energy method (see for example [48] and App. A). The central ingredient for computing the growth of the energy over time for the continuum equations is to use integration by parts

to interchange derivatives with integrals. If the differencing operators in the semi discrete equations – i.e. discretized in space but not in time – satisfy summation by parts, energy estimates that are valid in the continuum case carry over directly.

Restricting the scalar product norm σ_{ij} to some subclass (for example to a diagonal norm), instead of keeping it completely general, influences the properties of the corresponding finite differencing operator, including the convergence order at the boundary, the stencil width or the spectral radius.

The straightforward choice of a diagonal norm and one dimensional differencing operators already provides a lot of advantages that makes this construction very attractive and therefore widely used. The summation by parts property is guaranteed to hold in several space dimensions by simply applying the 1D operator along each direction [49, 50, 51]. In addition to the SBP property, to compute the energy estimate for showing numerical stability one needs to be able to bound the norm of the commutator between the difference operator and the principal part of the equations for all resolutions. This is always possible in the diagonal case [52]. On the other hand if the accuracy of the diagonal norm operators is of order $2p$ in the interior it is only of order p near the boundary, i.e. only half of the interior [53, 54, 55]. This will considerably lower the global and local convergence order, as errors originating from the boundaries propagate into the interior of the computational domain. For example in numerical experiments using the D_{8-4} operator a global convergence order of about 5 was found, which is actually the expected value [56, 57].

The problem of lower convergence order near the boundaries can be partly overcome by giving up on using a diagonal norm. Summation by parts operators that are only one order less accurate at the boundary than they are in the interior were implemented. The corresponding norm is called restricted full and is defined by Eq. (17). Unfortunately for this norm, the advantages that were described for the diagonal norm operators disappear. It is no longer guaranteed that summation by parts holds in several dimensions if 1D SBP

operators are simply applied along all directions [49, 50, 51]. In systems with variable coefficients, the commutator between the principle part of the equations and the derivative operator is not necessarily bounded for all resolutions [52]. The consequence is that stability can no longer be guaranteed in three dimensional or even one dimensional systems with variable coefficients. Improving the convergence order near the boundary therefore makes it necessary to stabilize the scheme by means of numerical high order artificial dissipation. A detailed description of the dissipation operators used in the work presented here can be found in Chap. 2.3.4.

Using a diagonal norm, differencing operators of order two, four, six, eight and ten in the interior and, as mentioned above of half order at the boundaries were implemented. They are denoted by $D_{2-1}, D_{4-2}, D_{6-3}, D_{8-4}$ and D_{10-5} respectively. Using a non-diagonal restricted full norm, the operators D_{4-3}, D_{6-5} and D_{8-7} of order four, six and eight respectively in the interior and one order less at the boundaries were implemented. In general the construction of these operators is not unique. Only in the second order in the interior case there is a unique operator satisfying SBP, and its norm is diagonal. With respect to higher order operators, the following holds for the diagonal norm based ones: D_{4-2} is unique, while D_{6-3}, D_{8-4} and D_{10-5} comprise a one-, three-, and ten-parameter family, respectively. In the restricted full case, D_{4-3}, D_{6-5} and D_{8-7} have three, four and five free parameters, respectively. Chap. 2.3.3 describes how this ambiguity can be used to improve certain properties of the operators.

The operator used most widely throughout this thesis is D_{8-4} because of its relatively good accuracy (see Chap. 3) and robustness. At least for linear equations, stability is guaranteed and the problem of choosing good dissipation operators and parameters can safely be ignored. D_{6-5} is used some places. Numerical experiments show that, as predicted by Gustafsson [56, 57], global sixth order convergence can be achieved with it and its accuracy is often superior to D_{8-4} in the cases that were used for comparison.

Results are shown in Chap. 3. A comparison of convergence and accuracy of different SBP operators in 1D can be found in [58].

2.3.2 Penalty Boundary Conditions

As mentioned above the core of a multi-block method is how to transfer information from one block to it's neighbor, or in other words, how to apply interblock boundary conditions. Global numerical stability can be shown for semi discrete – i.e. discretized in space but not in time – linear symmetric hyperbolic equations, given finite differencing operators that satisfy summation by parts (see 2.3.1) and penalty interblock boundary conditions. Given a stable semi-discrete scheme, stability for the completely discretized system follows, if a time integrator which is what is called locally stable is used [59]. Examples for locally stable time integrators are third and fourth order accurate Runge-Kutta methods (RK3 and RK4). An introduction about analyzing stability using the energy method is given in Chap. A.

It is known for single block systems how to construct outer boundary conditions that are well posed in the continuum. A simple, but still widely used boundary type is the maximally dissipative boundary condition. The evolved fields are decomposed into their characteristic modes and at the outer boundaries the incoming modes are chosen to inject less energy to the system than the outgoing modes dissipate from it. This could be imposed numerically by just overwriting the incoming modes. This scheme is unstable though. To remedy that problem, the penalty method was first introduced.

At the interface between two blocks, one might naively follow a similar strategy. The fields, this time on both blocks, would be decomposed into their characteristic fields and the outgoing fields of one block would be copied into the ingoing fields of it's neighbor and vice versa. It turns out though that – analogous to the outer boundary case – with this algorithm the energy estimate is violated and instabilities show up in actual simulations.

The idea behind the penalty method is to allow for a mismatch between characteristic modes on the face of one block and it's neighbor block. Terms that *penalize* this mismatch

are added to the discretized right hand sides of the equations and they are chosen in a way that the mismatch is converging towards zero over time and further, so that an energy estimate, and therefore numerical stability, is guaranteed, for an arbitrary high order of accuracy [43, 44, 45].

This paragraph illustrates with a simple example how the penalty method works and how the energy estimate showing stability follows by constructing a numerical scheme to solve the one dimensional advection equation for a state vector $u(t, x)$

$$\partial_t u = \Lambda \partial_x u. \tag{19}$$

The spatial domain is $(-\infty, +\infty)$ with appropriate fall off conditions. That domain is covered with two blocks, block one for the range $(-\infty, 0]$ and block two for $[0, +\infty)$. The discretized grid function u_i at each point is labeled u_i^l for points on block one and u_i^r for points on block two, where the index i labels the grid points (on each grid $i = 0$ is the point on the interface). The two blocks are discretized by regular grids with grid spacing h^l and h^r which do not have to be equal and derivatives are approximated by finite differencing operators D^l and D^r that satisfy summation by parts (see Chap. 2.3).

The scalar products on the two blocks are written as

$$\left\langle u^l, v^l \right\rangle = h^l \sum_{i,j=-\infty}^{0} \sigma_{ij}^l u_i^l v_j^l, \tag{20}$$

$$\left\langle u^r, v^r \right\rangle = h^r \sum_{i,j=0}^{+\infty} \sigma_{ij}^r u_i^r v_j^r. \tag{21}$$

If the norm is diagonal, the semi-discrete evolution equations including penalty terms at the boundary are

$$\partial_t u_i^l = \Lambda D^l u_i^l + \frac{\delta_{i0} S^l}{h^l \sigma_{00}^l} \left(u_0^r - u_0^l \right), \tag{22}$$

$$\partial_t u_i^r \;=\; \Lambda D^r u_i^r + \frac{\delta_{i0} S^r}{h^r \sigma_{00}^r} \left(u_0^r - u_0^r\right). \tag{23}$$

The non-diagonal case is more complicated and for simplicity is left out of the discussion at this point. S^l and S^r are parameters that for a certain energy estimate need to be restricted by two conditions to guarantee stability. These conditions are now derived.

For this simple example, a natural way to define an energy is

$$E \equiv \left\langle u^l, u^l \right\rangle + \left\langle u^r, u^r \right\rangle. \tag{24}$$

The time derivative of E is taken and with Eq. (22), (23) and the summation by parts property one gets

$$\dot{E} = (\Lambda - 2S^l)(u_0^l)^2 + (-\Lambda - 2S^r)(u_0^r)^2 + 2(S^l + S^r) u_0^l u_0^r. \tag{25}$$

To get an energy estimate, the right hand side of that expression must be non-positive for all u_0^l and u_0^r, which results in the following three conditions:

$$\Lambda - 2S^l \;\leq\; 0 \tag{26}$$

$$-\Lambda - 2S^r \;\leq\; 0 \tag{27}$$

$$(\Lambda + S^r - S^l)^2 \;\leq\; 0. \tag{28}$$

It follows directly that $\Lambda + S^r - S^l = 0$ and a second constraint to the choice of S^l and S^r that depends on the signature of Λ. For positive Λ one gets

$$S^l = \Lambda + \delta, \quad S^r = \delta, \quad \text{for any } \delta \geq -\frac{\Lambda}{2}. \tag{29}$$

Negative Λ results in the condition

$$S^r = -\Lambda + \delta, \quad S^l = \delta, \quad \text{for any } \delta \geq \frac{\Lambda}{2}, \tag{30}$$

while a vanishing Λ results in a degeneration of these conditions and can be seen as the limiting case. For the minimum value of δ allowed by the above constraints, the global energy estimate is the same as for a single grid without an interface. In particular for that value of δ the scheme is conservative (the energy is preserved). For larger values of δ there is damping in the energy, proportional to the mismatch at the interface.

The more general case of systems of equations in higher dimensions follows the same principle, applying the 1D treatment to each characteristic field.

2.3.3 Construction of Summation-by-Parts Finite-Differencing Operators

Stability is not the only concern when developing a numerical scheme. Others are for example computational efficiency and accuracy. In the construction of SBP finite differencing operators there are free parameters that can be used to enhance efficiency and accuracy. Optimization criteria that were used for that are discussed here. More details are given in [60].

First some notation has to be fixed. If the accuracy of the difference operator D in the interior is $2p$, then there are b points at and near the boundaries where the order of D is only q. In the diagonal case one has $q = p$, and in the restricted full case it is $q = 2p - 1$. b is called the boundary width. The difference operator at these b points uses (up to) s points to compute the derivative. s is called the boundary stencil size.

When expanding D in a Taylor series one has

$$Du|_{x_i} = \left.\frac{du}{dx}\right|_{x_i} + c_i h^q \left.\frac{d^{q+1}u}{dx^{q+1}}\right|_{x_i} \quad \text{for } i = 1 \ldots b \tag{31}$$

where h is the grid spacing and $x_i = ih$. One calls c_i the *error coefficients*.

In what follows, three cases for each family of operators of a given order are considered, denoted by:

- Minimum bandwidth: If there are n free parameters, it is always possible to set n of the derivative coefficients to zero, thereby minimizing the computational cost of evaluating the derivatives in the boundary region.

- Minimum spectral radius: In this case, the eigenvalues of the amplification matrix are calculated numerically for a test problem, and the parameters chosen to minimize the largest eigenvalue. That largest eigenvalue essentially determines the CFL limit. By minimizing the former, the latter is maximized, resulting in a increased allowed time step and an effective performance improvement.

- Minimum ABTE: The average boundary truncation error (ABTE) is minimized, which is defined as

$$\text{ABTE} := \left(\frac{1}{b} \sum_{i=1}^{b} c_i^2 \right)^{1/2} . \tag{32}$$

The test problem that is used to compute the spectral radius of the amplification matrix is the same one that was used in [26]: an advection equation propagating in a periodic domain. Periodicity is enforced through an artificial interface boundary via penalties.[1] The penalty parameter is chosen to be $\delta = -1/2$ (see Chap. 2.3.2), which means that the semi-discrete energy is strictly preserved, and that the amplification matrix is anti-Hermitian, and therefore the real part of all eigenvalues is zero.

Another option would be to compute the spectral radius of the discrete difference operator itself [61]. In this case, the spectrum is in general not purely imaginary, since the boundary conditions have not been imposed yet. In practice it was found, though, that both approaches lead to similar operators, in the sense that a derivative operator

[1] Truly periodic domains (that is, without an interface) do not require boundary derivative operators, and therefore do not constitute a useful test here.

with small spectral radius usually also leads to amplification matrices for the above test problem with small spectral radii as well.

It is worth pointing out that for the diagonal operator case the bandwidth and the ABTE can be globally minimized by analytically choosing the parameters, since the ABTE is a quadratic function of the parameters and therefore has a global minimum. This is not the case for the spectral radius. Therefore, when it is referred to minimizing the spectral radius, a numerical minimization is performed and it cannot be claimed that a global minimum is actually found.

It is now illustrated how these optimization criteria work in practice on the two most accurate operators that were made available for actual simulations: D_{8-4} , which is constructed from a diagonal norm and D_{6-5} which is based on a restricted full norm. The family of D_{8-4} operators has three free parameters. There are no restrictions how to choose those, since the norm of D_{8-4} is independent of them and always positive definite. The three dimensional parameter space was searched for minima in the bandwidth, spectral radius and ABTE. For the latter, instead of a unique minimum one finds a one parameter family of operators that minimize the ABTE. This is fortunate because it allows to use the free parameter to decrease the spectral radius as far as possible. Tab. 1 shows the spectral radius, ABTE and the error coefficients for the operators constructed using different optimization criteria. The minimum ABTE and minimum spectral radius operators have similar properties in these quantities and one can expect comparable behavior in their numerics. A numerical comparison of these operators is shown in Fig. 9. It shows – at least for the test that is specified in Chap. 3 that even though the error coefficients are quite close, the errors with the minimum ABTE operator are roughly a factor of two below the errors when minimizing spectral radius. The features of the minimum bandwidth are a very large spectral radius (which translates into a small time step for stable evolutions) and some error coefficients that are very large compared to

Table 1: Properties of the diagonal norm D_{8-4} operators.

Operator	Minimum bandwidth	Minimum spectral radius	Minimum ABTE
Spectral radius	16.0376	2.229	2.231
ABTE	1.2241	0.3993	0.3474
c_1	-0.5878	-0.8277	-0.8086
c_2	0.1068	0.3682	0.3439
c_3	3.1427	-0.3819	0.0228
c_4	-0.7918	-0.2186	-0.3086
c_5	0.9886	-0.3412	0.0225
c_6	0.3304	0.3619	0.2970
c_7	-0.1995	-0.1097	-0.0823
c_8	-0.0211	-0.0465	-0.0497

the other two operators. Due to these undesirable properties an implementation was not considered.

Contrary to the diagonal norm operators, the restricted full norm is not necessarily positive definite. Therefore fixing the free parameters in the construction of the differencing operators is subject to the constraint that they define a positive definite norm. There are four independent parameters in the construction of the D_{6-5} operator. As for the D_{8-4} one finds parameter values that minimize the bandwidth, spectral radius or the ABTE. In addition one needs to check if these minima result in a positive definite norm. A comparison of the resulting operators is shown in Tab. 2. In spite of its comparably small spectral radius, the error coefficients of the minimum spectral radius operator are large enough that it was not possible to stabilize it, even when adding considerable amount of dissipation to it. The minimum bandwidth and minimum ABTE operators can be stabilized, where for the latter, a significantly smaller amount of dissipation is needed. In addition to that, the errors of the ABTE operator are less. This is reflected in the smaller error coefficients, compared to the minimum bandwidth operator.

Table 2: Properties of the restricted full norm D_{6-5} operators.

Operator	Minimum bandwidth	Minimum spectral radius	Minimum ABTE
Spectral radius	2.940	1.458	3.194
ABTE	0.0986	0.5380	0.0648
c_1	0.1667	1.3692	-0.0154
c_2	-0.1558	-0.2682	-0.0507
c_3	0.0672	-0.2118	0.1336
c_4	0.0953	0.0097	0.0532
c_5	-0.0433	0.0702	-0.0733
c_6	0.0141	0.1434	0.0187
c_7	-0.0163	-0.0972	-0.0123

2.3.4 Artificial Dissipation

Two types of dissipation operators are used, both compatible with the described finite differencing operators.

One type was introduced by Mattson, Svärd and Nordström in [62] and it is referred to as *MSN operator*. The key property of these operators is that they are semi-negative definite with respect to the corresponding SBP scalar product, and that this holds for any SBP operator of arbitrary high order. Semi-negative definite dissipation operators do not spoil energy estimates. Naive prescriptions such as Kreiss-Oliger dissipation in the interior and zero at and close to boundaries do spoil energy estimates and one can show that they cause numerical instabilities in concrete examples. The MSN dissipation operators are

$$A_{2p}^{MSN} = -\frac{\epsilon}{2^{2p}} h^{2p} \Sigma^{-1} D_p^T B_p D_p \tag{33}$$

where Σ is the scalar product of the $2p$th-order accurate summation by parts operator. Here h is the grid spacing and ϵ a free parameter. D_p is a consistent approximation to the pth derivative with minimal width – minimal width means that the stencil must contain as few points as possible – and B_p is a diagonal matrix, the so called boundary operator.

The boundary operator is positive semi-definite and allows boundary points to be treated differently from interior points. It cannot be chosen freely but rather is subject to certain restrictions.

For the diagonal norm, B_p can simply be chosen to be a unit matrix. This choice guarantees that pth order accuracy is reached at and close to the boundary. The accuracy of the dissipation operator is the same as for the summation by parts operators, thus the dissipation is consistent with the discretization method.

In the case of restricted full norm operators, the accuracy requirement near the boundary is more strict. The dissipation operator should have order $2p-1$ at the boundary and order $2p$ in the interior, which requires a different choice of B_p. Again following [62] B_p is chosen to be a diagonal matrix, where the diagonal is the restriction onto the grid of a piecewise smooth function. The numerical domain is divided into three regions in each dimension: an interior part and on either side two transition regions containing the boundaries. The transition region has a fixed size that is independent of the resolution. Within the transition region the function, B_p, increases from $O(h^{p-1})$ at the outer boundary to a constant value 1 at the boundary with the interior region in such a way that the derivatives of B_p up to order $p-2$ vanish at either ends. In the interior region the function has the constant value 1.

For the D_{4-3} operator, B_p has the value h at the boundary and increases linearly to 1 in the transition region. For the D_{6-5} operator, a cubic polynomial with vanishing derivatives is used at either end of the transition region to increase the value of B_p from h^2 at the boundary to 1 in the interior. For the D_{8-7} operator, the boundary values for the transition region are h^3 and 1, and a fifth order polynomial is used to make the first and second derivatives vanish at either end of the transition region.

For the parameter ϵ one makes the choice $\epsilon = 2^{-2p}$, since then the parameter used to specify the strength of the dissipation has approximately the same allowed numerical range, independently of the order of the operator.

Note that for the diagonal case up to order eight in the interior, the scalar product Σ is independent of the free parameters in the construction of the finite differencing operators, while for the higher order diagonal operators and the restricted full norm operators a unique dissipation operator has to be constructed for each parameter choice.

A disadvantage of the MSN dissipation operators is that their dissipation parameter in some cases has to be scaled with changing numerical resolution to maintain stability. In the interior the MSN operators do not reduce to Kreiss-Oliger ones, for which the amplification factor is constant for a fixed dissipation parameter. While this is not a problem of principle, it can turn out to be unpractical since fine tuning of the parameter might be necessary for production runs. For this reason Kreiss-Oliger (KO) dissipation operators [63] that do not need adjustments at different resolutions were implemented. They are constructed according to

$$A_{2p}^{KO} = -\frac{\epsilon}{2^{2p+2}} h^{2p+1} \Sigma^{-1} D_{p+1}^T B_p D_{p+1}. \tag{34}$$

Again Σ is the norm of the $2p$th accurate summation by parts derivative operator. In this form, the KO operator is compatible with the finite differencing operators. The accuracy is the same as the one of the SBP operator near the boundary and one order higher in the interior and they are semi-definite with respect to the SBP scalar product. A disadvantage of KO type dissipation compared to the MSN one is a slightly larger stencil size.

2.4 Time Integrator

Unless noted otherwise a fourth order accurate Runge-Kutta time integrator (RK4) is used. The choice of time step is crucial to the stability of the numerical solution. The CFL condition for a uniform grid is

$$\Delta t = \lambda \Delta x \tag{35}$$

where the constant λ is the so called Courant factor. In the framework of multiple blocks one has to note that the time step should not be determined by the local spatial grid spacing but rather by the proper distance between the grid points. This proper distance can vary significantly over the computational domain and in the case of dynamical gauge functions also in time. This makes finding the correct time step not impossible but cumbersome and time consuming.

To avoid this problem for some simulations an adaptive RK4 time stepping algorithm is applied that picks the step size automatically for a given error tolerance [64]. The idea behind this method is to evolve from $t = t^n$ to $t = t^{n+1} = t^n + \Delta t$, with the time step size Δt and again with half the time step size $\Delta t/2$. The difference between both results is a measure for the truncation error. If the truncation error is above the specified tolerance, the time step size is decreased, if it is below, the time step is increased. That helps to avoid unnecessary small time steps and can give considerable performance improvements. In [64] it is claimed that performance often can improve by two orders of magnitude or more. In the same reference it is also shown that the computational overhead due to extra evolution steps necessary for estimating the truncation error, is only a factor of 1.375 compared to a fixed time step RK4 integrator. The adaptive time step also allows to control how much of the total error is due to time integration. For example, for the sake of testing convergence one can choose a very small error tolerance in the time integration to make sure that the total error and thus the convergence factor is dominated by the spatial differencing.

2.5 Computational Infrastructure and Parallelization

The choice was made to base the implementation on the Cactus infrastructure [18]. Cactus is a framework for doing scientific computation and especially for solving partial differential equations numerically. The core of Cactus is the so called *flesh*, a system of scripts that manages modules, so called *thorns* and lets them interact and work together. Any functionality needed to solve a specific scientific problem is provided by thorns, from

low level computational functions, like providing memory for meshes or distributing data among compute nodes on parallel machines, to the actual *physics thorns* that contain solvers for specific equations and analysis tools.

Cactus comes together with a set of thorns that provide basic functionality, like I/O routines, time integrators, a parallel driver for uniform grids and an interface for applying boundary conditions.

The main motivation to use an infrastructure like this is that it allows to write code in a modular way. It makes it comparably easy to for example use the infrastructure part of a multi-block code together with any evolution code, that was designed without multi-block in mind, given that it was written with a certain degree of generality. Another selling point for Cactus is the large amount of available modules that were written and well tested in the past, like I/O routines or analysis tools, which typically can be used out of the box with almost no modifications necessary.

As a driver, i.e. the module that is responsible for memory allocation and load distribution, Erik Schnetters *Carpet* [65] was chosen. Carpet is designed to implement fixed and adaptive mesh refinement in Cactus and was, as part of the effort described here, extended to assign storage, handle inter processor communication and provide I/O functionality for multi-block simulations. A benefit of using Carpet is that combining multi-block with mesh refinement is in principle possible using already existing infrastructure code. This has not been tested yet.

It should be stressed that all of the major modules necessary for doing multi-block simulations had to be newly written or at least extended significantly for the effort described in this thesis. This includes extensions to Carpet, parallelization, data output and newly developed boundary conditions, an interface to derivative operators, high order SBP finite differencing operators and two evolution codes, one for the scalar wave equation and one for a generalized harmonic formulation of the Einstein equations.

Following is a description of the main modules that were developed in the described effort to make Cactus and Carpet multi-block enabled. To be as modular as possible, the infrastructure part has been split up between several thorns:

The thorn *MultiPatch* defines the topology of the multi-block system. It specifies the number of blocks and how they connect to each other, i.e. which face of one block is adjacent to which face of which other block, how the faces are rotated with respect to each other and which faces coincide with the outer boundary. Apart from the topology, *MultiPatch* also knows the location of the blocks in the global coordinate space and can do mappings from global to local block coordinates.

The thorn *PenaltyPatchBoundary* applies boundary conditions by adding penalty terms to the right hand sides of the of the equations. It requires the characteristic fields as input and is therefore independent of the particular evolution system. It can be used for inter block boundaries as well as for outer boundaries. A more detailed description of the penalty method is given in Chap. 2.3.2.

The thorn *SummationByParts* computes high order finite differences using operators that satisfy summation by parts. This thorn was developed as part of the multi-block effort but actually provides a generic interface for computing numerical derivatives. Operators up to order ten have been coded. Close to the boundaries one sided stencils can be used.

The current implementation parallelizes a domain by splitting and distributing each block separately onto all available processors. This is not optimal, and it would be more efficient to split blocks only if there are more processors than blocks, or if the blocks have very different sizes. This optimization was not implemented at the time most simulations for the thesis were done, but is available now.

A scaling test on multiple processors has been performed by solving a simple test problem on a multi-block grid structure and measure the time it takes to evolve 100 time

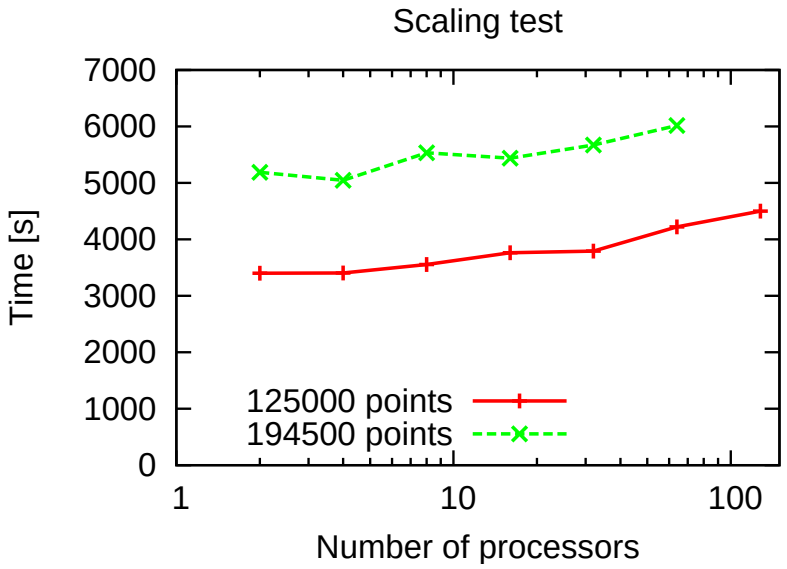

Figure 6: Wall clock time vs. numbers of processors for 100 time steps of a test problem. The load of each processor is kept approximately constant at 125000 and 194500 grid points, respectively. The implementation scales up to at least 128 processors.

steps.[2] With increasing number of processors, the number of grid points is increased as well, so that the load per processors remains approximately constant. This is realistic, because one chooses the number of processors that one uses for a job typically depending on the problem size. Fig. 6 shows the results of the scaling tests for two such problem sizes. It was found that the implementation scales well up to at least 128 processors, and would probably continue to scale to larger numbers. See [66] for a comparison of other benchmarks using Cactus and Carpet.

It would also be possible to distribute the domain onto the available processors by giving (at least) one domain to each processor. This would mean that one splits domains when one adds more processors, introducing additional inter-block boundary conditions. Penalty inter-block boundary conditions are potentially more efficient than using ghost

[2]This test was performed with a 4th order Runge–Kutta integrator, the scalar wave equation formulated in a patch-local tensor basis, a seven-block system, the D_{6-5} differencing operators, and a Mattsson–Svärd–Nordström dissipation operator. The number of grid points per block was varied from 65^3 to 253^3 to keep the load per processor approximately constant.

zones, since they require an overlap of only one single grid point. An nth order accurate finite differencing scheme, on the other hand, requires in general an overlap of $2n$ grid points. Penalty boundary conditions thus require less communication between the blocks. A disadvantage of this scheme is that the exact result of a calculation then depends on the number of processors. Of course, these differences are only of the order of the discretization error.

Such differences are commonly accepted when e.g. elliptic equations are solved. Many efficient algorithms for solving elliptic equations apply a domain decomposition, assigning one domain to each processor, and using different methods for solving within a domain and for coupling the individual domains. The discretization error in the solution depends on the number of domains. For hyperbolic equations that are solved with explicit time integrators, it is often customary to not have such differences. On one hand, this may not be necessary to achieve an efficient implementation, and on the other hand, it simplifies verifying the correctness of a parallel implementation if the result is independent of the number of processors. However, there are no fundamental problems in allowing different discretization errors when solved on different numbers of processors, especially if this may lead to a more efficient implementation. This parallelization method has partly been implemented and preliminary numerical tests with the code described in Chap. 5 indicate that a factor or roughly two in speed can be gained from it.

3 Numerical Accuracy and Convergence

3.1 Linear Scalar Wave Equation on a Minkowski Background

In Chap. 2 an overview of the numerical techniques that were implemented was given. As a proof of concept and to check the correctness of the fairly complex code, a thorough numerical study of convergence and accuracy is presented in this chapter. There are a number of requirements on such tests to make them general enough to incorporate all the key parts of the new infrastructure. Inter-block boundaries must be present so that the according boundary conditions are applied. Furthermore the block coordinate systems should be non-trivial, so that the boundary conditions are tested in fairly general situations. Finally to make error estimates easier, one wants a physical system for which the analytic solution is known at all times.

In this chapter such a test is specified and realized with a variety of different order accurate summation by parts finite differencing operators.

Also shown is a numerical comparison of simulations using a patch-local and a global tensor basis as described in Chap. 2.2.5 , investigating which tensor base is preferable.

The results presented in this chapter are described in more detail in [60].

Numerical evolutions of the scalar wave equation on a Minkowski background serve as an ideal test case. The form of the equations is given in Chap. 3.2. These simulations are suitable for testing and verifying the robustness of the multi-block implementation, penalty boundary conditions and summation by parts operators. In addition to that analytic solutions are known. The evolution is done on a multi-block grid structure that consists of seven components (see Chap. 2.2.3). Because of the non-cartesian local coordinate systems, even in the case of a Minkowski background, the components of the metric are non-trivial and their spatial derivatives do not equal zero. Conceptually this is as challenging to the code as choosing a curved background metric, since the components of the Minkowski metric in arbitrary coordinates are non-trivial and due to different local

coordinate systems on the different blocks all the coordinate transformations that one needs in the most general case need to be done when applying boundary conditions. For that reason one can test the functionality of all the key elements of the multi-block code using a setup like that.

3.2 Formulation of the Evolution Equations, Initial Data and Boundary Conditions

The wave equation for a massless scalar field Φ is written as

$$\nabla^{\mu}\nabla_{\mu}\Phi = 0 \tag{36}$$

where ∇_{μ} is the covariant derivative compatible to the four metric. The metric can generally be written as (see App. C)

$$g^{\mu\nu} = \alpha^{-2} \begin{pmatrix} -1 & \beta^i \\ \beta^i & \alpha^2 H^{ij} \end{pmatrix} \tag{37}$$

where, given the inverse three metric γ^{ij}, the definition $H^{ij} = \gamma^{ij} - \beta^i\beta^j/\alpha^2$ is used. Here γ is the determinant of the three metric. α and β^i are the lapse and the shift, respectively, and they are defined in App. C. For simplicity, and since only linear effects are of interest here, the metric is assumed to be time independent, and the evolution equations in first order symmetric hyperbolic form become

$$\dot{\Phi} = \Pi \tag{38}$$

$$\dot{\Pi} = \beta^i\partial_i\Pi + \frac{\alpha}{\sqrt{\gamma}}\partial_i\left(\frac{\sqrt{\gamma}}{\alpha}\beta^i\Pi + \alpha\sqrt{\gamma}H^{ij}d_j\right) \tag{39}$$

$$\dot{d}_i = \partial_i\Pi. \tag{40}$$

This formulation is described in more detail in [67] and [26].

The non-zero characteristic speeds $\lambda_\pm$ and eigenmodes $w_\pm$ with respect to a vector n_i are

$$\lambda_\pm = \beta^i n_i \pm \alpha\sqrt{\gamma^{ij} n_i n_j} \tag{41}$$

$$w_\pm = [\beta^i n_i \pm \alpha\sqrt{\gamma^{ij} n_i n_j},\ H^{ij} n_j]^T. \tag{42}$$

The zero speed eigenmodes are

$$w_0 = d_i - n_i d_j n^j. \tag{43}$$

Reference [67] describes a number of useful features of this formulation. Equations (38)-(40) are symmetric with respect to the physical energy. Whenever maximally dissipative boundary conditions are applied, this energy does not grow. Maximally dissipative boundary conditions are automatically constraint preserving. The Leibniz rule is not needed to show that the energy does not grow, thus the discretization is strictly stable. The physical energy however is not positive definite in the interior of a black hole, where the Killing vector becomes space-like. Only for a computational domain that does not include the black hole, long term stability is guaranteed. Formulations that are globally symmetric hyperbolic and that conserve the physical energy outside of a black hole can be constructed [68].

Solutions to the wave equation on a flat background space-time are analytically known for all times. The difference between these solutions and the numerical data from simulations with according initial data are computed and it is checked that these differences converge towards zero with the correct rate when increasing the resolution. The solution represents plane waves traveling along an arbitrary direction. Corresponding initial data are

$$\Phi(t=0) = A\cos(2\pi \mathbf{k}\cdot\mathbf{x}) \tag{44}$$

$$\Pi(t=0) = -2\pi A|\mathbf{k}|\sin(2\pi \mathbf{k}\cdot\mathbf{x}) \tag{45}$$

$$d_i(t=0) \quad = \quad -2\pi A k_i \sin(2\pi \mathbf{k}\cdot\mathbf{x}). \tag{46}$$

$\mathbf{k}$ is the wave vector pointing in the propagation direction and the wave length is $\lambda = 2\pi/|\mathbf{k}|$. $\mathbf{x}$ is the coordinate vector. The units are chosen so that the wave propagates with a global coordinate speed of one. In all of the simulations presented here, the wave amplitude is $A = 1.0$ and the wave vector $\mathbf{k} = (0.2, 0.2, 0.2)^T$ so the wave is propagating along the main diagonal.

At the outer boundaries the analytically known solution is injected via penalty terms. For that one needs to compute the ingoing characteristic modes from the analytic solution and penalize the incoming numerical characteristic modes against them.

With these boundary conditions the numerical results should converge towards the analytic solution.

3.3 Grid Structure

To avoid dealing with holes in the domain but keeping a smooth outer boundary the simulations are done on a spherical domain using the seven block geometry described in Chap. 2.2.3. Fig. 7 shows schematically the geometry of that setup and how it relates to the parameters r_0 and r_1 that determine the domain size. The seven block system is derived from the six blocks cubed sphere system and is used when no excision region is required. The hole in the center of the six block system is filled up with a seventh block. To avoid coordinate singularities, this block is chosen to be cubical with standard cartesian coordinates. The rest of the seven blocks are a slightly deformed variation of the cubed sphere blocks to make them connect to the central cube without gaps but still provide a spherical outer boundary.

r_1 is the radius of the global spherical domain and r_0 the half edge length of the central cubical block. In the simulations presented in this chapter these parameters are set to $r_0 = 1.0$ and $r_1 = 3.0$.

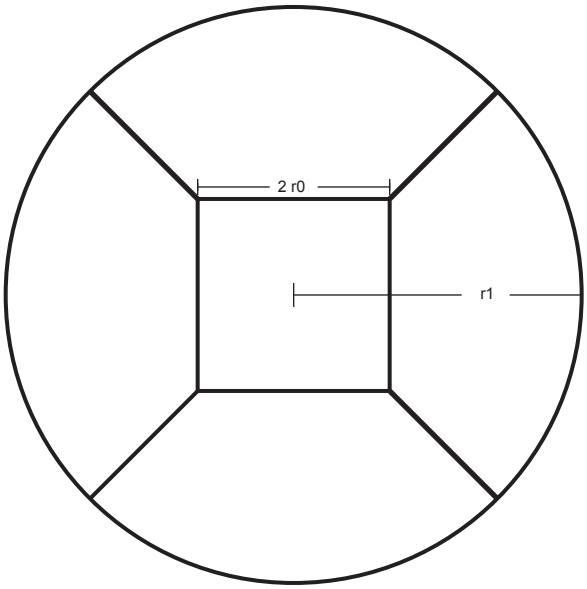

Figure 7: Sketch of an equatorial cut through the seven block system (see also Fig. 3). The edge length of the central cubical block is $2r_0$, the total radius of the spherical domain called r_1. The center of this spherical block system coincides with the origin of the global coordinate system. For runs in this chapter the dimensions of the domain are specified by $r_0 = 1$ and $r_1 = 3$.

For doing convergence tests resolutions of $\Delta a = \Delta b = \Delta c = 0.1$ to $\Delta a = \Delta b = \Delta c = 0.0125$ are used which correspond to grid points per block of between 21^3 to 161^3.

The simulations were stopped at time $t = 10$. As mentioned above the units are chosen so that the propagation speed of the waves is one. Given that the diameter of the domain is 6, $t = 10$ corresponds to about 1.67 crossing times.

3.4 Results

Accuracy and convergence with respect to the known plane wave analytic solution were tested using the setup described above with a wide variety of finite differencing operators. The operators looked at are D_{2-1}, D_{4-2}, D_{4-3}, D_{6-3}, D_{6-5} and D_{8-4}. The first number denotes the convergence order in the interior of a grid and the second number the convergence order at the boundaries.

For all of the operators the expected convergence order was found. Details about all these runs are given in reference [60]. As an example the D_{8-4} and D_{6-5} operators are discussed here – these are the ones that are later used for the black hole simulations – and then a comparison of accuracy for most of the other implemented operators is shown.

Fig. 8 displays the convergence exponent for D_{8-4} computed from runs with two different resolutions and comparing the errors with respect to the exact solution. The convergence exponent n is then computed as

$$n = \frac{\log\left(\frac{E_1}{E_2}\right)}{\log\left(\frac{h_1}{h_2}\right)} \tag{47}$$

where h_1 and h_2 denote the local grid spacing in either of these runs and E_1 and E_2 are a measure for the error with respect to the analytic solution. Since it is the strongest test for convergence and accuracy , typically the infinity norm is used, i.e. the maximum of the error.

Three convergence tests have been performed with increasing resolution and all of these tests show fifth order accuracy as expected [56, 57]. The periodicity that is seen in the plots corresponds to the periodicity of the wave solution and can be explained by a changing number of maxima and minima in the wave as it propagates through the simulation domain.

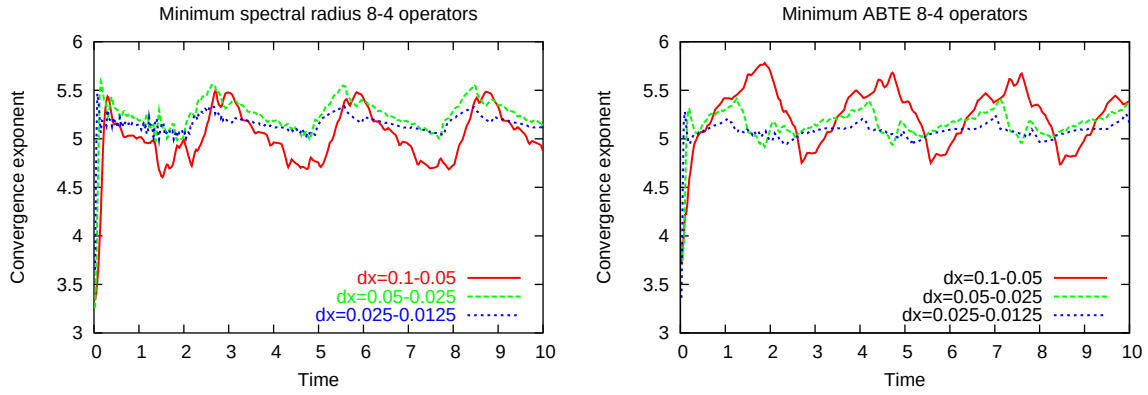

Figure 8: Convergence exponents for the minimum spectral radius (top) and the minimum ABTE (bottom) D_{8-4} operators.

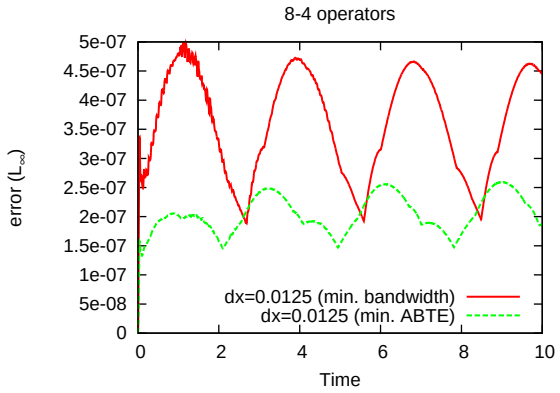

Figure 9: Comparison of the accuracy of the two D_{8-4} operator types shown in the previous figure in the L_∞ norm. Although both operators have quite similar error coefficients, there is up to a factor of two difference in the errors seen in the actual runs.

Fig. 9 is a comparison of the L_∞ norm of two D_{8-4} operators constructed by applying different optimization criteria. For one of them the free parameters were chosen so that

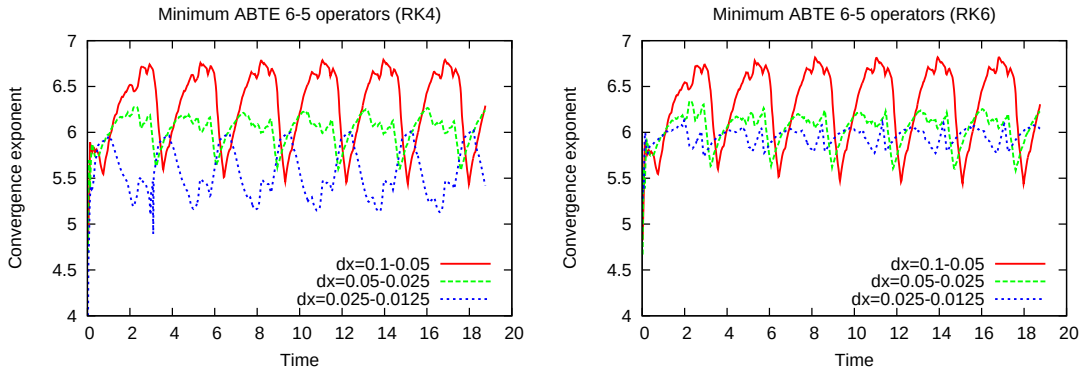

Figure 10: Convergence for the optimized D_{6-5} operator with dissipation and Runge–Kutta time integrators of order four (top) and six (bottom), respectively. A slightly lower convergence order for the highest resolution is seen when RK4 is used. This effect is not present with the RK6 integrator. The lower convergence order indicates that the accuracy of the spatial finite differencing operators is high enough, so that the overall error is dominated by the accuracy of the time integrator.

they minimize the bandwidth of the operator, the other one was constructed to minimize the average boundary truncation error (ABTE). Even though both operators have comparable error coefficients, in the actual numerical results roughly a factor of two difference can be seen.

Convergence exponents for runs using the D_{6-5} operator are shown in Fig. 10. When using an RK4 time integrator the spatial truncation error at the highest resolutions gets so small that the global accuracy is affected by the lower convergence order of the time integration. That manifests itself in the left plot of Fig. 10. For the highest resolution runs the global convergence order drops down from the expected value of six to a number between five and six. If a sixth order accurate Runge Kutta time integrator (RK6) is used, as shown on the right panel, the truncation error in the time integrator gets smaller and even for the highest resolution runs that were done the spatial differencing errors dominate. The global convergence exponent stays at approximately six for all three tests that were done.

Fig. 11 compares the errors resulting from using a larger selection of finite differencing operators at two different resolutions $\Delta x = 0.1$ and $\Delta x = 0.0125$. Fig. 12 again compares the errors resulting from different operators this time at a fixed $t = 4.4$, all the resolutions that were used in the convergence tests and two choices for an error measure: the infinity norm and the L_2 norm. This plot can be used as a guideline for which operator to choose for a given resolution. Note that the errors change by orders of magnitude depending on the choice of operator at a given resolution. For the tests shown here, D_{6-5} is the best choice, in terms of convergence order as well as accuracy. It should be noted that the higher order methods only pay off when going to high enough resolutions. In the same way the errors converge faster with increasing resolution, they also grow faster when decreasing resolution compared to lower order operators. For example at $h = 0.1$, the errors of D_{8-4} are a bit larger D_{4-3} (which is computationally cheaper to compute), while at the highest resolution it is about one order of magnitude less.

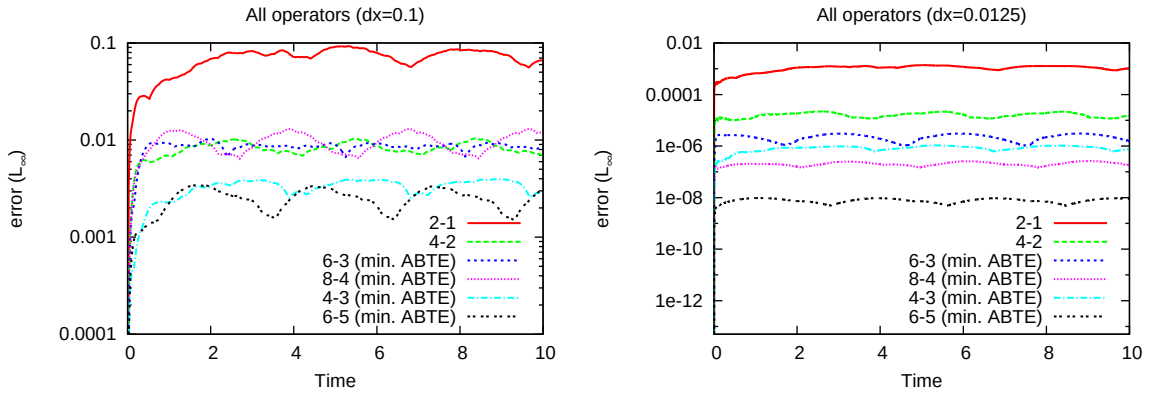

Figure 11: Comparison of the L_∞ errors for all the new, optimized, differencing operators constructed in this thesis. The left (right) plot shows a comparison of all the unique and optimized operators at low (high) resolutions. The most successful operators are the optimized D_{6-5}, D_{4-3}, and D_{8-4}.

3.5 Local vs. Global Coordinate Basis

In Chap. 2.2.5 the point was made that the basis in which the tensor components are expressed does not need to be identical to the coordinates in which the partial derivatives

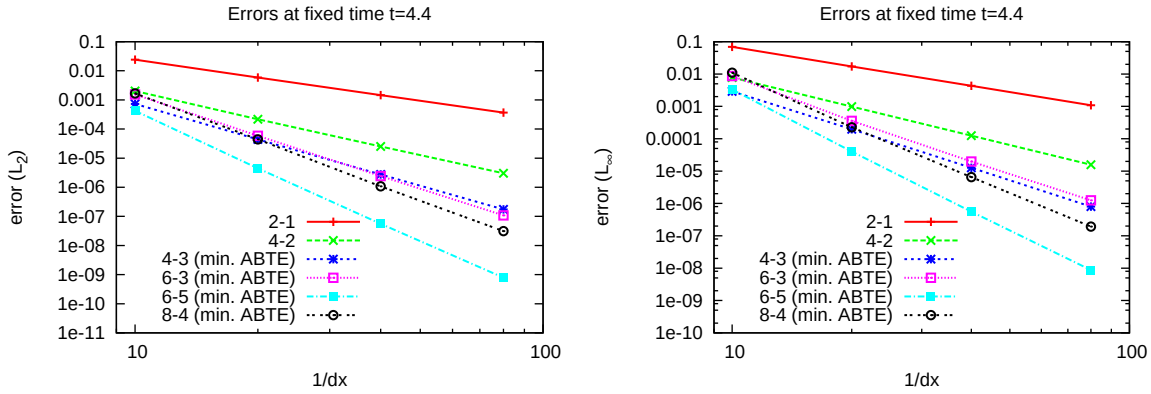

Figure 12: Comparison of the errors at $t = 4.4$ for all resolutions. The left (right) plot shows the L_∞ (L_2) errors.

and finite differencing operators are written. Using a different basis for the tensor components requires to transform the spatial partial derivatives in the evolution equations according to Eq. (14). Choosing a global tensor basis, i.e. one that is common to all of the individual blocks will simplify the treatment of inter block boundary conditions considerably.

Shown is a numerical comparison between runs following the specifications given in Chap. 3.3. A numerical resolution of $21 \times 21 \times 21$ grid points on each block, including the central cubical one is used. The test is done applying the D_{6-5} finite differencing operators.

With a patch-local tensor basis and diagonal norm operators, the system is strictly stable. The numerical error at a given resolution is bounded by a constant. With a global tensor basis on the other hand, strict stability has not been shown and a small amount of artificial dissipation is required for stability. Because of the D_{6-5} operators being constructed from a restricted full norm, dissipation is required here for both types of tensor bases. Therefore compatible artificial dissipation is added to the system of both Mattson-Svärd-Nordström and Kreiss-Oliger type. A description of these dissipation operators is given in Chap. 2.3.4. The dissipation coefficient is chosen to be $\epsilon = 3.0$, the

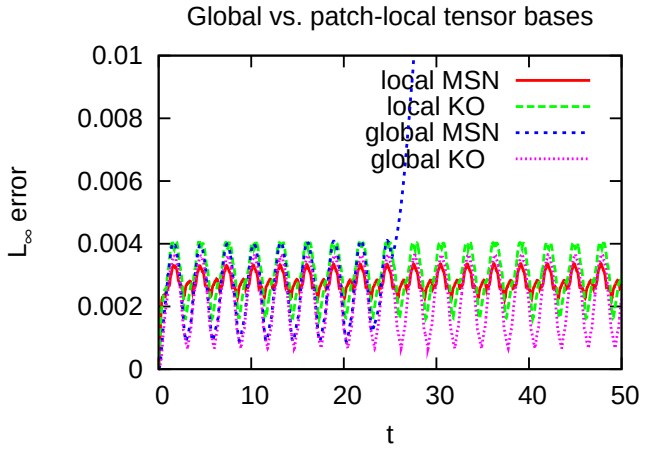

Figure 13: Comparing global and patch-local tensor bases, and Mattsson–Svärd–Nordström (MSN) and Kreiss-Oliger (KO) dissipation operators. The graphs show the L_∞ norm of the solution error vs. time for a coarse resolution on a seven-block system. Some artificial dissipation is necessary to stabilise the system, since it has non-constant coefficients. For this particular value of the dissipation strength ϵ, using a global tensor basis is unstable with the MSN dissipation operators, but stable with the KO operators. With higher values of ϵ, the system is stable for both dissipation operators.

size of the transition region is 0.3 times the size of the block. The whole system is then sixth order accurate.

The numerical results are shown in Fig. 13. Shown is the L_∞ norm of the numerical error function, i.e. the difference between the numerical and the known exact solution. The simulation was run up to a time of $t = 50$ where as previously the crossing time is about $1.67M$. The discretization using MSN dissipation is unstable with the global tensor basis formulation. It was found that increasing the dissipation parameter ϵ to values above 3.0 will stabilize the system. In the patch-local tensor basis formulation even for $\epsilon = 3.0$ instabilities are not seen. Using the Kreiss-Oliger dissipation operators, a dissipation strength of 3.0 is sufficient for both tensor bases to keep the simulation stable. In terms of accuracy, i.e. the actual value of the numerical error, all cases, except when going unstable, are similar. The influence of the tensor basis on global accuracy does not seem to be relevant. Therefore the choice of the tensor basis changes the numerical simulation

mainly in the sense that depending on the choice, a different amount of dissipation is necessary for stability. That justifies the pragmatic approach to use a global basis for the more complicated general relativistic code, where the added simplicity makes the code more readable and debugging simpler.

4 Quasinormal Mode Excitation of Kerr Black Holes

4.1 Introduction

One of the most useful methods to explore the response of black holes to external perturbations is based on wave scattering [69]. Early studies identified three main stages in the dynamics of a wave propagating on a black hole background, as observed at a fixed spatial point. In a first, transient phase the observed wave depends on the structure of the initial pulse. Vishveshwara and Press discovered that this initial "burst" is invariably followed by a second phase characterized by exponentially decaying oscillations: this phase is usually referred to as "quasinormal ringing" [70, 71]. In the third and last stage of the evolution, waves slowly die off as a power law tail [72].

Astrophysical black holes should be well described by the Kerr solution, since charge is unlikely to play a major role in astrophysical scenarios (see e.g. [17] for a discussion). As a consequence of the "no hair theorem", if general relativity is the correct theory of gravity, the quasinormal mode (QNM) frequencies of a Kerr black hole depend only on its mass and angular momentum. Earth-based and space-based gravitational wave detectors have the potential to measure the frequency and damping time of a QNM. From these two observables one can infer the black hole's mass and angular momentum [73, 74]. For the space-based *Laser Interferometer Space Antenna* (LISA) and possibly also for second-generation ground-based detectors, the signal-to-noise ratio can be large enough that one will be able to identify *two* or more QNM frequencies in the signal [75]. A multi-mode detection would provide a striking, direct test of the Kerr nature of the source (i.e., of the no-hair theorem). The basic idea is quite simple. Roughly speaking, the first mode in the pair is used to determine the black hole's mass and angular momentum, and the other mode(s) to verify that the QNM spectrum is indeed consistent with a general relativistic Kerr black hole [76].

The combined observation of supermassive black hole binary inspiral and ringdown with LISA can provide even more information [77]. Parameter estimation during the inspiral phase can be very accurate, depending on the black holes' masses, spins and distance [78]. Combining information from the inspiral and ringdown phases one can estimate the energy radiated in the merger, and possibly improve parameter estimation from both phases (see e.g. [79] for a preliminary study of this effect in the context of earth-based detectors).

In the last thirty years the development of gravitational wave astronomy motivated a detailed investigation of the QNM frequency spectrum [80, 81, 82]. In comparison, the problem of the *relative excitation* of QNMs received very little attention (see e.g. [83] and references therein). One especially needs information about relative excitation amplitudes for physically realistic, strong sources of gravitational waves like binary black holes which have good chances of being detected by current or next generation interferometers. Therefore, ideally, the relative QNM excitation should be determined by general relativistic simulations of (for example) binary black hole mergers. Despite recent progress, this information is not yet available [84]. Given the recent progress of numerical relativity, by the time LISA flies one could have a good knowledge of the multipolar distribution of the energy and angular momentum radiated in a black hole merger under generic conditions. Knowing in advance which modes should be excited in a realistic merger will not only be useful to probe the Kerr nature of the source, but also to reduce the number of templates needed to perform matched filtering on ringdown waveforms.

In this chapter a quantitative investigation of QNM excitation is presented studying a simple model problem: the scattering of scalar waves on a Kerr background. This problem can be studied in the framework of black hole perturbation theory analytically. Instead of that, here the scalar field is evolved with a three dimensional finite differencing code that applies the multi-block methods described in the previous chapters. The results are compared with results from analytic perturbation methods, partly to test the accuracy of

the applied methods in cases for which the perturbative results are known to be correct to a high accuracy and partly to provide independent numerical results in cases for which it is not clear how well approximations and assumptions that go into the perturbative calculations hold. An example for the first case is the quasinormal frequency spectrum of a Schwarzschild black hole; an example for the second case is the excitation strength of quasinormal modes for an observer at a finite distance from the black hole. From here on, analytic results from perturbation theory are just called *perturbative results* as opposed to the *numerical results* from the simulations.

Even though the work was done in three dimensions, due to the advantages of the multi-block code, the results are more accurate than previous studies using two-dimensional codes [85, 86]. Krivan *et al.* [85] studied the late time dynamics and the rotational coupling of massless scalar fields in a Kerr background, but not their quasinormal ringing. Later they extended the analysis to gravitational perturbations, considering both the late time tail and the quasinormal ringing phase [86]. For large rotation the damping times of corotating fundamental modes in [86] are accurate within $\sim 3\%$ when compared to results from perturbation theory; the accuracy reached with the 3D code ($\sim 0.3\%$) is roughly an order of magnitude better. In fact, it was possible to extract the frequencies of some *overtones* with an error of the order of a few percent or less.

Given the high accuracy of the multi-block infrastructure, a careful extraction of the QNM content of the waveforms becomes necessary. The so-called *time-shift problem* (exponential dependence of the quasinormal amplitudes on the time at which the quasinormal ringing regime starts) is discussed in detail, how it affects the determination of both absolute and relative QNM amplitudes, and how to choose pairs of modes so as to decrease the uncertainty on relative amplitudes. A general criterion (based on minimizing a suitably defined residual) to determine the optimal fitting window to extract QNM frequencies and amplitudes is introduced. These tools are used to study the absolute and relative amplitudes of corotating and counterrotating modes for Gaussian initial data located in

the far zone. The dependence of these amplitudes on the radial shape of the initial data is looked at, and excellent agreement with results from perturbation theory [83] is found. Also discussed is the problem of extracting overtones for modes with a given angular dependence, finding that the first overtones of corotating modes (e.g. modes with $l = m = 2$) contribute significantly to the waveform for rapidly rotating black holes.

4.2 The Continued Fractions Method for Computing Quasinormal Modes

In this chapter perturbations of black holes are studied by evolving the time dependent wave equation directly as opposed to analytical perturbative calculations. The first attempts to compute quasinormal frequencies took this approach [70] and due to the ever increasing computational resources and development of numerical schemes and codes, this approach can still provide new results today. The advantage of numerical evolutions is mainly that they can produce results for fairly general physical situations, for which it is not necessarily known how well perturbative approximations hold. For example predictions about initial perturbations and observers at finite distances from the black hole can be performed and, given that the numerical details are under control, will converge towards the correct solution. Also how to apply boundary conditions to these kind of initial value problems is well understood. The disadvantage is higher computational cost, compared to other methods and problems extracting enough information about the modes from the data. As described in Chap. 4.9, modes can be extracted by Fourier transformations or by fitting to a quasinormal ringdown function. With both methods it is only possible to reliably extract the two or three strongest modes in the waveform. This is not at all due to insufficient numerical accuracy but because higher overtones typically decay so fast that their contribution is extremely small during most of the quasinormal ringing phase.

An alternative method for computing quasinormal mode frequencies was presented in 1985 by Leaver [87]. It can be applied to Schwarzschild, Kerr and with some modifications

Reissner-Nordström black holes and it is very accurate even for very high overtones. In the following subsections numerical results from simulations will frequently be compared to results computed by that method. Here a quick overview of the basis of this method is given. This discussion follows closely the more detailed description in [88].

The one dimensional wave equation for the function $\Phi(r)$ with a potential $V(r)$ can be written as

$$\partial_t^2 \Phi + \left(-\partial_r^2 + V(r)\right) \Phi = 0. \tag{48}$$

The Regge-Wheeler equation that describes odd parity linear perturbations of a Schwarzschild black hole (for other types of perturbations the discussion and analysis is similar) is of that form. In that case Φ would be the so called Regge-Wheeler function that represents the perturbation and $V(r)$ is a potential that depends on the black hole parameters and the spin and angular structure of the perturbing field.

For simplicity this discussion is restricted to smooth solutions with compact support. Also the potential is chosen to be positive $V(r) \geq 0$ and vanishing for $|r| > r_0$. Note that this is generally not the case for the potentials that show up in the Regge-Wheeler formalism. All solutions with compact support are bounded, i.e. $|\Phi| < C$. The Laplace transform of the of Φ is

$$\hat{\Phi}(s, x) = \int_0^\infty e^{-st} \Phi(t, x) dt. \tag{49}$$

Eq. (48) for the transformed field is

$$s^2 \hat{\Phi} - \hat{\Phi}'' + V \hat{\Phi} = s\Phi(0, r) + \partial_t \Phi(0, r). \tag{50}$$

Solutions to that equation are

$$\hat{\Phi}(s, r) = \int_{-\infty}^\infty G(s, r, r') j(s, r') dr' \tag{51}$$

with the Green function

$$G(s,r,r') = \frac{1}{W(s)} \begin{cases} f_-(s,r')f_+(s,r), & (r' < r) \\ f_-(s,r)f_+(s,r'), & (r' > r), \end{cases} \tag{52}$$

two arbitrary solutions to the homogeneous part (i. e. the right hand side set to zero) of Eq. (50), f_- and f_+, and their Wronskian $W(s)$. j is the inhomogeneity of Eq. (50). The quasinormal frequencies are defined as the complex numbers s_n for which the two solutions to the homogeneous equations become linearly dependent:

$$f_+(s_n,r) = c(s_n)f_-(s_n,r). \tag{53}$$

The corresponding $f_+(s_n,r)$ are the so called quasi eigenfunctions and the Green function is singular at $s = s_n$. The solution to the Regge-Wheeler equation is computed by the inverse Laplace transform

$$\Phi(t,r) = \frac{1}{2\pi \mathrm{i}} \int_{-\infty}^{\infty} e^{(a+\mathrm{i}s)t} \hat{\Phi}(a+\mathrm{i}s,x) ds, \tag{54}$$

a complex line integral ($a > 0$).

In Leaver's method, also called continued fractions method, a series representation of f_- is assumed to represent also f_+ for the values of the quasinormal frequencies. This method may work if f_+ is bounded which would be the case for *normal modes*. For *quasinormal modes* this is generally not clear, since f_+ grows exponentially. In spite of that, the method works very well numerically. With an improved version of it Nollert was able to compute quasinormal modes up to a mode number of 100000 and could numerically show the asymptotic distribution of modes [89]. Some insight about how that method works is given in [90].

For Kerr black holes this leads to two coupled equations, one for the radial and one for the angular dependence of the perturbation. For both of them recurrence relations for the coefficients of the series expansion can be found and used to compute the quasinormal modes.

4.3 Evolution Equations and Background Geometry

The evolution equations used in this chapter to study scalar quasinormal modes, are identical to the ones described in Chap. 3.2 except that the flat background metric is replaced by the metric of a single rotating black hole in Kerr Schild coordinates. Explicitly the background metric is given as

$$ds^2 = \eta_{\mu\nu} + 2Q l_\mu l_\nu dx^\mu dx^\nu \tag{55}$$

with $\eta_{\mu\nu}$ the Minkowski metric, and

$$\begin{aligned} Q &= \frac{Mr}{r^2 + a^2 \left(z/r\right)^2}\,, & (56)\\ r^2 &= \frac{1}{2}(\rho^2 - a^2) + \sqrt{\frac{1}{4}(\rho^2 - a^2)^2 + a^2 z^2}\,, & (57)\\ \rho^2 &= x^2 + y^2 + z^2\,. & (58) \end{aligned}$$

Here M is the mass and $a = jM$ is the angular momentum per unit mass of the black hole (j is the dimensionless spin parameter, $0 \leq j \leq 1$). In Cartesian coordinates, the null vector l_μ is given by

$$l_\mu dx^\mu = dt + \frac{rx + ay}{r^2 + a^2} dx + \frac{ry - ax}{r^2 + a^2} dy + \frac{z}{r} dz\,. \tag{59}$$

This form of the Kerr-Schild metric has become of common use in numerical relativity. However, in these coordinates the shape of the Cauchy and event horizons become

more and more ellipsoidal with increasing spin[3]. For $j \gtrsim 0.96$ it is not possible to fit a spherical excision boundary between these horizons any more. This is illustrated in Fig. 14. Although one could in principle choose a different shape for the excision boundary within the code, instead coordinates for which both horizons are always spherical, and therefore an excision sphere can always fit between them are used. This version of the Kerr Schild coordinates is related to the "standard" one defined above by the following transformation:

$$\tilde{x} = x - \frac{ay}{r}\,, \tag{60}$$

$$\tilde{y} = y + \frac{ax}{r}\,, \tag{61}$$

$$\tilde{z} = z\,. \tag{62}$$

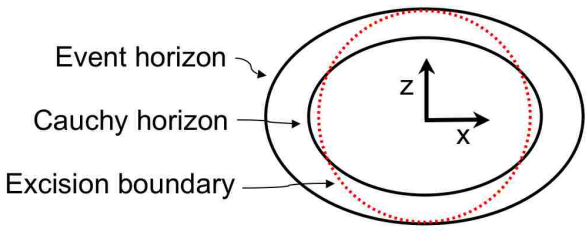

Figure 14: Event and Cauchy horizons for a Kerr black hole with spin $j \gtrsim 0.96$ in "standard" Kerr-Schild coordinates (as defined in the text), here shown in the x-z plane. The horizons have an ellipsoidal shape; it is therefore not possible to fit a spherical excision region (dotted line) between the two horizons.

4.4 Initial and Boundary Conditions

The QNM excitation depends on the structure of the scalar field that is used as a perturbation. To excite certain modes in a controlled way, one chooses initial data of the form

$$\Phi = A \exp\left(-\frac{(r-r_0)^2}{\sigma^2}\right) Y^{(\ell,m)}\,, \tag{63}$$

[3]The author thanks Harald Pfeiffer for pointing this out.

$$\Pi = B \exp\left(-\frac{(r-r_0)^2}{\sigma^2}\right) Y^{(\ell,m)}\,, \tag{64}$$

$$d_i = \partial_i \Phi\,. \tag{65}$$

Unless otherwise stated, throughout this chapter the initial data location is fixed to $r_0 = 20M$ and $\sigma = M$. $Y^{(\ell,m)}(\theta,\phi)$ denotes the ordinary spherical harmonics. Since the Kerr background is not spherically symmetric, one should really expand the perturbation in terms of spin-weighted spheroidal harmonics ${}^{(s)}S^{(\ell,m)}(j\omega)$ of spin weight $s = 0$. Using spherical harmonics weakly excites other modes through rotational mode mixing; this point will be discussed in more detail below, in Chap. 4.10.

The changes in the characteristic length scale in the radial direction are usually small over time. To accurately resolve the propagating waves all the way to the outer boundary a constant resolution in the radial direction of the cubed sphere coordinates is used. As mentioned, the coordinates are set up so that the spherical inner (excision) boundary is placed between the event and Cauchy horizons, and no boundary conditions need to be applied there. For global stability maximally dissipative boundary conditions are chosen at the outer boundary, and they are applied through penalty terms as described in Sec 2.3.2. That works analogous to the inter-block boundary treatment, except that the ingoing modes (that enter the computational domain) are not taken from a neighboring block but constructed according to the type of boundary condition one wants to apply.

4.5 Multi-Block Setup

The setup laid out in the previous chapters is inherently an axisymmetric problem that could be solved for each m independently with a two dimensional code. Nonetheless the approach is taken to evolve the full set of three dimensional equations, making use of the multi-block infrastructure described above. The following considerations will make clear that this problem can be treated numerically in an efficient way by that approach:

The goal is to model the ring down of the scalar field, before the power law tail decay sets in at late times. To get a sufficiently complete picture of that phase, an observer located at a certain radius $r_{\rm obs}$ needs to be able to monitor the field for a time of about $100M$ from the moment on that the first signal from the black hole reaches him, while still being causally disconnected from the outer boundary and errors that might get induced there. Given that the center of the Gaussian in the initial data is typically around $2M - 20M$ and the observer location between $2M - 30M$, an evolution time of around $150M$ is required with outer boundaries located at about $200M$.

The excision sphere is placed between the event and the Cauchy horizon and will be, depending on the spin of the black hole, located between $1M$ and $2M$.

To resolve the dynamics going on close to the horizon it was found that a radial resolution of at least $\Delta r = 0.1M$ is necessary, i.e. 2001 grid points in radial direction are needed. In the angular directions 21×21 grid points are used. On the other hand, the characteristic feature length of the data in the angular directions is not expected to change much during the course of the evolution. Given that the angular part of the initial data is resolved well, the angular resolution should be sufficient for all times and all radii. As it is clear from the description of the cubed sphere coordinates in Chap. 2.2.4 this multi-block grid structure fulfills exactly those requirements. The fact that it provides a constant angular resolution is the primary reason why three dimensional simulations of the outlined problem can be done in an efficient way.

An additional benefit coming from the cubed sphere coordinates is that waves can be extracted from the numerical data easily without the need for interpolation or similar more complicated methods, since one can use constant r coordinate spheres for the wave extraction.

4.6 Specifications for the Simulations

Spatial finite-differencing operators that satisfy summation by parts are used; they are eighth order accurate in the interior and fourth order accurate at and close to the bound-

aries. With those operators a global accuracy of order five is expected [56, 57] (see Chap. 3 and reference [60] for more details on the operators that are used). A fourth order accurate Runge Kutta time integrator is applied. This does not spoil the expected global fifth order spatial convergence, since a small enough time step is chosen so that the truncation errors generated by the time integration are smaller than those that originate from the spatial finite differencing (see Chap. 3 and reference [60] for details on the code's convergence).

In multi-block simulations one does not necessarily have a uniform or isotropic grid spacing in a global coordinate system. Since in all of the simulations presented the global grid spacing in the radial direction is smaller than in the angular directions, the radial direction is used for the time step criterion $\Delta t = \lambda \Delta r$, where λ —usually referred to as the Courant factor— is chosen to be $\lambda = 0.25$.

Fig. 15 shows a typical waveform that results when extracting the real part of the $\ell = 2, m = 2$ mode from the simulations. The initial data are set up according to Eq. (4.4), with the specific choice $A = 0$, $B = 1$, $\sigma = M$ and $r_0 = 20M$. The background Kerr black hole has a spin $j = 0.9$. The strongest modes in this waveform are $(\ell = 2, m = 2, n = 0)$ and $(\ell = 2, m = -2, n = 0)$, where n labels the overtones, $n = 0$ being the fundamental mode. A fit for those two modes is shown together with the numerical data. For details about how that fit was done, see Chap. 4.9. The third strongest component in the data is the $(\ell = 2, m = 2, n = 1)$ mode, i.e. the first overtone. Since this mode is decaying much faster than the fundamental mode, it only plays a role at early times. That is the reason why the fit, done for only the two fundamental modes, is drifting away from the numerical data at times below $50M$ (overtones will be analyzed explicitly in Chap. 4.12).

4.7 Overview of Quasinormal Mode Extraction

The time evolution of perturbations of a Kerr black hole can be split into three stages. After a first burst of radiation depending on the source of the excitation, the perturbation field Φ undergoes exponentially damped oscillations (ringdown phase). Finally, in the tail phase (caused by back-scattering of radiation off the background gravitational potential)

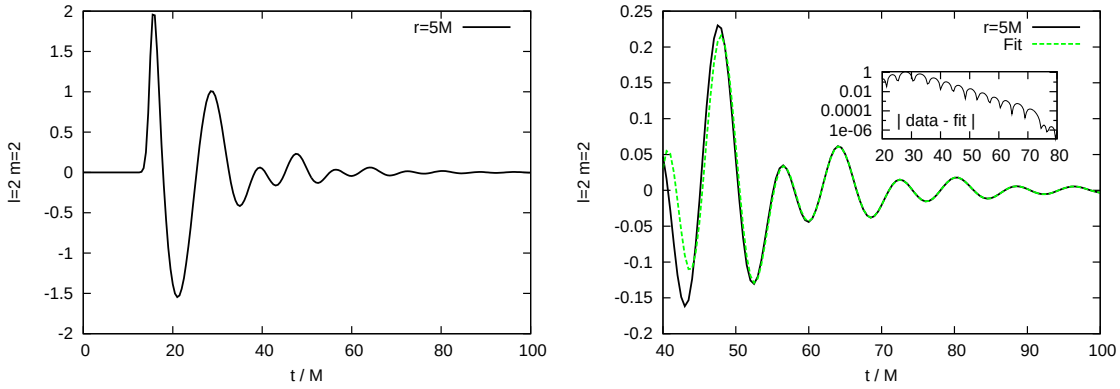

Figure 15: The left panel shows the $\ell = m = 2$ component of the waveform extracted at radius $r = 5M$ on a Kerr black hole background with a spin of $j = 0.9$. The waveform is a superposition of the corotating and the counterrotating mode, and the beating of two different frequencies is clearly visible. The right panel shows the waveform for $t \geq 40M$ as well as a QNM fit with the fundamental $\ell = |m| = 2$ modes. The interval used for the fit is $[74.5M, 150M]$. The inlay shows the absolute value of the difference between the fit and the data. At times between the excitation of the QNM ($t \sim 25M$) and about $70M$ the differences are mainly due to the presence of the $(l = 2, m = 2, n = 1)$ mode (i.e. the first overtone), the exponentially decaying mode that can be seen in the inlay (a fit of this mode yields quasinormal frequencies in agreement with perturbation theory). At times $t \lesssim 25M$ the difference is due to the initial burst.

the field follows a power-law decay. In this thesis the focus is on the ringdown stage. The different multipole components of the solution are extracted by integrating the scalar field against different spherical harmonics over surfaces of constant observer radius r:

$$\Phi^{(\ell,m)}(r,t) = \int \bar{Y}^{(\ell,m)}(\theta,\phi)\Phi \; d\Omega \,, \tag{66}$$

where the bar denotes complex conjugation. Usually multipole components are considered up to $\ell = 4$ and all values of m ($|m| \leq \ell$). By adding up the contributions of all multipoles one should recover the full scalar field:

$$\int_r \Phi^2 d\Omega = \sum_{\ell=0}^{\infty} \sum_{m=-\ell}^{\ell} (\Phi^{(\ell,m)})^2 \,. \tag{67}$$

As already mentioned, the rotation of the black hole and numerical errors can excite multipole components which are not present in the initial data. The above property can be used to check for the existence of overtones or modes with $\ell > 4$ that are not explicitly extracted but might be present in the solution (e.g. due to rotational mode mixing, numerical errors, or both). Multipoles with $m \neq 0$ require some care. The spherical harmonics $Y^{(\ell,m)}(\theta,\phi)$ are given by

$$Y^{(\ell,m)}(\theta,\phi) = \sqrt{\frac{2\ell+1}{4\pi}\frac{(\ell-m)!}{(\ell+m)!}} P^{(\ell,m)}(\cos\theta) e^{\mathrm{i}m\phi} \,, \tag{68}$$

where $P^{(\ell,m)}(\theta)$ is a real function (an associated Legendre polynomial). Therefore the initial data of a pure multipole with $m \neq 0$ will be complex. Given that the evolution equations are linear, one can evolve the real and imaginary parts of Φ separately, and obtain the complex solutions for positive and negative m by linear combinations of the form

$$\Phi^{(\ell,m)} \;\; = \;\; \mathcal{R}(\Phi^{(\ell,m)}) + \mathrm{i}\mathcal{I}(\Phi^{(\ell,m)}) \,, \tag{69}$$

$$\Phi^{(\ell,-m)} \;=\; \mathcal{R}(\Phi^{(\ell,m)}) - \mathrm{i}\mathcal{I}(\Phi^{(\ell,m)})\,. \tag{70}$$

$\mathcal{R}(\Phi^{(\ell,m)})$ and $\mathcal{I}(\Phi^{(\ell,m)})$ are the real and imaginary parts of $\Phi^{(\ell,m)}$ respectively. This point is important for the extraction of the relative amplitude of corotating and counterrotating modes. In fact, as stressed (for example) in Ref. [75, 87], QNMs of Kerr black holes always come "in pairs". In the Kerr case, for a given multipole (ℓ, m) one has to solve an eigenvalue problem to determine both the quasinormal frequencies $\omega^{(\ell,m,n)}$ and the angular separation constant $A^{(\ell,m,n)}$ (not to be confused with the mode amplitude $\mathcal{A}^{(\ell,m,n)}$ introduced below), used to separate the angular and radial dependence of the Teukolsky equation and write it as two ordinary differential equations. For *each* $(\ell, m \neq 0)$ and $j \neq 0$ the eigenvalue problem admits *two* sets of solutions. In addition to (ℓ, m), one labels the modes of each set by the overtone index n, denoting the frequencies by $\omega_{(i)}^{(\ell,m,n)}$ $(i = 1, 2)$. For given (ℓ, m, n), the solutions corresponding to the two different sets have different values of $\omega^{(\ell,m,n)}$ (and also of $A^{(\ell,m,n)}$):

$$\omega_{(1)}^{(\ell,m,n)} \neq \omega_{(2)}^{(\ell,m,n)}\,.$$

Both the real and imaginary parts are different. In fact, the real part of one of the frequencies is positive and the other one is negative:

$$\mathcal{R}(\omega_{(1)}^{(\ell,m,n)}) > 0\,, \qquad \mathcal{R}(\omega_{(2)}^{(\ell,m,n)}) < 0\,.$$

If one considers instead the frequencies corresponding to the pair $(\ell, -m)$, they are related to those of (ℓ, m) by a simple symmetry property:

$$\begin{aligned} -\mathcal{R}(\omega_{(i)}^{(\ell,m,n)}) = \mathcal{R}(\omega_{(j)}^{(\ell,-m,n)})\,, \qquad & \mathcal{I}(\omega_{(i)}^{(\ell,m,n)}) = \mathcal{I}(\omega_{(j)}^{(\ell,-m,n)})\,, \\ \bar{A}_{(i)}^{(\ell,m,n)} = A_{(j)}^{(\ell,-m,n)}\,, \qquad & (i, j = 1, 2\,; i \neq j)\,. \end{aligned} \tag{71}$$

In this sense, any solution with positive m is nothing but the "mirror image" of a solution with opposite real part and opposite m (see Fig. 6 of [75] for an illustration of this). For $m = 0$ (or for any value of m in the Schwarzschild case) the two "mirror solutions" are degenerate in modulus of the frequency and damping time. However, in general, a multipolar component with a given (ℓ, m) will always contain a superposition of *at least* two different damped exponentials. Because of this, it is enough to consider only one frequency for each mode [(ℓ, m) or $(\ell, -m)$], since the other two frequencies are obtained through this symmetry property; the standard convention of considering, for each mode, the frequency with positive real part is followed. Below is a detailed discussion of the excitation of these modes, extending previous work by Krivan *et al.* [86].

When the perturbation field is in the quasinormal ringing regime, it can be expanded as a QNM sum of the form

$$\Phi^{(\ell,m)}(r,t) \approx \mathcal{R}\left\{\sum_{n=0}^{\infty} \mathcal{A}^{(\ell,m,n)} e^{\mathrm{i}c^{(\ell,m,n)}} e^{-\mathrm{i}\omega^{(\ell,m,n)}(t-t_0)}\right\}, \tag{72}$$

where $\mathcal{A}^{(\ell,m,n)}$ is the amplitude of the n-th overtone with angular structure given by the pair (ℓ, m), $c^{(\ell,m,n)}$ its phase, $\omega^{(\ell,m,n)}$ its complex quasinormal frequency and t_0 (which to a first approximation is assumed to be the same for all modes) marks the time at which the quasinormal regime starts.

The extraction of gravitational waves from numerical simulations of the full Einstein equations requires the observer to be located far away (in the wave zone). This aspect is covered in detail in Chap. 5. For the extraction of QNM frequencies, on the other hand, it is not problematic to place the observer close to the black hole, since an observer at any point in the space-time is in general expected to measure the same frequencies. In fact, a small r is better suited for extracting quasinormal frequencies from the simulations simply because outer boundary effects pollute the waveform later, and the ringing regime can be

observed for a longer time. The availability of a longer ringdown waveform improves the accuracy of the fitting procedure that is applied to extract the frequencies.

Table 3: Quasinormal frequencies computed by Leaver's continued fraction method (here labeled "perturb.") and by the time domain simulations, with the associated relative differences. 21×21 points are used in the angular direction on each block and a resolution of $0.1M$ in the radial direction. For $j = 0.9$ the frequencies as seen by observers located at different radii r are compared. Observers at larger radii measure frequencies with larger errors, since boundary effects start to contaminate the waveform earlier.

r	j	l, m	$\omega_{\rm perturb.}$	$\omega_{\rm numerical}$	rel. difference (Re,Im)
$5M$	0.0	2, 0	$0.48364 - 0.09676$i	$0.48364 - 0.09676$i	$< 10^{-5}$
	0.5	2, 0	$0.49196 - 0.09463$i	$0.49190 - 0.09469$i	$4.27 \times 10^{-4}, 6.34 \times 10^{-4}$
	0.5	2, -2	$0.42275 - 0.09562$i	$0.42281 - 0.09569$i	$1.42 \times 10^{-4}, 7.32 \times 10^{-4}$
	0.5	2, 2	$0.58599 - 0.09349$i	$0.58589 - 0.09339$i	$1.71 \times 10^{-4}, 1.07 \times 10^{-3}$
	0.9	2, 0	$0.51478 - 0.08641$i	$0.51471 - 0.08646$i	$1.36 \times 10^{-4}, 5.79 \times 10^{-4}$
	0.9	2, -2	$0.38780 - 0.09379$i	$0.38781 - 0.09339$i	$2.58 \times 10^{-5}, 4.26 \times 10^{-3}$
	0.9	2, 2	$0.78164 - 0.06929$i	$0.78144 - 0.06955$i	$2.56 \times 10^{-4}, 3.75 \times 10^{-3}$
	0.98	2, 2	$0.89802 - 0.04090$i	$0.90940 - 0.04018$i	$1.27 \times 10^{-2}, 1.76 \times 10^{-2}$
	0.98	2, -2	$0.38177 - 0.09338$i	$0.38234 - 0.09743$i	$1.49 \times 10^{-3}, 4.34 \times 10^{-2}$
$20M$	0.9	2, -2	$0.38780 - 0.09379$i	$0.38694 - 0.09471$i	2.22×10^{-3}, 9.81×10^{-3}
	0.9	2, 2	$0.78164 - 0.06929$i	$0.78244 - 0.06670$i	1.02×10^{-3}, 3.74×10^{-2}
$40M$	0.9	2, -2	$0.38780 - 0.09379$i	$0.38406 - 0.09958$i	9.64×10^{-3}, 6.17×10^{-2}
	0.9	2, 2	$0.78164 - 0.06929$i	$0.78292 - 0.06618$i	1.64×10^{-3}, 4.49×10^{-2}

The effect of the observer's location on the result is illustrated in Table 3, where the frequencies of $(\ell = 2, m = \pm 2)$ fundamental modes for a Kerr black hole with spin $j = 0.9$ as measured by observers at radii $r = 5M$, $20M$ and $40M$ are listed. $t_0 = r + r_0$ in Eq. (72) and $A = 0$, $B = 1$ in Eq. (4.4) was chosen. The results presented in this Table are discussed in more detail below (Chap. 4.9). Here it is simply pointed out that quasinormal frequencies measured at different radii are very close to the analytical predictions, supporting the statement that the observer does not need to be far away from the black hole to extract the correct ringdown frequencies. Indeed, *for these particular simulations* the relative error increases with r: the main reason, as explained, is that

observers located at large radii see boundary effects earlier, so they can only measure a shorter ringdown waveform with respect to observers closer to the black hole.

4.8 The Time-Shift Problem

Here the so-called *time-shift problem* is discussed, how it affects the extraction of quasinormal frequencies and amplitudes from numerical simulations, and a possible way to address it. Even though in this chapter scalar perturbations are considered, the discussions of this and other chapters apply also to other types of black hole perturbations.

The standard approach is to choose t_0 in Eq. (72) using some approximate calculation based, for example, on the location of the initial data and the time it would take for initial data to be scattered by the black hole potential and reach the observer, usually assuming that perturbations propagate with coordinate speed one (as they would in flat space-time). Criteria like this are well motivated and provide a good guess, but there is still an uncertainty in t_0. For example, the coordinate speed of the perturbation in a curved background in general will not be one. One might expect that such a small uncertainty would not influence the extraction of physically relevant quantities. However, as discussed below, this is not the case: there are quantities of interest to gravitational wave detection which have a strong dependence on t_0. Following the existing literature, this is called the *time-shift problem*.

Suppose the starting time t_0 is subject to an uncertainty δ_0. Under a change

$$t_0 \to t_0 + \delta_0 \,, \tag{73}$$

the amplitude and phase of each mode change according to

$$\mathcal{A}^{(\ell,m,n)} \;\to\; \mathcal{A}'^{(\ell,m,n)} = \mathcal{A}^{(\ell,m,n)} e^{-\delta_0 \mathcal{I}\left(\omega^{(\ell,m,n)}\right)} \,, \tag{74}$$

$$c^{(\ell,m,n)} \;\to\; c'^{(\ell,m,n)} = c^{(\ell,m,n)} + \delta_0 \mathcal{R}\left(\omega^{(\ell,m,n)}\right) \,. \tag{75}$$

That is, an uncertainty in t_0 induces a linear uncertainty in the phase, and an *exponential* uncertainty in the amplitude. Fortunately other quantities are largely independent of this uncertainty: for example, the QNM frequencies $\omega^{(\ell,m,n)}$ are unaffected by δ_0.

How large can one allow this exponential amplification of errors to be? Impose the requirement on the amplitude uncertainty induced by the starting-time uncertainty δ_0 to be less than some small number ϵ, that is

$$\left|\frac{\mathcal{A}'^{(\ell,m,n)}-\mathcal{A}^{(\ell,m,n)}}{\mathcal{A}^{(\ell,m,n)}}\right| = \left|e^{-\delta_0\mathcal{I}\left(\omega^{(\ell,m,n)}\right)}-1\right| < \epsilon\,.$$

For small ϵ this implies

$$|\delta_0| \lesssim \left|\frac{\epsilon}{\mathcal{I}\left(M\omega^{(\ell,m,n)}\right)}\right| M\,. \tag{76}$$

For the $\ell=2$ fundamental scalar mode in the Schwarzschild background (which is spherically symmetric, so that the choice of m becomes irrelevant) $|\mathcal{I}\left(M\omega^{(2,0,0)}\right)| = 0.09676 \simeq 10^{-1}$. In other words, if one wants to determine the amplitude of this mode within 1% ($\epsilon = 10^{-2}$) one needs to know t_0 with an uncertainty $\delta_0 \lesssim 0.1M$. Constraints on δ_0 are even tighter for overtones, since they decay faster and the exponential propagation of errors is more dramatic.

In practice, what is most interesting is the *relative* amplitude between different modes. Under a change of the form (73) this relative amplitude changes according to

$$\frac{\mathcal{A}^{(\ell,m,n)}}{\mathcal{A}^{(\ell',m',n')}} \to \left(\frac{\mathcal{A}^{(\ell,m,n)}}{\mathcal{A}^{(\ell',m',n')}}\right)' = \frac{\mathcal{A}^{(\ell,m,n)}}{\mathcal{A}^{(\ell',m',n')}} e^{-\delta_0\mathcal{I}\left(\omega^{(\ell,m,n)}-\omega^{(\ell',m',n')}\right)}\,. \tag{77}$$

Following the same reasoning one finds the constraint

$$|\delta_0| \lesssim \left|\frac{\epsilon}{M\mathcal{I}\left(\omega^{(\ell,m,n)}-\omega^{(\ell',m',n')}\right)}\right| M\,. \tag{78}$$

Consider for example the relative amplitude between the fundamental mode and the first overtone. For Schwarzschild black holes and small values of n the typical difference in the imaginary part of the frequency for two consecutive overtones ($\ell' = \ell$, $m' = m$, $n' = n+1$) is

$$M\mathcal{I}\left(\omega^{(\ell,m,n)} - \omega^{(\ell',m',n')}\right) \simeq 0.2\,.$$

Setting again $\epsilon = 10^{-2}$ the maximum allowed uncertainty on the starting time would be quite small: $\delta_0 \lesssim 0.05M$ (this presumably already precludes assuming that the perturbation propagates with speed one, as in flat space-time).

Suppose one wants to resolve corotating and counterrotating components of the fundamental mode with $\ell = 2$ (say, the components with $m = \pm\ell$). In the case of a spinning black hole background these QNM frequencies are different, but their imaginary parts are actually quite close for most values of the rotation rate [87, 75]. For example, looking at Tab. 3 one can see that for spin $j = 0.5$ the difference is $|M\mathcal{I}\left(\omega^{(2,2,0)} - \omega^{(2,-2,0)}\right)| \simeq 0.00212$, so that $\delta_0 \lesssim 4.7M$. Even for a rapidly rotating black hole with $j = 0.9$ the difference is not as large as between a fundamental mode and its overtone: $M\mathcal{I}\left(\omega^{(2,2,0)} - \omega^{(2,-2,0)}\right) \simeq 0.0245$, and $\delta_0 \lesssim 0.4M$.

Critical starting-time uncertainties for $\epsilon = 10^{-2}$, general values of the spin and different pairs of modes are plotted in Fig. 16. Determining the relative amplitude of a fundamental mode and of the first overtone is generally harder, unless corotating modes and near-extremal black holes are considered, as it is done in Chap. 4.12. The spin dependence of δ_0 is quite weak for overtones, but δ_0 can change by orders of magnitude for modes with different angular dependence ($\ell \neq \ell'$ or $m \neq m'$). For $j \lesssim 0.5$ the time-shift problem, as defined here, becomes irrelevant when one wants to determine the relative amplitude of components with the same l and different m's. The reason is simply that modes with different m's have the same QNM frequency in the Schwarzschild limit, so that $\delta_0 \to \infty$. As a rule of thumb, determining the relative amplitude of angular components with the

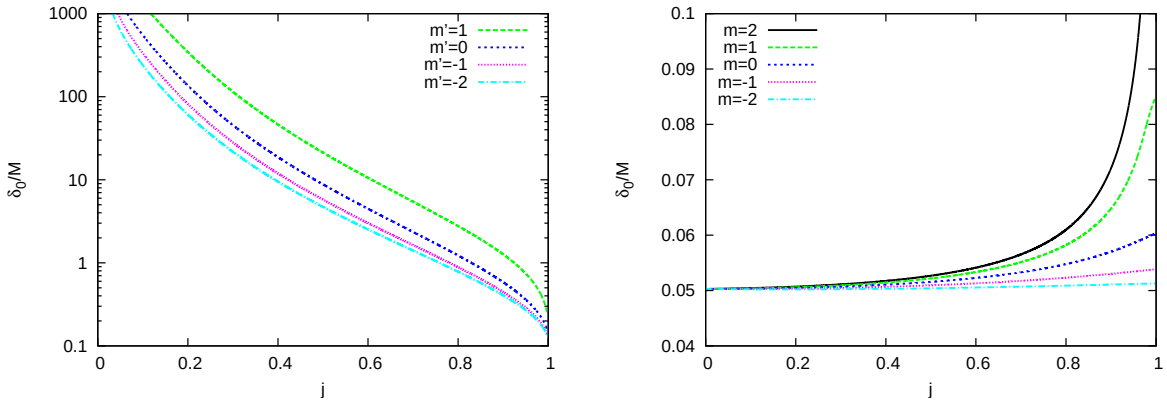

Figure 16: Critical uncertainty in the starting time, as defined by Eq. (78), assuming $\epsilon = 10^{-2}$. In the left panel the critical δ_0 is given for fundamental modes ($n = n' = 0$) with different angular dependence. For the first mode $\ell = m = 2$ is assumed; the second mode has $\ell' = 2$ and different values of $m' = 1, 0, -1, -2$ (lines from top to bottom). In the right panel the critical uncertainty in the relative amplitude of the fundamental mode and first overtone, i.e., $n = 0$ and $n' = 1$ is shown. Here $\ell = \ell' = 2$ is set, all values of $m = m'$ are considered and once again $\epsilon = 10^{-2}$ is assumed.

same l and different m's is harder for large rotation. However, as said before, even for $j = 0.9$ the critical uncertainty is $\delta_0 \gtrsim 0.4M$, an order of magnitude larger than the typical uncertainty to resolve overtones (which in most cases is $\sim 0.05M$). Most of the qualitative features of Fig. 16 are also seen in the experimental problem of resolving different QNMs in the actual detection of a ringdown signal (compare e.g. Figs. 3, 4 and 18 of [75]).

In Chap. 4.11 and Chap. 4.12 the extraction of corotating and counterrotating modes and of overtones will be studied in more detail, respectively. In preparation for this study, in the next chapter the general method by which we extract quasinormal frequencies from the numerical waveforms is outlined.

4.9 Optimal Choice of Fitting Interval

Once one has the different multipole components of the numerical solution, one can analyze them by applying a fitting procedure to each of these components. Since each mode decays exponentially while oscillating with its quasinormal frequency, the obvious function to fit the numerical waveform is Eq. (72), where the free parameters are the amplitudes,

phases and frequencies. As discussed in Chap. 4.12, only in some cases it was possible to fit for overtones, in the sense of getting their expected quasinormal frequencies with reasonable accuracy. However, as described below, the residual that one gets by truncating the sum at the fundamental mode is already quite small (see also Fig. 15).

This subsection deals with extracting the quasinormal frequencies from the numerical data. To a very good approximation the frequencies are independent of t_0, and one can therefore pick any value for the latter. One still needs to find a good choice for the time interval $[T_i, T_f]$ over which the ringdown dominates and the fitting procedure works best. Since in principle the parameters obtained from the fitting might depend on the choice of this time interval, the procedure applied here will be described in detail.

Only during the ringdown phase does the waveform have the functional behavior of Eq. (72), so the time interval $[T_i, T_f]$ should not include the transient regime and the tail phase. For the simulations described here it was found reasonable to pick $T_f = 150M$, since for $T > T_f$ the system typically goes into the tail phase. The choice of T_i is more delicate: small values would bring the fitting time window out of the ringdown phase, but large values would make the fitting interval small and the resulting fit inaccurate. It was decided to take a pragmatic approach: for different values of T_i one computes the (relative) residual $R(T_i, t_0)$ between the fitted function and the numerical data, which is defined as

$$R(T_i, t_0) = \left(\sum_{t_j=T_i}^{T_f} |\Phi_{\rm data}(t_j) - \Phi_{\rm fit}(t_j, t_0)| \right) \left(\sum_{t_j=T_i}^{T_f} |\Phi_{\rm data}(t_j)| \right)^{-1} \tag{79}$$

Then a value of T_i that minimizes the residual is chosen. In a very well defined sense, this gives an optimal choice for T_i. In principle one could use other norms (for example, a sum over squares instead of a sum over absolute values), but it was checked that this does not affect significantly the results of presented here. Choosing the value of T_i that minimizes

the residual defined above should not be confused with the minimization procedure done at each T_i to get the fit itself.

Instead of extracting the quasinormal frequencies through a fitting procedure, in principle one could also perform a Fourier transform of the solution, as in Ref. [86]. However it was found that the fitting procedure provides a far superior accuracy, even in cases with relatively few sampling points. Nonetheless a comparison to the results that were obtained by Fourier analysis has been done and consistency between both methods was confirmed.

Fig. 17 shows the residual as a function of T_i for one of the simulations (the one corresponding to spin $j = 0.5$ and $\ell = m = 2$ initial data in Tab. 3). The residual is independent of the choice of excitation time t_0, since a change in t_0 is just absorbed in the amplitude of the fitting function, leaving the other fitting quantities unaffected.

Since the black hole's spin is non-zero, both $m = 2$ and $m = -2$ modes are present in the solution. Here the discussion is restricted to the $m = 2$ part of the numerical solution. The $m = -2$ part behaves similarly (in Chap. 4.11 a detailed study of the relative amplitudes of corotating and counterrotating modes is presented).

From Fig. 17 it can be seen that $R(T_i, t_0)$ has a rather sharp local (and global) minimum. By computing the derivative (through finite differences) of the residual with respect to T_i one finds that the minimum is located at $T_i = (59.65 \pm 0.025)M$. The uncertainty refers to the difference between two consecutive values of T_i, which is in turn given by the time step for this simulation: $\Delta t = 0.025M$.

Fig. 18 shows the real and imaginary parts of the frequency extracted from the same simulation as a function of T_i. By evaluating them at $T_i = (59.65 \pm 0.025)M$ one gets $\omega_R = 0.585887 \pm 1 \times 10^{-6}$ and $\omega_I = 0.0933851 \pm 5 \times 10^{-7}$.

Fig. 18 also reveals that ω changes very little within the interval $50M \lesssim T_i \lesssim 80M$. Since the choice of T_i is by no means unique —for example a different definition of the residual would slightly shift T_i— this plateau in the frequencies guarantees that the phys-

ical quantities that are extracted are not too sensitive to that uncertainty. This means that the errors in the numerically extracted QNM frequencies due to the choice of T_i are quite small.

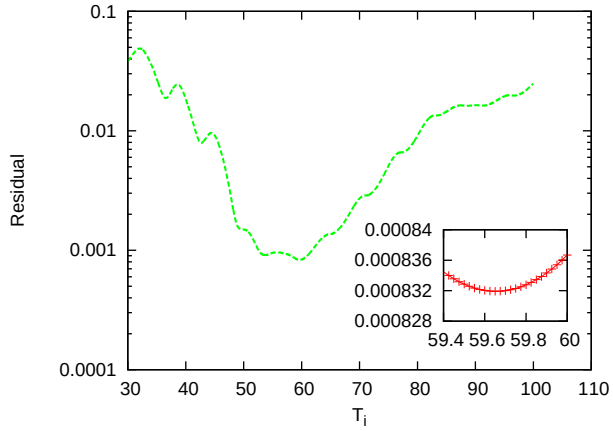

Figure 17: Residual in the fit, as defined in Eq. (79), as a function of the initial time for the fitting T_i. Looking at the minimum of the residual one can determine T_i with high precision. This plot corresponds to a simulation with spin $j = 0.5$, $\ell = m = 2$ initial data with $A = 0$, $B = 1$ and a radial resolution $\Delta r = 0.1M$.

The quasinormal frequencies obtained from the numerical data can now be examined in the way just described. Tab. 3 shows the frequencies computed in [83] using Leaver's continued fraction method for perturbed Kerr black holes with spin $j = 0$, 0.5, and 0.9 (here labeled *perturb.*). Along with these frequencies values extracted from the time domain evolutions (labeled *numerical*) and the relative differences between the two are listed. The numerical values were obtained by evolving different initial data sets with $A = 0$ and $(\ell = 2, m = 0, \pm 2)$ in Eq. (4.4), and fitting for the multipoles present in the initial data (additional multipoles generated by rotational mode mixing are discussed below). For $j = 0$ the frequencies do not depend on m, therefore only results for $m = 0$ are shown. Even with a relatively modest resolution, the differences on quasinormal frequencies from the three-dimensional simulations in Tab. 3 are between one and two orders of magnitude smaller than the ones reported in previous two-dimensional, axisymmetric simulations of gravitational perturbations [86].

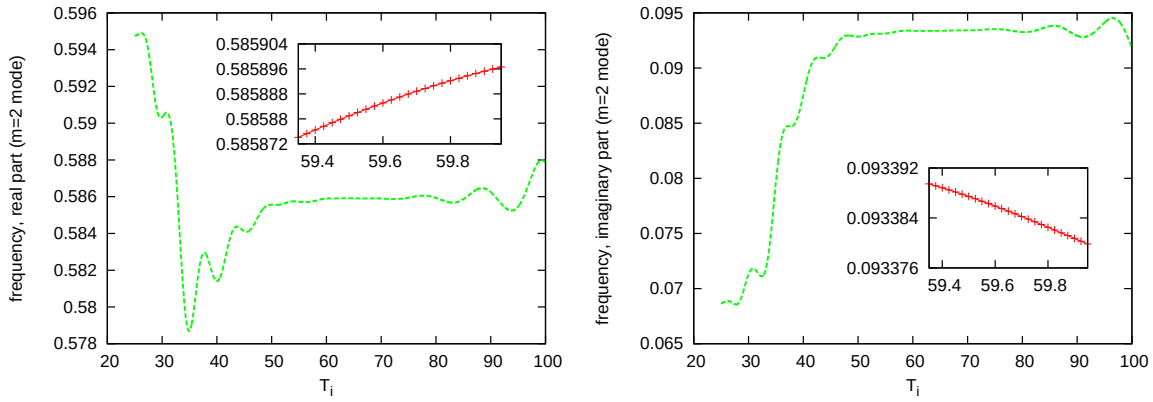

Figure 18: The left and right panels show the real and imaginary parts of the quasinormal frequencies extracted from the simulations in Fig. 17. From the optimal starting time determined by minimizing the residual, $T_i = (59.65 \pm 0.025)M$ (see previous figure), one finds $\omega_R = 0.585887 \pm 1 \times 10^{-6}$ and $\omega_I = 0.0933851 \pm 5 \times 10^{-7}$.

4.10 Rotational Mode Mixing

In Chap. 4.4 the initial data family sets are described, which were expanded in spherical harmonics. Since the Kerr background is not spherically symmetric one should not expand the perturbation in terms of spherical harmonics, but (more rigorously) in terms of the spin-weighted spheroidal harmonics ${}^{(s)}S^{(\ell,m)}(a\omega)$, where s is the spin weight of the perturbing field, $a = jM$ is the black hole spin per unit mass, and ω is the frequency in a Fourier expansion of the perturbation (a quantitative discussion of spin-weighted spheroidal harmonics and more references can be found in [91]). However, as first shown by Press and Teukolsky [92], the ${}^{(s)}S^{(\ell,m)}$'s may be expanded as a power series in $a\omega$:

$$ {}^{(s)}S^{(\ell,m)} = {}^{(s)}Y^{(\ell,m)} + (a\omega) \sum_{\ell' \neq \ell} c_{\ell'\ell m} \, {}^{(s)}Y^{(\ell',m)} + \mathcal{O}(a\omega)^2 \, . \tag{80} $$

Here ${}^{(s)}Y^{(\ell,m)}$ denotes a spin-weighted spherical harmonic of spin-weight s. The focus of this chapter lies on scalar perturbations ($s = 0$), in which case the spin-weighted spherical harmonics reduce to ordinary spherical harmonics. The coefficients $c_{\ell'\ell m}$ are related to the more familiar Clebsch-Gordan coefficients [92, 91]. As a result of (80), and because of

the orthogonality of the (spin-weighted) spherical harmonics, inner products of different spheroidal harmonics will be given by inner products of *spherical* harmonics with higher-order corrections in $a\omega$. At least for small $a\omega$, one may expect these contributions to be small. In fact, the corrections turn out to be small even for moderately large values of $a\omega$ (see [91] for an explicit calculation of the inner products at the QNM frequencies). Nevertheless, using spherical harmonics instead of spheroidal harmonics can induce a small amount of mode-mixing in the initial data.

For a spherically symmetric background space-time, initial data with different values of ℓ evolve separately and the angular structure of each mode is preserved during evolution. On the other hand, for a Kerr background with non-zero spin, modes with different values of ℓ do couple and furthermore, modes that are not present in the initial data can be excited during evolution. This may make it necessary to increase the angular resolution compared to the non-rotating case to resolve the higher ℓ modes generated during evolution. However, the decay rate of these modes increases with ℓ, so even when modes with higher values of ℓ are generated during evolution, they do not dominate. Therefore, it was found that if one accurately resolves the angular structure initially, the same is in general true for the whole evolution.

Fig. 19 illustrates rotational mode coupling for non-zero spin backgrounds (see also [93] and [94] for numerical studies of mode-mode coupling). Since modes with same m but different ℓ can couple to each other, the extracted $(\ell = 4, m = 2, n = 0)$ waveform is shown (for three simulations with different spin parameters) excited by initial data whose angular dependence is given by an $\ell = m = 2$ spherical harmonic. As expected, the rotationally-induced excitation of the $(\ell = 4, m = 2)$ mode typically increases with spin. Some additional mode mixing is an artifact of the symmetry of the computational grid. This "spurious" mode mixing is present also for $j = 0$, but it converges to zero as the angular resolution is increased. All other extracted modes, up to $\ell = 4$ and all allowed values of m, are within roundoff error throughout the simulations.

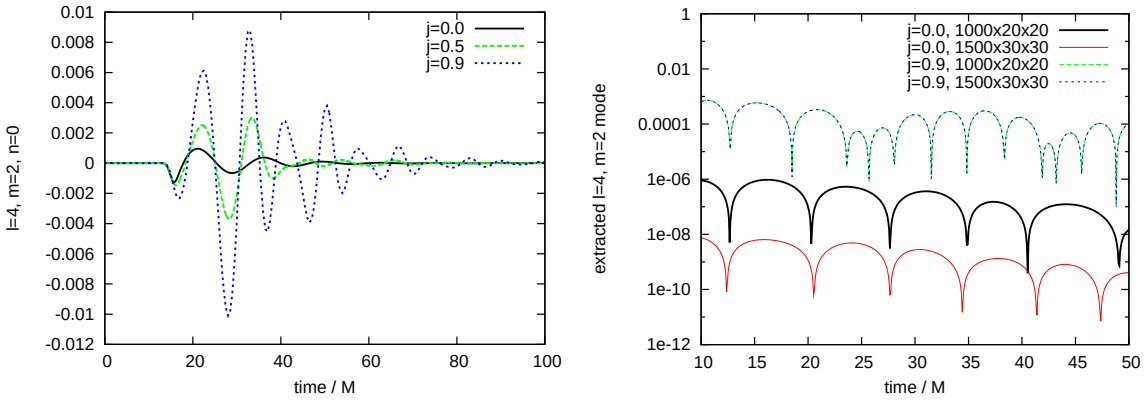

Figure 19: The left panel shows the extracted $(\ell = 4, m = 2, n = 0)$ waveform for three simulations with different spin parameters as seen by an observer at $r_{\rm obs} = 5M$. The initial data are a pure $(\ell = m = 2)$ mode and are set up according to Eq. (4.4) with $A = 0$, $B = 1$ and $r_0 = 20M$. For zero spin the different multipole components of the solution should evolve independently and no modes besides the one in the initial data should be excited, while for non-zero spin modes with different ℓ but same m do couple [86]. In the Schwarzschild case the $(\ell = 4, m = 2, n = 0)$ waveform differs from zero due to the used grid structure and discretization errors, but it converges to zero with increasing resolution. This is illustrated by the right panel, which shows the extracted $(\ell = 4, m = 2, n = 0)$ amplitude for $j = 0$ and $j = 0.9$ from runs with two resolutions ($20 \times 20 \times 1000$ and $30 \times 30 \times 1500$ points per block and outer boundaries at $100M$). Only for $j = 0.0$ the mode converges to zero.

Since QNMs are extracted only up to $\ell = 4$ one needs to test whether there is a relevant contribution from higher modes that are not extracted explicitly. In the absence of $\ell > 4$ modes, summing up all extracted modes up to $\ell = 4$ one should recover the full field, according to Eq. (67). The result of this test for a spinning black hole with $j = 0.9$ is shown in Fig. 20: at the level of accuracy needed in the presented work, extracting modes with $\ell \leq 4$ is sufficient.

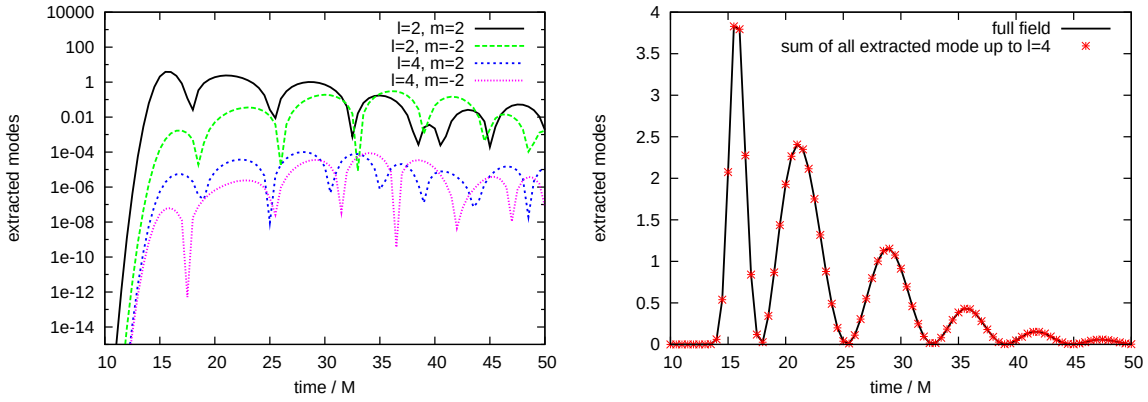

Figure 20: Results from a run with initial data parameters $\ell = m = 2$ and spin $j = 0.9$. The left panel shows the amplitude of all modes up to $\ell = 4$ which are not within the roundoff error. The right panel shows the sum over those modes compared to the full field: the two curves lie on top of each other, and there is no relevant contribution from higher modes.

4.11 Excitation Factors for Co- and Counterrotating Modes

It is known that in the quasinormal ringing regime, the field will behave according to Eq. (72). In the previous subsection the values predicted in Ref. [83] for the frequencies were verified through simulations. Now also the amplitudes of each mode, as predicted in that same reference, are tested against the numerical simulations.

Assume that the observer and the initial data are located far away from the black hole (these assumptions underlie the "asymptotic approximation" adopted in [95, 83]). From Eq. (4.15) of [83], when $B = 0$ the response of the black hole in the ringdown phase

should be well approximated by a QNM decomposition of the form

$$\Phi^{(\ell,m)}(r,t) \approx -\frac{r_0}{r}\sqrt{\pi}\sigma\mathcal{R}\left\{\sum_{n=0}^{\infty}(\mathrm{i}A\omega^{(\ell,m,n)})B^{(\ell,m,n)}e^{-\frac{1}{4}\left(\sigma\omega^{(\ell,m,n)}\right)^2}e^{-\mathrm{i}\omega^{(\ell,m,n)}(t-r_0-r_*)}\right\}, \quad (81)$$

In the simulations done here $A = 0$ is set, in which case it can easily be shown that the previous expression becomes

$$\Phi^{(\ell,m)}(r,t) \approx -\frac{r_0}{r}\sqrt{\pi}\sigma B\mathcal{R}\left\{\sum_{n=0}^{\infty}B^{(\ell,m,n)}e^{-\frac{1}{4}\left(\sigma\omega^{(\ell,m,n)}\right)^2}e^{-\mathrm{i}\omega^{(\ell,m,n)}(t-r_0-r_*)}\right\}, \quad (82)$$

With respect to [83] an extra factor r_0/r has been added. This is because Eq. (4.15) in [83] refers to the Sasaki-Nakamura function $X^{(\ell,m)}_{(0)}(r,t)$, which is related to the Teukolsky function $\Phi^{(\ell,m)}(r,t)$ that is used in the evolutions by the relation $X^{(\ell,m)}_{(0)}(r,t) = (r^2+a^2)^{1/2}\,\Phi^{(\ell,m)}(r,t)$ (see the discussion in App. C of [83]). The focus lies on large values of r, for which the asymptotic approximation holds and $X^{(\ell,m)}_{(0)}(r,t) \simeq r\Phi^{(\ell,m)}(r,t)$. The transformation between the Teukolsky and Sasaki-Nakamura functions must also be taken into account when comparing the initial data in Eq. (4.14) of [83] with the initial data used, Eq. (4.4). Assuming $\sigma \ll r_0$ and $r \gg 1$ this comparison yields the normalization factor r_0 in the equations above.

The scalar QNM frequencies $\omega^{(\ell,m,n)}$ and the scalar excitation factors $B^{(\ell,m,n)}$ are listed in Table I and Table III of [83], respectively. In that reference and in Eq. (81) Boyer-Lindquist coordinates are used; since in the simulations Kerr-Schild coordinates are used one needs to transform Eq. (81) appropriately. Since Φ is a scalar, the transformation is straightforward. The transformation of the initial data is more subtle, since the slices are different. One would expect that whenever the asymptotic approximation is valid the difference between the slices should not be too important. The results discussed below and explicit comparisons between evolutions using both coordinate systems in the non-

spinning case [96] confirm this expectation. Details on how the transformation of the initial data and the field itself is done are given in App. B.

To check the accuracy of Eq. (82), for rest of this chapter an analysis of evolutions of different initial data sets is done, all of them consisting of a combination of $(\ell = 2, m = 2)$ and $(\ell = 2, m = -2)$ modes with $A = 0$ and $B = 1$. The dependence of the amplitudes of the counter- and co-rotating *fundamental* modes (in the next subsection overtones will be studied) on the width σ of the initial data [cf. Eq. (4.4)] is explored numerically. In order to assess more quantitatively the effect of the *time-shift problem* (see Chap. 4.8) first the value of the width maximizing these amplitudes is compared. Given that all the initial data sets that are considered are centered at the same radius, the reasonable assumption can be made that locally (that is, around the width for which the amplitudes are maximal) t_0 is approximately the same for each set. If t_0 were *exactly* the same, the value of t_0 used would not change the width at which the maximum amplitude is located, since changes in t_0 would only involve a global rescaling of all amplitudes, as discussed in Chap. 4.8. Therefore the hope is that within the setting described for the simulations the width for which the amplitudes are maximal does not depend too sensitively on t_0.

The numerical results shown here were obtained with the same number of points in the angular direction as above. Half of the radial resolution was used (that is, $\Delta r = 0.2M$) for a rough scan of a large σ range, and again the original resolution around the maxima of the amplitudes. Initial data with varying widths σ and $r_0 = 20M$ were chosen (as in the simulations above) and an observer placed at $r = 40M$, for which the asymptotic approximation holds reasonably well [96]. $t_0 = r_{\text{initial data}} + r$ was chosen (that is, $t_0 = 60M$ in the cases considered), which is approximately the time the initial data pulse needs to propagate to the black hole and back to the observer.

Fig. 21 and (more quantitatively) Tables 4 and 5 show the excitation amplitudes as functions of the width of the Gaussian σ from our numerical simulations. At first the results given here could be interpreted as an approximate verification of the predictions of

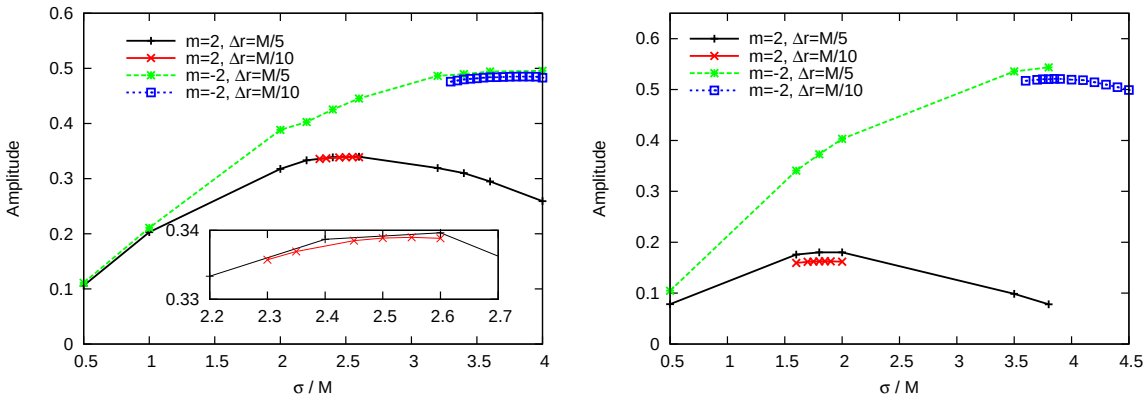

Figure 21: Numerically obtained excitation amplitudes of the $\ell = |m| = 2$ fundamental modes assuming an observer location $r_{\rm obs} = 40M$ and a ringdown starting time $t_0 = 60M$. The left panel refers to a black hole with spin $j = 0.5$. According to predictions from perturbation theory in the asymptotic approximation [cf. Eq. (81) and the following discussion] the maximum for $m = 2$ should be located at $\sigma^{(2,2,0)} = 2.445$, while the value that obtained from the simulations is $\sigma^{(2,2,0)} = 2.55 \pm 0.05$ (the uncertainty describing the difference between consecutive values of σ used in the simulations here: $\Delta\sigma = 0.05$). Similarly, for $m = -2$ the width at the maximum should be $\sigma^{(2,-2,0)} = 3.434$, while the simulations give a value of $\sigma^{(2,-2,0)} = 3.875 \pm 0.075$. The right panel, in turn, refers to a black hole with spin $j = 0.9$. In this case the theoretical (numerical) maxima are located at $\sigma^{(2,2,0)} = 1.816$ ($\sigma^{(2,2,0)} = 1.85 \pm 0.05$) and $\sigma^{(2,-2,0)} = 3.758$ ($\sigma^{(2,-2,0)} = 3.85 \pm 0.05$), respectively. The inset in the left panel is a zoom around the maximum for $j = 0.5$ and $m = 2$. As discussed in the text, an uncertainty in the excitation time of $0.09M$ would already explain the difference between the predicted location of the maxima and the numerical results shown here.

Table 4: Excitation amplitudes for $j = 0.5$, $\ell = 2$ and $n = 0$ for initial perturbations of variable Gaussian width σ, as displayed in Fig. 21. The observer location in these runs is $r = 40M$. Highlighted are the maxima in the amplitudes of the different m-modes. Also shown are the relative amplitudes of the two modes, and the relative differences between the values predicted by perturbation theory and the ones extracted from the numerical simulations. The amplitudes are given for the wave expressed in Boyer-Lindquist coordinates (see appendix B for details) and are multiplied by a factor of r/r_0 to get them in an observer independent form.

	numerical results			perturbation theory			relative difference
σ	$\mathcal{A}^{(2,2,0)}$	$\mathcal{A}^{(2,-2,0)}$	$\frac{\mathcal{A}^{(2,-2,0)}}{\mathcal{A}^{(2,2,0)}}$	$\mathcal{A}^{(2,2,0)}$	$\mathcal{A}^{(2,-2,0)}$	$\frac{\mathcal{A}^{(2,-2,0)}}{\mathcal{A}^{(2,2,0)}}$	$\frac{\mathcal{A}^{(2,-2,0)}}{\mathcal{A}^{(2,2,0)}}$
2.30	0.3357	0.411	1.22	0.315	0.419	1.33	0.080
2.35	0.3369	0.410	1.22	0.314	0.423	1.35	0.097
2.45	0.3385	0.420	1.24	0.311	0.430	1.38	0.103
2.50	0.3389	0.425	1.25	0.310	0.433	1.40	0.102
2.55	**0.3390**	0.430	1.27	0.308	0.436	1.42	0.104
2.60	0.3388	0.435	1.28	0.306	0.439	1.43	0.105
3.30	0.315	0.476	1.51	0.253	0.449	1.77	0.149
3.35	0.311	0.478	1.54	0.248	0.448	1.81	0.149
3.40	0.308	0.480	1.56	0.243	0.446	1.84	0.151
3.45	0.304	0.481	1.58	0.238	0.445	1.87	0.154
3.50	0.301	0.482	1.60	0.233	0.443	1.90	0.158
3.55	0.297	0.483	1.63	0.228	0.441	1.93	0.159
3.60	0.293	0.484	1.65	0.223	0.439	1.97	0.161
3.65	0.289	0.484	1.67	0.217	0.437	2.01	0.168
3.70	0.285	0.4843	1.70	0.212	0.434	2.05	0.170
3.75	0.281	0.4848	1.73	0.207	0.432	2.09	0.173
3.80	0.276	0.4850	1.76	0.202	0.429	2.12	0.173
3.85	0.272	**0.4851**	1.78	0.196	0.425	2.17	0.178
3.90	0.267	**0.4851**	1.82	0.191	0.423	2.21	0.180
3.95	0.263	0.4849	1.84	0.186	0.419	2.25	0.182
4.00	0.259	0.4831	1.87	0.180	0.416	2.31	0.193

Table 5: Same as Tab. 4 for $j = 0.9$.

	numerical results			perturbation theory			relative difference
σ	$\mathcal{A}^{(2,2,0)}$	$\mathcal{A}^{(2,-2,0)}$	$\frac{\mathcal{A}^{(2,-2,0)}}{\mathcal{A}^{(2,2,0)}}$	$\mathcal{A}^{(2,2,0)}$	$\mathcal{A}^{(2,-2,0)}$	$\frac{\mathcal{A}^{(2,-2,0)}}{\mathcal{A}^{(2,2,0)}}$	$\frac{\mathcal{A}^{(2,-2,0)}}{\mathcal{A}^{(2,2,0)}}$
1.60	0.1594	0.3156	1.98	0.1768	0.3683	2.08	0.05
1.70	0.1615	0.3319	2.06	0.1766	0.3857	2.18	0.06
1.75	0.1621	0.3399	2.10	0.1755	0.3990	2.27	0.08
1.80	0.1625	0.3476	2.14	0.1752	0.4022	2.30	0.07
1.85	**0.1626**	0.3553	2.18	0.1740	0.4101	2.36	0.07
1.90	0.1625	0.3629	2.23	0.1725	0.4177	2.42	0.08
2.00	0.1617	0.3775	2.33	0.1725	0.4323	2.51	0.07
3.60	0.0800	0.5173	6.47	0.0566	0.5259	9.30	0.30
3.70	0.0743	0.5192	6.99	0.0507	0.5235	10.32	0.32
3.75	0.0714	0.5204	7.29	0.0479	0.5220	10.89	0.33
3.80	0.0688	0.5204	7.56	0.0452	0.5203	11.51	0.34
3.85	0.0661	**0.5212**	7.89	0.0427	0.5184	12.15	0.35
3.90	0.0636	0.5208	8.19	0.0402	0.5162	12.85	0.36
4.00	0.0590	0.5194	8.81	0.0355	0.5114	14.41	0.39
4.10	0.0590	0.5184	8.79	0.0312	0.5059	16.20	0.46
4.20	0.0505	0.5144	10.19	0.0274	0.4997	18.25	0.44
4.30	0.0469	0.5098	10.88	0.0239	0.4929	20.64	0.47
4.40	0.0433	0.5047	11.65	0.0207	0.4854	23.41	0.50
4.50	0.0433	0.4991	11.52	0.0179	0.4774	26.63	0.57

[83]. However, if one takes into account the limitations imposed by the *time-shift problem*, the agreement can in fact be considered excellent. For example, take the $j = 0.5, m = -2$ case, which is the one where the difference between the theoretical and numerical values is largest. The theoretical maximum is located at $\sigma = 3.434M$, while the numerical value is $\sigma = (3.875 \pm 0.075)M$ (the uncertainty indicating the difference between consecutive values of σ). The relative numerical amplitude between $\sigma = 3.45M$ and $\sigma = 3.85M - 3.9M$ from the simulations is ≈ 1.008 (see Tab. 4). If the values of t_0 for these two widths differ by $\approx 0.09M$, the amplitude corresponding to $\sigma = 3.45M$ would actually be larger than the one of $\sigma = 3.85M - 3.9M$ and would therefore shift the maximum to the predicted value of $3.45M$. Recalling that $t_0 = 60M$ was used, a very modest uncertainty in the *relative* ringdown starting time ($\approx 0.4\%$) would shift the maximum to the theoretical value. It was also assumed that the excitation time t_0 is the same for all the initial data sets when fitting the numerical data. Whenever such assumption is a good approximation, the precise value of t_0 should not affect the location of the width for which the excitation amplitudes are maximal. In particular, the approximation should be good if the initial data pulses are relatively narrow. However, as σ increases, the possibility of the excitation time t_0 shifting around has to be taken into account, because the interaction time of the pulse with the black hole becomes longer and the interaction sets in well before the center of the pulse reaches the black hole. Taking all this into account, the agreement between numerical and perturbative results *for the location of the maxima* can be considered excellent. The situation for the amplitudes themselves is different, as discussed next.

Tables 4 and 5 show the predicted and extracted absolute and relative amplitudes for the co- and counter-rotating modes $\mathcal{A}^{(m=2)}$, $\mathcal{A}^{(m=-2)}$. As expected, the prediction from perturbation theory works better for sharp pulses. The differences between the predicted and absolute values are of order a few percent for sharp pulses and grow with σ. For $\sigma = 4$ the difference is as large as $\sim 20\%$ and $\sim 60\%$ for $j = 0.5$ and $j = 0.9$, respectively (the actual amplitudes being larger than the predicted ones). These large differences in the

relative amplitudes are mostly due to the amplitude of the corotating mode, the predicted and extracted amplitudes for the counterrotating one agree quite well. The fact that the location of the maxima, as discussed above, agrees very well despite the large differences in the amplitudes for larger σ can be easily explained: the location of the maxima for the corotating mode takes place at $\sigma \approx 1.85M$, which corresponds to a pulse which is sharp enough for perturbation theory to give a good prediction, while the maximum for the counterrotating mode is at a larger value of σ but, as discussed before, the agreement between predicted and measured amplitudes is quite good for that mode.

Could this large difference in amplitudes be explained by the *time-shift problem*, as discussed in Chap. 4.8? Using Eq. (77) and assuming that t_0 is roughly the same for both modes it is found that an uncertainty in the excitation time as large as $\delta_0 = \pm 5M$ would imply an uncertainty on the relative amplitudes of about $\pm 1.1\%$ for $j = 0.5$, and $\pm 13\%$ for $j = 0.9$. Therefore the uncertainty δ_0 does not seem to account for the differences that are found with respect to the predicted amplitudes. One possibility is that the excitation time t_0 is different for the two modes in a pair; but, if so, it is not clear then why the naive choice of t_0 is very good for the counterrotating mode and quite bad for the corotating one. It is actually not clear why such a large disagreement happens only for the corotating mode, and not for the counterrotating one. The possibilities that the initial data and/or the observer are not far enough away for the asymptotic approximation to be valid, or that the disagreement is due to a lack of resolution, seem to be ruled out by one-dimensional studies in the non-spinning case [96]. Summarizing, even though the exact mechanism is not clear, all this suggests that the predicted amplitudes for the corotating mode in the asymptotic approximation are simply valid only for very sharp pulses, as the black hole spin increases.

To conclude this subsection, it is interesting to discuss one aspect of the simulations, as shown in Fig. 21. One can see a rather large discrepancy between the amplitudes resulting from runs with resolution $\Delta r = M/5$ and $\Delta r = M/10$, especially for $j = 0.9$.

That is a direct effect of decreasing accuracy in $\mathcal{I}(\omega^{(\ell,m,n)})$ when going to high spins and the need for more resolution in those cases. The *location* of the maximum, however, is always consistent (that is, within the differences in σ used in the different initial data sets) between runs of different resolution. That is not surprising since the measured $\omega^{(\ell,m,n)}$ at a fixed resolution is roughly the same for all values of σ, and the value of σ that maximizes $\mathcal{A}^{(\ell,m,n)}$ only depends on the value of $\mathcal{R}(\omega^{(\ell,m,n)})$.

4.12 Rapidly Spinning Black Holes and Overtones

As discussed in the introduction to this chapter, a single complex quasinormal frequency contains enough information to determine the two parameters of a Kerr black hole (namely, its mass M and spin j). If one is able to detect a second mode from the same source, one can use this extra information for a consistency check that would increase the confidence in the interpretation of the measured data as signals from a perturbed black hole. An important question that might be answered by numerical relativity is whether more than one mode will be detectable by Earth- and space-based gravitational wave detectors. In Chap. 4.11 the relative amplitude of corotating and counterrotating modes were considered; here the simulations are used to determine the relative excitation of overtones with the same angular dependence and $m > 0$. According to perturbation theory, in this case the damping time of the first overtone becomes comparable to the damping time of the fundamental mode for large spins (see Fig. 16). In addition, the excitation factor of higher overtones is usually larger than the excitation factor of the fundamental mode for large j [83]. This means that higher overtones are more likely to be detectable for fast spinning black holes. A detailed study of this topic is beyond the scope of this chapter and this thesis, but here a brief discussion is presented on how one can extract information about overtones from numerical data and determine which modes contribute most significantly to the waveform.

Simulations for different spins ($j = 0$, 0.5, 0.9, and 0.98) are performed. The initial data and numerical procedure are the same as in Chap. 4.4 and 4.6, with one exception: for

spins $j \geq 0.9$ it was found necessary to increase the angular resolution. The simulations presented here used a resolution of 31×31 grid points on each block in the angular directions. This is not surprising, since for fast rotation one expects more dynamics in the angular directions.

The extraction of modes is done in principle according to Chap. 4.7 and 4.9. Extracting information about all modes present in the data can turn into a subtle problem, especially when the contributions of some modes is weak. One option is to first fit for the strongest mode present in the data, subtract the fit, fit for the next dominant mode and so on, repeating the procedure as long as an oscillatory exponential decay is seen in the data. However, when there are several modes with similar contributions one can just fit for all of them at the same time. This is exactly what has been done for fundamental modes with different m in the previous subsection. When a single mode dominates the waveform the first strategy not only seems to be more meaningful, but also turns out to work better in practice. The results of this chapter were computed by a hybrid of these two methods, depending on the contribution of each mode (something that one can find out by, for example, looking at the dominant frequencies of the signal to fit).

Tab. 6 shows the quasinormal frequencies of the overtones that were obtained from the simulations, using $(A = 0, B = 1)$, $\sigma = M, r_0 = 20M$ and an observer at $r = 60M$. It was found that the overtones for the $m = -2$ mode do not contribute enough to the waveforms to extract them from the data with decent accuracy, especially for high spins. The reason for this is that the imaginary part of their frequency is generally smaller than the one for the corresponding $m = 2$ mode, which makes them decay faster. The decay of the $m = 2$ mode, on the other hand, slows down considerably when increasing the spin. Numerically one can find that the excitation amplitude (at fixed t_0) increases with increasing spin. Those two effects combined make the extraction of overtones easier and more accurate in the high spin cases. Quite remarkably, for runs with spin $j = 0.9$ and

above one can extract the quasinormal frequency for $n = 2$ with reasonable accuracy (see Table 6).

Tab. 7 compares the amplitudes of the three most dominant $l = 2$ modes, $(m = 2, n = 0)$, $(m = -2, n = 0)$ and $(m = 2, n = 1)$, with the predicted asymptotic amplitudes of Eq. (81). Except for the $j = 0.98$ case, the difference between the predicted and extracted values for the relative amplitudes between a given mode and the fundamental $\ell = 2 = m$ one is of the order of a few percent for the fundamental mode and one order of magnitude larger for the first overtone.

Table 6: Comparison of quasinormal frequencies for the first overtones ($n = 1, 2$) of an $\ell = 2$, $m = 2$ mode, for black holes with varying spin, as predicted by perturbation theory and as extracted from the numerical simulations, along with their relative differences. This table is complementary to Tab. 3, where the frequencies associated to the fundamental modes are shown. The extraction of overtones becomes easier for rapidly rotating black holes, as explained in the text, allowing to extract the frequencies of two overtones for high spins.

j	n	$\omega_{\rm perturb}$	$\omega_{\rm numerical}$	rel. difference (Re, Im)
0.0	1	$0.46385 - 0.29560$i	$0.45651 - 0.28859$i	1.58×10^{-2}, 2.37×10^{-2}
0.5	1	$0.57344 - 0.28334$i	$0.54718 - 0.31722$i	4.58×10^{-2}, 1.20×10^{-1}
0.9	1	$0.77768 - 0.20801$i	$0.73737 - 0.19558$i	5.18×10^{-2}, 5.98×10^{-2}
0.9	2	$0.77043 - 0.34720$i	$0.52473 - 0.35319$i	3.19×10^{-1}, 1.73×10^{-2}
0.98	1	$0.89622 - 0.12214$i	$0.93152 - 0.12406$i	3.94×10^{-2}, 1.57×10^{-2}
0.98	2	$0.89358 - 0.20244$i	$0.88668 - 0.25850$i	7.72×10^{-3}, 2.77×10^{-1}

4.13 Summary

The chances of a multi-mode detection by either Earth- or space-based gravitational wave detectors will depend on the relative amplitude of those modes. Knowing in advance which modes should be excited under a realistic binary merger would reduce the dimensionality of the template bank needed to perform matched filtering on ringdown waveforms. An answer that numerical relativity might provide is precisely which modes are likely to be dominant. This involves predicting the relative amplitudes of different pairs of modes

Table 7: Absolute and relative amplitudes as a function of the black hole spin and angular dependence of the perturbations, as predicted by perturbative calculations and as extracted from the numerical evolutions. The amplitudes are given for the wave expressed in Boyer Lindquist coordinates (see appendix B for details) and are multiplied by a factor of r/r_0 to get them in an observer independent form. The last column presents the relative difference between perturbative and numerical results for relative amplitudes. In the corotating case the amplitude of the first overtone are also extracted. The differences in the relative amplitudes are considerably smaller when one looks at corotating and counterrotating modes, compared to the case of fundamental mode and first overtone with the same angular dependence. This can be explained by the relative magnitude of their damping frequencies, as discussed in Chap. 4.8 (see also Tab. 6). This difference becomes less pronounced at very large spins, as expected from the analysis of Chap. 4.8.

	mode			numerical result		perturbation theory		relative difference
j	l	m	n	$\mathcal{A}^{(\ell,m,n)}$	$\frac{\mathcal{A}^{(\ell,m,n)}}{\mathcal{A}^{(2,2,0)}}$	$\mathcal{A}^{(\ell,m,n)}$	$\frac{\mathcal{A}^{(\ell,m,n)}}{\mathcal{A}^{(2,2,0)}}$	$\frac{\mathcal{A}^{(\ell,m,n)}}{\mathcal{A}^{(2,2,0)}}$
0.00	2	2	0	0.211	1.00	0.221	1.00	0.00
0.00	2	2	1	0.316	1.50	0.504	2.28	0.342
0.50	2	2	0	0.201	1.00	0.213	1.00	0.00
0.50	2	-2	0	0.208	1.03	0.228	1.07	0.037
0.50	2	2	1	0.525	2.61	0.768	3.61	0.277
0.90	2	2	0	0.137	1.00	0.148	1.00	0.00
0.90	2	-2	0	0.211	1.54	0.246	1.66	0.072
0.90	2	2	1	0.533	3.89	0.98	6.62	0.412
0.98	2	2	0	0.0833	1.00	0.068	1.00	0.00
0.98	2	-2	0	0.263	3.16	0.257	3.78	0.164
0.98	2	2	1	0.634	7.61	0.416	6.12	0.243

under a variety of scenarios. In this chapter a first step towards understanding the issues involved in such a prediction has been taken.

First a systematic way of extracting QNMs from a given signal has been presented. The procedure has a number of built in self-consistency checks, to make sure that when one keeps adding modes to the fit one is fitting a true signal and not numerical noise. One of these self-consistency checks is to make sure that one extracts the correct quasinormal frequency of each mode within a certain accuracy. If the data being analyzed comes from a numerical simulation, consistent frequencies can be used to monitor the accuracy of the code. If the data is experimental, consistency of the frequencies allows for a test of the no hair conjecture. In more detail: during the fitting procedure one first fits for the dominant mode(s), looks at the residual (defined as the difference between the original signal and the fit), makes sure that it has a consistent quasinormal ringing behavior and only then fits for the next set of modes, repeating the procedure as long as it makes sense to do so. By following this procedure it was hardly possible to go beyond the first few dominant modes, and this was only possible in very special cases. The results seem to indicate that this will likely happen in most numerical simulations

The so-called *time-shift problem* was addressed in some detail. In essence, this is the fact that the quasinormal amplitudes depend exponentially on the quasinormal ringing excitation time, which is not defined unambiguously (not even in the continuum). Furthermore, examining this problem quantitatively using actual values of quasinormal frequencies it was shown that this exponential dependence is an important factor to take into account in practice. To (partially) get rid of this exponential dependence it was proposed to look at relative amplitudes: choosing pairs of modes whose damping frequency is as close as possible, one can partially cancel each others' exponential dependence. The exponential dependence of different pairs of modes as a function of the black hole spin was analyzed in detail. In particular, it was found that the *time-shift problem* becomes more important as one increases the spin. For modes with the same value of ℓ, for example, the

problem is not very relevant for spins $j \lesssim 0.5$. On the other hand, an accurate extraction of the relative amplitude between the fundamental mode and the first overtone only seems feasible for very high spins and $m > 0$.

Keeping this in mind, first the fundamental quasinormal frequencies for different values of spin, ranging from $j = 0$ to a rapidly rotating black hole with $j = 0.98$ were extracted. Even using modest resolutions the frequencies agree with those obtained from perturbation theory within one part in 10^5 to one part in 10^2, depending on the black hole spin, location of the observer and angular dependence. To the authors knowledge this is the first time that quasinormal frequencies for scalar perturbations of Kerr, as predicted by perturbation theory, have been confirmed by numerical evolutions of the field equations.

Next the relative amplitude of corotating and counterrotating fundamental modes was analyzed in detail, as a function of the width of the initial perturbation and the black hole spin, making it possible to quantify (within the limitations imposed by the *time-shift problem*) under what conditions the asymptotic approximation of Ref. [83] is valid. In particular, it was possible to verify the widths of the initial perturbation corresponding to the maximal QNM excitation. Finally, the excitation of overtones was studied. It was found that, according to expectations from perturbation theory [83], they get significantly excited for corotating modes and very high spins. In this particular case it was possible to extract the complex QNM frequency for the fundamental mode and the first two overtones, with a difference with respect to the predicted values by perturbation theory of the order of a tenth of a percent to ten percent, depending on the mode and the black hole spin. The author expects the techniques and results of this chapter to be general enough to be useful for future work on ringdown waveforms.

5 Comparison of Wave Extraction Methods in Non-Linear Black Hole Evolutions

5.1 Introduction

One of a major motivation for numerical relativity is to predict and analyze the gravitational radiation emitted from some physical process. One difficulty is how to separate the radiation content of a numerical space-time from the background geometry. This in fact is a non-trivial problem that can be solved rigorously only for very specific situations. If the computational domain includes null infinity, radiation can be defined and extracted in an unambiguous way (see for example [97] and references therein, and [98]). Due to extra complexity that arises when handling null infinity in numerical simulations, many relativity codes truncate the domain and place an artificial boundary at a finite, hopefully large distance. This implicates that the extraction radius is finite as well and one has to rely not only on the assumption that the observer is far enough in the wave zone to compute reasonably accurate waveforms but also on some approximations in the way gravitational radiation is computed in terms of the space-time metric. In general one expects that for an asymptotically flat space-time the differences between the extracted waves and the correct solution decay as the extraction radius is moved further out. A question that naturally arises is – for a given wave extraction method – at which radius one has to do the extraction so that the errors in the wave form are dominated by numerical discretization error and not by systematic errors originating from the extraction algorithm itself.

The extraction methods that are compared here are based on the theory of perturbed single Schwarzschild black holes. In a linear treatment, the perturbations are well described by the Regge-Wheeler (RW) and Zerilli equations, for odd and even parity waves respectively. These equations are wave equations for a single scalar quantity, namely the Regge-Wheeler function for odd parity perturbations [99] and the Zerilli function for even parity ones [100]. If the mass of the black hole is known, these functions can be extracted

from a numerical space-time and serve as a measure for its radiation content. This method goes back to Abrahams and Evans [101, 102, 103] and has been used extensively in numerical relativity since then (see [104] for early work on that and [105] for a review). For example, the accuracy of simulations of distorted black holes was tested by comparing extracted waveforms against perturbative calculations [106, 107, 108, 109, 110], and often, also technical improvements (such as excision) were tested by studying their effects on waveforms [111, 112]. Recently, [113] reported Zerilli waveforms from unequal mass binary black hole inspirals. In hydrodynamical simulations, gravitational waves are often determined via the quadrupole formula, which usually gives more accurate information in these particular situations (unless a black hole is present), since the wave amplitude is typically very small and thus difficult to detect from the space-time metric [114, 115, 116]. Another popular approach to wave extraction, which will not be discussed here, is based on the Weyl scalar Ψ_4 (see for example [117, 118, 119, 120, 121, 122, 123, 124, 125, 126, 127]).

One simple way to apply the RW formalism is to assume that the background is the Minkowski space-time. This is justified by the fact that the leading order of the metric in an expansion of $1/r$ is flat. To decrease the errors one can incorporate the next order in the expansion, which is described by the Schwarzschild solution. Even higher orders can be taken into account to incorporate for example the spin contribution. It is obvious that all these methods will give the same result at an infinite radius.

A property of the standard RW approach is that it is gauge invariant only with respect to infinitesimal first order changes of coordinates, which keep the background coordinates fixed. In other words, the background metric has to represent the geometry of the Schwarzschild space-time, and the metric components have to be expressed in the Schwarzschild coordinate base. This is not necessarily the case in numerical simulations. Even if the background metric is close to the Schwarzschild geometry, it does not need to be close to Schwarzschild in Schwarzschild coordinates. An example are simulations that

use coordinates – contrary to the Schwarzschild ones – that are regular at the horizon. This is typically done in combination with excision.

Here also a generalized RW wave extraction method is implemented that is fully covariant in the sense that it is independent of the coordinates of the Schwarzschild background, assuming those coordinates are aligned with the spherical symmetry of the background. In other words, it is assumed that there is no angular shift. Therefore the generalized RW wave extraction can give correct waveforms for perturbations of Schwarzschild black holes independent of the slicing. It is based on ideas formulated in [128, 129, 130].

It could be argued that the improvement from this method is marginal, since it is only a higher order correction in powers of $1/r$ compared to the order to which the extraction method is valid anyway. One reason why the author still believes that this method is useful is that for example in binary black hole simulations the space-time decays to that of a stationary black hole but in generally unknown coordinates.

The wave extraction methods are compared in a very particular scenario, that the author believes has relevance for more general cases, namely perturbations of a Schwarzschild black hole. Here the focus is on the odd parity sector. A similar study for even parity perturbations is currently being worked on. It is especially interesting to investigate the dependence of the errors on the observer location for extraction radii that are chosen in a range that is commonly used for example in state or the art binary black hole simulations. Due to the efficiency of multi-block methods it is easily possible to choose domains with outer boundaries located at several hundred or even up to 1000M (such simulations are shown in [26], using very similar methods to the ones presented here) at relatively small computational cost. For example in the simulations shown later in this chapter, boundaries were placed at $250M$, far enough that the waveforms extracted at radii up to $80M$ (which is larger than used with most current evolution codes) were uncontaminated by reflections from the boundaries for more than $250M$ of evolution time.

The initial data are constructed in a way that they satisfy the linearized constraints. The evolutions are done with a first order generalized harmonic formulation of the Einstein equations. Wave extraction is greatly simplified by the use of a six-block grid structure with cubed-sphere coordinates (see Chap. 2.2.4), which allows integrations over coordinate spheres without the need for interpolation.

It is found that for the standard RW approach even at the largest extraction radius that was used ($r = 80M$), the errors are dominated by systematic errors in the extraction and not by numerical truncation error. Also analyzed are the quasinormal frequencies of the waves, using the methods described in Chap. 4 and compared against the results known from perturbation theory and excellent agreement was found in all cases. Additional details can be found in [131].

5.2 Generalized Harmonic System

The actual system of equations that is used for the simulations is the so called generalized harmonic system.

The name harmonic system comes from a special choice of coordinates, the so called harmonic coordinates, that have the property that they satisfy the harmonic wave equation. Besides their use in a variety of disciplines within general relativity they have been used to find numerical solutions to the Einstein equations, for example fairly recently by Garfinkle [132] and by Winicour et al. [133, 134, 135]. A generalization of the harmonic system that allows for arbitrary coordinate systems was described by Friedrich [136]. The attractiveness of using harmonic coordinates comes from their property of bringing the Einstein equations into a manifestly hyperbolic form. The principal part of the evolution equations of the four metric is identical to the second order wave equation.

As one of the first persons Pretorius in 2005 presented seminal evolutions that follow a binary black hole system through the last few orbits, the plunge and the final merger [137], using a harmonic formulation with built in constraint damping that was described

by Gundlach [138]. This constraint damping mechanism is based on the lambda proposal by Brodbeck, Hübner, Frittelli and Reula [139].

Here a first order symmetric hyperbolic implementation of the generalized harmonic system is used. It is described in detail by Lindblom et.al. in [140] and was, combined with pseudo spectral methods, successfully used for binary black hole simulations by Scheel et.al.[39]. The option to control the evolution of the constraints is built into this formulation and this seems to be a crucial feature for long term stable evolutions. In outlining the properties of this system the description given in [140] is followed closely.

5.2.1 Harmonic Coordinates

Coordinates x^μ are called harmonic if they satisfy the standard harmonic wave equation

$$-\Gamma_\mu \equiv g_{\mu\nu}\nabla^\rho\nabla_\rho x^\nu = 0. \tag{83}$$

Here ∇_μ is the covariant derivative and $\Gamma_\mu = g^{\nu\rho}\Gamma_{\mu\nu\rho}$ with $\Gamma_{\mu\nu\rho}$ being the standard Christoffel symbol. If the Ricci tensor $R_{\mu\nu}$ is computed using these definitions, all terms, except the ones containing second derivatives vanish and the vacuum Einstein equations $R_{\mu\nu} = 0$ become manifestly hyperbolic. Explicitly they are given as

$$g^{\rho\sigma}\partial_\rho\partial_\sigma g_{\mu\nu} = 2g^{\rho\sigma}g^{\tau\eta}\left(\partial_\tau g_{\rho\mu}\partial_\eta g_{\sigma\nu} - \Gamma_{\mu\rho\tau}\Gamma_{\nu\sigma\eta}\right). \tag{84}$$

5.2.2 Gauge Sources

Friedrich [136] (Garfinkel applied this to cosmology simulations [132]) worked out a variation of the harmonic system that allows for arbitrary coordinates while preserving the hyperbolic form of the Einstein equations. The coordinates have to satisfy the following inhomogeneous wave equation:

$$-\Gamma_\mu \equiv g_{\mu\nu}\nabla^\rho\nabla_\rho x^\nu = H_\mu(x, g) \tag{85}$$

H_μ is an arbitrary function of the coordinates and the metric but is not allowed to contain first or higher derivatives of either. Using that condition with the Ricci tensor one obtains the Einstein equations in the form

$$g^{\rho\sigma}\partial_\rho\partial_\sigma g_{\mu\nu} = 2g^{\rho\sigma}g^{\tau\eta}\left(\partial_\tau g_{\rho\mu}\partial_\eta g_{\sigma\nu} - \Gamma_{\mu\rho\tau}\Gamma_{\nu\sigma\eta}\right) - 2\nabla_{(\mu}H_{\nu)}. \tag{86}$$

The extra terms including H_ν are given algebraic functions that do not contain derivatives and therefore to not change the principal part of the equations. Therefore the hyperbolic structure of the evolution equations is untouched by specifying the coordinates in this way.

5.2.3 Relation Between Standard 3+1 Quantities and Evolution Variables of the Generalized Harmonic System

Traditionally the standard 3+1 ADM quantities g_{ij} and K_{ij} together with the gauge quantities, the lapse α and the shift vector β^i have been used frequently in numerical relativity. See App. C for details. It is therefore instructive to establish the relation between these quantities and the variables of the generalized harmonic system. As described in App. C, in the frame work of the 3+1 formalism the four dimensional space-time is foliated by $t =$ constant three dimensional space-like hypersurfaces with associated coordinates x^i, $i = 1, 2, 3$. The general four metric can be written in terms of the three metric γ_{ij} on each slice, the lapse and the shift as (see also App. C)

$$ds^2 = -\alpha^2 dt^2 + \gamma_{ij}\left(dx^i + \beta^i dt\right)\left(dx^j + \beta^j dt\right). \tag{87}$$

The extrinsic curvature is defined as

$$K_{ij} = -\frac{1}{2}\mathcal{L}_{\bar{n}}\gamma_{ij} \tag{88}$$

where $\bar{n}$ is the time-like unit vector normal to the three dimensional hyper surface. The three metric γ_{ij} simply is the spatial part of the four metric $g_{\mu\nu}$ used in Eq. (86).

The relation between the gauge quantities α, β^i and H_μ unfortunately are not as straight forward. To obtain them one has to use the metric of the form given in Eq. (87) with the generalized harmonic coordinate condition $H_\mu = \Gamma_\mu$ to arrive at the equalities

$$\partial_t \alpha - \beta^k \partial_k \alpha = -\alpha \left(H_t - \beta^i H_i + \alpha K \right) \tag{89}$$

$$\partial_t \beta^i - \beta^k \partial_k \beta^i = \alpha \gamma^{ij} \left[\alpha \left(H_j + \gamma^{kl} \Gamma_{jkl} \right) - \partial_j \alpha \right]. \tag{90}$$

Note that the index t in H_t labels the zeroth component of the four dimensional object H. $K = \gamma^{ij} K_{ij}$ is the trace of the extrinsic curvature. From Eq. (89)-(90) it is clear that instead of determining α and β^i directly H_μ acts as a source term in a set of partial differential equations that govern the evolution of these quantities. Due to the absence of derivatives in H_μ the principal part and therefore the hyperbolic structure of these evolution equations is unchanged when choosing a different H_μ. Since H_μ can be an arbitrary time dependent function, it is clear that by choosing it accordingly any behavior of the lapse and the shift can be enforced. This illustrates the statement made earlier that arbitrary coordinate systems can be represented by the generalized harmonic coordinates.

5.2.4 Constraint Evolution System

General relativity is a theory with constraints. In numerical work, the constraints serve as an error measure, even though – besides the requirement that they converge to zero with increasing resolution – there is no general criterion for how much constraint violation is acceptable for a given physics problem. It is understood though that *large constraints* mean *large errors* and that for example exponentially growing constraints indicate a numerical solution that is drifting away from solutions to the Einstein equations and therefore is becoming unphysical quickly. This behavior has been observed in numerical relativity for a long time.

It is now described how to analyze the evolution of the constraints off the constraint surface and to modify the main evolution system in a way that it is void of growing constraint modes. The propagation of the constraints as a non-linear system was presented by Friedrich in 2005 [141].

In the generalized harmonic system, the condition that the coordinates satisfy the inhomogeneous wave equation serves as a set of four constraints

$$\mathcal{C}_\mu = H_\mu + \Gamma_\mu. \tag{91}$$

For the following discussion the evolution Eq. (86) are modified by adding derivatives of the constraints.

$$R_{\mu\nu} - \nabla_{(\mu}\mathcal{C}_{\nu)} = 0 \tag{92}$$

To derive the evolution equations for the constraints, one first takes the trace of Eq. (92) and subtract it from Eq. (92) to arrive at

$$R_{\mu\nu} - \tfrac{1}{2}g_{\mu\nu}R - \nabla_{(\mu}\mathcal{C}_{\nu)} + \tfrac{1}{2}g_{\mu\nu}g^{\eta\rho}\nabla_{(\eta}\mathcal{C}_{\rho)} = 0 \tag{93}$$

$$\Rightarrow \quad -\tfrac{1}{2}\nabla^\nu\nabla_\mu\mathcal{C}_\nu + \tfrac{1}{2}\nabla_\mu\nabla^\nu\mathcal{C}_\nu - \tfrac{1}{2}\nabla^\nu\nabla_\nu\mathcal{C}_\mu = 0. \tag{94}$$

To get to the second line, the contracted Bianchi identities $\nabla^\nu R_{\mu\nu} = \frac{1}{2}\nabla_\mu R$ are used. The definition of the Riemann tensor is applied $\nabla_{[\mu}\nabla_{\nu]}C^\eta = R^\eta{}_{\tau\mu\nu}C^\tau$ (assuming a torsion free metric) to replace the first two terms in Eq. (94) and arrive at

$$R_{\mu\nu}\mathcal{C}^\nu + \nabla^\nu\nabla_\nu\mathcal{C}_\mu = 0. \tag{95}$$

Finally by plugging Eq. (92) into Eq. (95) one gets

$$\nabla^\nu\nabla_\nu\mathcal{C}_\mu + \mathcal{C}^\nu\nabla_{(\mu}\mathcal{C}_{\nu)} = 0. \tag{96}$$

From that equation it is obvious that the constraints will stay zero for all times if they are satisfied on any space-like hypersurface and if on that hypersurface $\partial_t \mathcal{C}_\mu = 0$. Therefore the generalized harmonic system is consistent. That is of course only true in the absence of boundaries. If boundaries are present, constraint-preserving boundary conditions have to be applied to keep the system consistent on the continuum level [142, 143, 144, 145, 146]. In numerical simulations, due to truncation error, the discrete constraints get excited and tend to grow in time at a fixed resolution. In the following chapters it is discussed how to modify the equations to prevent such a growth.

5.2.5 Relation Between the Generalized Harmonic Constraints and the Standard Hamiltonian and Momentum Constraints

Again one wants to see the relation between the widely used ADM quantities and the generalized harmonic ones. The goal is to express the Hamiltonian $\mathcal{H}$ and the momentum $\mathcal{M}^i$ constraints (defined in App. C) in terms of the constraints $\mathcal{C}_\mu$ that show up in the generalized harmonic system and are defined by Eq. (91).

It is convenient to introduce a four dimensional momentum constraint

$$\mathcal{M}_\mu \equiv \left(R_{\mu\nu} - \frac{1}{2} g_{\mu\nu} R \right) \bar{n}^\nu \tag{97}$$

where again $\bar{n}^\mu$ is the unit time-like normal vector to the t = constant hypersurface. This new object has the standard Hamiltonian constraint as its zeroth component and the standard three dimensional momentum constraints as its second, third and fourth component. By using the definition in Eq. (92) one finds

$$\bar{n}^\nu \nabla_\nu \mathcal{C}_\mu = 2\mathcal{M}_\mu + \left((g^{\nu\eta} + \bar{n}^\nu \bar{n}^\eta) \bar{n}_\mu - (g^\nu{}_\mu + \bar{n}^\nu \bar{n}_\mu) \bar{n}^\eta \right) \nabla_\nu \mathcal{C}_\eta. \tag{98}$$

5.2.6 Modified Generalized Harmonic System with Constraint Damping

Until now a manifestly hyperbolic formulation of the Einstein equations has been established, with complete freedom of coordinate choice, as long as they are written in the

generalized harmonic form. The constraints were defined and their evolution equations computed, which revealed that the formulation is consistent. It was also shown how the generalized harmonic variables, especially the gauge functions and the constraints are related to the more widely used 3+1 formalism. Following [138], a further adjustment is added to the formulation of Einsteins equations in generalized harmonic coordinates (Eq. (92)):

$$R_{\mu\nu} - \nabla_{(\mu}\mathcal{C}_{\nu)} + \zeta_0 \left[\bar{n}_{(\mu}\mathcal{C}_{\nu)} - \frac{1}{2} g_{\mu\nu}\bar{n}^{\sigma}\mathcal{C}_{\sigma}\right] = 0. \tag{99}$$

ζ_0 is a free parameter. The principal part of these equations is identical to the formulations (92) and (86) so one knows that the system of equations is still symmetric hyperbolic.

The constraint evolution equations are derived following the recipe given in Chap. 5.2.4. Like for the evolution equations, the principal part of the constraint evolution system is unchanged compared to the unmodified generalized harmonic system. The explicit form of the equations is

$$\nabla^{\nu}\nabla_{\nu}\mathcal{C}_{\mu} + \mathcal{C}^{\nu}\nabla_{(\mu}\mathcal{C}_{\nu)} - 2\zeta_0\nabla^{\nu}\left[\bar{n}_{(\nu}\mathcal{C}_{\mu)}\right] - \frac{1}{2}\zeta_0\bar{n}_{\mu}\mathcal{C}^{\nu}\mathcal{C}_{\nu} = 0. \tag{100}$$

Also the relation to the four dimensional momentum constraint $\mathcal{M}^{\mu}$ stays the same in the sense that on a t = constant hyper surface setting $\mathcal{C}_{\mu} = \partial_t\mathcal{C}_{\mu} = 0$ is equivalent to $\mathcal{C}_{\mu} = \mathcal{M}_{\mu} = 0$.

A linearized analysis of that constraint propagation system has been executed by Gundlach et.al. [138]. Since one is interested in how the constraints behave close to zero, i.e. what happens in case of an initially small constraint violation, introduced for example by numerical truncation error, the terms quadratic in $\mathcal{C}_{\mu}$ or it's derivative can be ignored. Gundlach found that short wavelength solutions to this linearized problem are damped like $e^{-\zeta_0 t}$ or $e^{-\zeta_0 t/2}$. Choosing a positive ζ_0 in Eq. (99) guarantees small constraint violations to decay in time and therefore the numerical solution to be physical,

in the sense that it satisfies the constraints. A similar analysis for the long wave length solutions is not available at this moment.

5.2.7 First Order Generalized Harmonic System

The numerical methods described in this thesis demand that the partial differential equations that are solved are first order in time and spatial derivatives. To rewrite a second order system into a first order one (for which stability and hyperbolicity is well understood) is straightforward.

To rewrite Eq. (99) in first order form, new variables that replace all second derivatives are introduced.

$$\Psi_{i\mu\nu} \equiv \partial_i g_{\mu\nu} \tag{101}$$

$$\Pi_{\mu\nu} \equiv -\bar{n}^\sigma \partial_\sigma g_{\mu\nu} \tag{102}$$

These definitions give rise to 40 new constraints

$$\mathcal{C}_{i\mu\nu} \equiv \Psi_{i\mu\nu} - \partial_i g_{\mu\nu} \tag{103}$$

$$\mathcal{C}_{\mu\nu} \equiv \Pi_{\mu\nu} + \bar{n}^\sigma \partial_\sigma g_{\mu\nu} \tag{104}$$

Using these definitions with Eq. (99), one gets a set of 50 coupled equations. For the following analysis of these equations it is sufficient to look at their principal part which is

$$\partial_t g_{\mu\nu} \doteq \beta^i \partial_i g_{\mu\nu} \tag{105}$$

$$\partial_t \Pi_{\mu\nu} \doteq \beta^i \partial_i \Pi_{\mu\nu} - \alpha\gamma^{ij} \partial_i \Psi_{j\mu\nu} \tag{106}$$

$$\partial_t \Psi_{i\mu\nu} \doteq \beta^j \partial_j \Psi_{i\mu\nu} - \alpha \partial_i \Pi_{\mu\nu}. \tag{107}$$

While this system is known to be symmetric hyperbolic, it shows two fundamental problems. The additional constraint $\mathcal{C}_{i\mu\nu}$ is not damped and can generally show exponential

growth. Also mathematically the formation of shocks in the gauge variables cannot be ruled out. For example writing the principal part for g_{ti} in terms of the 3+1 quantities on gets terms like $\partial_t \beta^i - \beta^j \partial_j \beta^i = 0$, one of the most basic examples for a differential equation that forms shocks in the solution.

A solution to these issues is to add multiples of the constraints to the right hand sides of the evolution equations in a proper way. Following Lindblom et al [140], one adds $\zeta_1 \beta^i \mathcal{C}_{i\mu\nu}$ to Eq. (105), $\zeta_2 \alpha \mathcal{C}_{i\mu\nu}$ to Eq. (107) and $\zeta_3 \beta^i \mathcal{C}_{i\mu\nu}$ to Eq. (106). ζ_1, ζ_2 and ζ_3 are free parameters. This choice of modifications changes the principal part of Eq. (105)–(107) to

$$\partial_t g_{\mu\nu} = (1+\zeta_1)\beta^i \partial_i g_{\mu\nu} \tag{108}$$

$$\partial_t \Pi_{\mu\nu} = \beta^i \partial_i \Pi_{\mu\nu} - \alpha \gamma^{ij} \partial_i \Psi_{j\mu\nu} + \zeta_3 \beta^i \partial_i g_{\mu\nu} \tag{109}$$

$$\partial_t \Psi_{i\mu\nu} = \beta^j \partial_j \Psi_{i\mu\nu} - \alpha \partial_i \Pi_{\mu\nu} + \zeta_2 \alpha \partial_i g_{\mu\nu}. \tag{110}$$

The full system of equations, containing all non-linear terms is

$$\partial_t g_{\mu\nu} = (1+\zeta_1)\beta^i \partial_i g_{\mu\nu} - \alpha \Pi_{\mu\nu} - \zeta_1 \beta^i \Psi_{i\mu\nu} \tag{111}$$

$$\begin{aligned} \partial_t \Pi_{\mu\nu} = {} & \beta^i \partial_i \Pi_{\mu\nu} - \alpha \gamma^{ij} \partial_i \Psi_{j\mu\nu} + \zeta_3 \beta^i \partial_i g_{\mu\nu} \\ & + 2\alpha g^{\sigma\tau} \left(\gamma^{ij} \Psi_{i\sigma\mu} \Psi_{j\tau\nu} - \Pi_{\sigma\mu} \Pi_{\tau\nu} - g^{\eta\rho} \Gamma_{\mu\sigma\eta} \Gamma_{\nu\tau\rho} \right) \\ & - 2\alpha \nabla_{(\mu} H_{\nu)} - \frac{1}{2} \alpha \bar{n}^\sigma \bar{n}^\tau \Pi_{\sigma\tau} \Pi_{\mu\nu} - \alpha \bar{n}^\sigma \Pi_{\sigma i} \gamma^{ij} \Psi_{j\mu\nu} \\ & + \alpha \zeta_0 \left[2\delta^\sigma_{(\mu} \bar{n}_{\nu)} - g_{\mu\nu} \bar{n}^\sigma \right] (H_\sigma + \Gamma_\sigma) - \zeta_1 \zeta_2 \beta^i \Psi_{i\mu\nu} \end{aligned} \tag{112}$$

$$\begin{aligned} \partial_t \Psi_{i\mu\nu} = {} & \beta^j \partial_j \Psi_{i\mu\nu} - \alpha \partial_i \Pi_{\mu\nu} + \zeta_2 \alpha \partial_i g_{\mu\nu} + \frac{1}{2} \alpha \bar{n}^\sigma \bar{n}^\rho \Psi_{i\sigma\rho} \Pi_{\mu\nu} \\ & + \alpha \gamma^{jk} \bar{n}^\sigma \Psi_{ij\sigma} \Psi_{k\mu\nu} - \alpha \zeta_2 \Psi_{i\mu\nu}. \end{aligned} \tag{113}$$

One can project these equations to an unit vector n_i normal to the space-like boundary and write the resulting principal part symbolically as

$$\partial_t u^\alpha = A^{n\alpha}{}_\beta \partial_n u^\beta \tag{114}$$

where the notation $\partial_n \equiv n^i \partial_i$ and $A^{n\alpha}{}_\beta \equiv A^{i\alpha}{}_\beta n_i$ is used. The eigenvalues of $A^{n\alpha}{}_\beta$ are

$$\begin{aligned} v^1 &= \beta^n - \alpha & (115)\\ v^2 &= \beta^n + \alpha & (116)\\ v^3 = v^4 &= \beta^n & (117)\\ v^5 &= \beta^n(1+\zeta_1). & (118) \end{aligned}$$

The eigenvalues are real, thus the system of equations is hyperbolic. Symmetric hyperbolicity requires the existence of a hermitian symmetrizer $H_{\alpha\beta}$. This symmetrizer can in fact be found and can be written as

$$\mathbf{H} = \begin{pmatrix} \Lambda^2 & -\zeta_2 & 0 & 0 & 0 \\ -\zeta_2 & 1 & 0 & 0 & 0 \\ 0 & 0 & \gamma^{11} & \gamma^{12} & \gamma^{13} \\ 0 & 0 & \gamma^{12} & \gamma^{22} & \gamma^{23} \\ 0 & 0 & \gamma^{13} & \gamma^{23} & \gamma^{33} \end{pmatrix} \tag{119}$$

where γ^{ij} label the components of the inverse spatial metric. The matrix resulting from the product **HA** is symmetric only with the choice of $\zeta_3 = \zeta_1\zeta_2$ and therefore, for this choice of parameters, the first order generalized harmonic system is symmetric hyperbolic.

The characteristic fields are given by

$$\hat{u}^1_{\mu\nu} = g_{\mu\nu} \tag{120}$$

$$\hat{u}^2_{i\mu\nu} = -n^j \Psi_{j\mu\nu} n_i + \Psi_{i\mu\nu} \quad (121)$$

$$\hat{u}^3_{\mu\nu} = -\zeta_2 g_{\mu\nu} + \Pi_{\mu\nu} + n^j \Psi_{j\mu\nu} \quad (122)$$

$$\hat{u}^3_{\mu\nu} = \zeta_2 g_{\mu\nu} - \Pi_{\mu\nu} + n^j \Psi_{j\mu\nu}. \quad (123)$$

5.3 The Background Metric and Tensor Spherical Decomposition of the Perturbations

This and the following chapters summarize the results of the generalized Regge-Wheeler formalism relevant for this part of the thesis. It follows closely the notation and presentation of ref. [128].

This formalism assumes that the total metric can be written as

$$g^{\rm tot}_{\mu\nu} = g_{\mu\nu} + \delta g_{\mu\nu} \quad (124)$$

where $g_{\mu\nu}$ describes the Schwarzschild geometry and $\delta g_{\mu\nu}$ is, in some sense, a "small" correction. Further, it is assumed that the four-dimensional manifold can be decomposed as the product of a two-dimensional manifold $\mathcal{M}$ parametrized with coordinates x^a ($a = 0, 1$) and a unit 2-sphere S^2 with coordinates x^A ($A = 2, 3$), such that the background Schwarzschild metric takes the form

$$ds^2 = \tilde{g}_{ab}(t, r)\, dx^a dx^b + f^2(t, r)\, \hat{g}_{AB}\, dx^A dx^B\,. \quad (125)$$

Capital Latin indices refer to angular coordinates (θ, ϕ) on S^2, while lower-case ones refer to the (t, r) coordinates. Here $\hat{g}_{AB}$ is the standard metric on the unit sphere, $\tilde{g}_{ab}$ denotes the metric tensor on the manifold $\mathcal{M}$, and f^2 is a positive function. If one uses an areal radius coordinate, then $f = r$, but such an assumption is not made here. Actually, as discussed below, the fact that the formalism is general enough to allow for $f = f(t, r)$ has practical advantages in the wave extraction procedure. For simplicity, the metric on

the unit 2-sphere S^2 is assumed to be in standard coordinates: $\hat{g}_{AB} = \mathrm{diag}(1, \sin^2\theta)$. Summarizing, the assumption is made that the background Schwarzschild metric is given in a coordinate system in which there is no angular shift, but there can be a radial shift. Note that there is no assumption about the shift in the perturbation.

From a numerical relativity point of view, it is usually convenient to deal with the variables that appear in the $3+1$ split of space-time. To this end, the notation of ref. [128] is followed and the components of the background Schwarzschild metric explicitly expanded as

$$\begin{aligned} ds^2 &= (-\alpha^2 + \gamma^2\beta^2)dt^2 + 2\gamma^2\beta dt\, dr + \gamma^2\, dr^2 \\ &\quad + f^2(d\theta^2 + \sin^2\theta\, d\phi^2) \end{aligned} \tag{126}$$

where α and $\beta \equiv \beta^r$ are the background lapse and radial shift vector, respectively, and $\gamma^2 \equiv \tilde{g}_{rr}$. Since the background is spherically symmetric, it is convenient to expand the perturbations in spherical harmonics,

$$\delta g_{\mu\nu} = \sum_{\ell=1}^{\infty} \sum_{m=-\ell}^{\ell} \delta g_{\mu\nu}^{(\ell,m)}\,. \tag{127}$$

In the odd-parity sector there is no perturbation for $\ell = 0$. The dipole term, $\ell = 1$, corresponds to the linearization of the Kerr metric using the angular momentum of the space-time as a parameter. Thus, for gravitational wave extraction one only needs to consider perturbations with $\ell \geq 2$. These quantities can be parametrized according to

$$\begin{aligned} \delta\beta_A^{(\ell,m)} &= b^{(\ell,m)} S_A^{(\ell,m)} \\ \delta g_{rA}^{(\ell,m)} &= h_1^{(\ell,m)} S_A^{(\ell,m)} \\ \delta g_{AB}^{(\ell,m)} &= h_2^{(\ell,m)} S_{AB}^{(\ell,m)} \\ \delta K_{rA}^{(\ell,m)} &= \pi_1^{(\ell,m)} S_A^{(\ell,m)} \end{aligned} \tag{128}$$

$$\delta K_{AB}^{(\ell,m)} \quad = \quad \pi_2^{(\ell,m)} S_{AB}^{(\ell,m)} \,.$$

Using the covariant derivative $\hat{\nabla}_A$ compatible with the metric $\hat{g}_{AB}$ on the unit sphere S^2 and its associated Levi–Civita tensor $\hat{\epsilon}_{AB}$ (with non-vanishing components $\hat{\epsilon}_{\theta\phi} = \sin\theta = -\hat{\epsilon}_{\phi\theta}$), the definition $S_A = \hat{\epsilon}^B{}_A \hat{\nabla}_B Y$ (the first index in $\hat{\epsilon}$ raised with the inverse of $\hat{g}$) and $S_{AB} = \hat{\nabla}_{(A} S_{B)}$ is applied. Here, $Y \equiv Y^{(\ell,m)}$ are the standard spherical harmonics. The quantities S_A and S_{AB} form a basis on S^2 for odd-parity vector and symmetric tensor fields, respectively. For completeness, a detailed and self-consistent description of how to use these to decompose vectors and tensors into spherical harmonics is given in App. D.

From now on, the super-indices (ℓ, m) and the sum over them are suppressed, since modes belonging to different pairs of (ℓ, m) decouple from each other in the perturbation formalism.

5.4 Extraction of the Regge-Wheeler Function from a Given Geometry

To define the background metric, the $\ell = 0$ component (that is, the spherically symmetric part) of the numerical solution $g_{\mu\nu}^{\rm tot}$ is extracted. This is done by decomposing the metric $\tilde{g}_{ab}$ of the two-dimensional manifold $\mathcal{M}$ into spherical harmonics. These metric components behave like scalars under a rotation of coordinates. Thus, the background metric is computed as

$$\tilde{g}_{ab} = \frac{1}{4\pi} \int g_{ab}^{\rm tot} d\Omega \,, \tag{129}$$

where $d\Omega$ is the standard area element on S^2. The function f can be computed through $f = \sqrt{A/4\pi}$, with

$$A = \int \sqrt{\hat{g}}\, d\theta\, d\phi \,, \tag{130}$$

where the integration is performed over the extraction 2-sphere, and $\hat{g}$ is the determinant of $\hat{g}_{AB}$.

Similarly, the perturbed quantities are computed by extracting the $\ell \geq 2$ components of the numerical metric $g^{\rm tot}_{\mu\nu}$, in the way explained in App. D.

Once one has obtained the multipoles $b, h_1, h_2, \pi_1, \pi_2$ defined above in Eq. (128) and the background quantities f, α, γ, β defined in eq. (126), one can find the generalized gauge-invariant Regge–Wheeler (RW) function Φ_{RW}. It is given by [128]

$$\Phi_{RW} = \frac{2f}{\lambda\alpha\gamma}\left(\alpha\,\pi_1 - \frac{\partial_0 f}{f} h_1\right). \tag{131}$$

where $\partial_0 \equiv \partial_t - \beta\partial_r$ and $\lambda = (\ell-1)(\ell+2)$. Notice from eq. (131) that the *only* multipole components appearing in the RW function Φ_{RW} are h_1 and π_1, so that there is no need to compute the others.

Previous approaches to compute waveforms with the standard RWZ formalism have typically been considerably more involved than what has just been described. The standard approach is sketched briefly here. Einstein's equations are usually solved using Cartesian coordinates on a Cartesian grid. The numerically obtained metric is first transformed to polar-spherical coordinates. Performing the multipole decomposition on a given coordinate sphere requires a numerical integration over that sphere, which in turn requires interpolating the metric to the spherical surface, which does not coincide with the grid points of the Cartesian grid. Integrating over the sphere also allows computing the areal radius and its radial derivatives. These quantities are then used to transform the metric in a second step to its final form in "Schwarzschild-like" coordinates. This is done by first changing from the coordinate radius to an areal radius (which requires the numerically calculated radial derivatives), and then identifying the (t, r) components of the metric in this new coordinate system, which is assumed to be a perturbation of the Schwarzschild metric in Schwarzschild coordinates. With all this in place, the waveforms are then computed using standard RWZ formulae.

In the case here, the multi-block grid structure naturally allows for spherical surfaces. Hence, no interpolation is required. The generalized perturbation formalism allows to compute the RW function Φ_{RW} without transforming the metric to Schwarzschild coordinates. In particular, the transformation to an areal radial coordinate is not required at all. Thus, the extraction procedure amounts simply to numerical integrations at a given value of the radial coordinate to compute the multipoles, and then using eq. (131) to compute the RW function. An additional improvement is that the high order accurate derivative operators are naturally associated with a high order accurate discrete norm, leading to an integration procedure which has the same accuracy as the derivative operators.

5.5 Construction of Initial Data for Perturbed Black Holes

Initial data representing a single black hole with an arbitrary perturbation added to it are constructed. In this chapter it is described how to set up these initial data on a spherically symmetric background in a way that they satisfy the linearized constraints. This discussion follows closely the description given in [128].

If a function $\Phi(r,t)$ satisfies the generalized Regge-Wheeler equation

$$\ddot{\Phi} = c_1\dot{\Phi}' + c_2\Phi'' + c_3\dot{\Phi} + c_4\Phi' - \alpha^2 V\Phi \tag{132}$$

one can find the corresponding four metric that will satisfy the the linearized Einstein equations from this so called Regge-Wheeler potential Φ. The expression above is valid for spherically symmetric backgrounds and the prime denotes partial derivatives in the radial direction. The coefficients c_i are

$$\begin{aligned} c_1 &= 2\beta \\ c_2 &= \frac{\alpha^2 - \gamma^2\beta^2}{\gamma^2} \\ c_3 &= \frac{\gamma\dot{\alpha} - \gamma\beta\alpha' + \alpha\beta\gamma' - \alpha\dot{\gamma} + \gamma\alpha\beta'}{\gamma\alpha} \end{aligned}$$

$$c_4 = \frac{1}{\gamma^3\alpha}\left(-\gamma^3\beta\dot{\alpha} - \alpha^3\gamma' + \gamma^3\beta^2\alpha' - 2\gamma^3\alpha\beta\beta' + \gamma^3\alpha\dot{\beta} + \gamma^2\alpha\beta\dot{\gamma} + \gamma\alpha^2\alpha' - \gamma^2\alpha\beta^2\gamma'\right).$$

If the background is Schwarzschild in Schwarzschild coordinates, the generalized RW equation reduces to the standard one. The corresponding potential depends on the multipolar mode of the perturbation as well as on the coordinate choice of the background. For Kerr-Schild coordinates it is

$$V_{RW} = \frac{1}{f^2}\left[\ell(\ell+1) - \frac{6M}{f}\right]. \tag{133}$$

For $\ell \geq 2$ the metric perturbations expressed in terms of the Regge-Wheeler function are

$$\delta g_{r\theta} = \left[\frac{\gamma}{\alpha}\left(-f\dot{\Phi} + \beta f\Phi' + \Phi(\beta f' - \dot{f})\right) + \frac{fk' - 2kf'}{f}\right]\frac{Y_\phi}{\sin\theta}$$

$$\delta g_{r\phi} = -\left[\frac{\gamma}{\alpha}\left(-f\dot{\Phi} + \beta f\Phi' + \Phi(\beta f' - \dot{f})\right) + \frac{fk' - 2kf'}{f}\right]\sin\theta Y_\theta$$

$$\delta g_{\theta\theta} = \frac{2k}{\sin^2\theta}\left[-\cos\theta Y_\phi + \sin\theta Y_{\theta\phi}\right]$$

$$\delta g_{\theta\phi} = k\left[\cos\theta Y_\theta + \sin^{-1}\theta Y_{\phi\phi} - \sin\theta Y_{\theta\theta}\right]$$

$$\delta g_{\theta t} = \left[\frac{1}{\gamma\alpha}\left(-\gamma^2\beta f\dot{\Phi} + f(\gamma^2\beta^2 - \alpha^2)\Phi' + (-\alpha^2 f' - \dot{f}\beta\gamma^2 + f'\gamma^2\beta^2)\Phi\right) + \frac{f\dot{k} - 2k\dot{f}}{f}\right]\frac{Y_\phi}{\sin\theta}$$

$$\delta g_{\phi\phi} = 2k\left[\cos\theta Y_\phi - \sin\theta Y_{\theta\phi}\right]$$

$$\delta g_{\phi t} = -\left[\frac{1}{\gamma\alpha}\left(-\gamma^2\beta f\dot{\Phi} + f(\gamma^2\beta^2 - \alpha^2)\Phi' + (-\alpha^2 f' - \dot{f}\beta\gamma^2 + f'\gamma^2\beta^2)\Phi\right) + \frac{f\dot{k} - 2k\dot{f}}{f}\right]\sin\theta Y_\theta .$$

k is an arbitrary gauge function and the choice $k = 0$ generates a metric in the so called Regge-Wheeler gauge. For making the equations more readable all (ℓ, m) indices were suppressed and the notation $Y_\theta \equiv \partial_\theta Y$ and $Y_\phi \equiv \partial_\phi Y$ was used.

How can a specific type of initial data be implemented through this formalism? One can look at Eq. (132) as an initial value problem for which, since the equation is second order in the time derivatives, specifying any arbitrary $\Phi(r, t = 0)$ and $\dot{\Phi}(r, t = 0)$ is allowed and sufficient for constructing a solution $\Phi(r, t)$ at all times. That means that one can choose Φ and $\dot{\Phi}$ freely and construct the corresponding metric through the equations given above. Doing this one replaces all $\ddot{\Phi}$ by the right hand side of the Regge-Wheeler Eq. (132).

If the RW function Φ_{RW} satisfies the RW Eq. (132), then the perturbed metric constructed above satisfies the linearized Einstein equations. Furthermore, it can be explicitly shown that this metric initially satisfies the linearized constraints around the Schwarzschild geometry for *any* initial values $\Phi_{RW}(t = 0, r)$ and $\dot{\Phi}_{RW}(t = 0, r)$.[4] One takes advantage of this property and constructs initial data in a simple way as a test for the new wave extraction method. For the simulations below, Kerr–Schild coordinates for the Schwarzschild background were used, and the distortion was set to $\ell = 2$, $m = 0$ with the RW function

$$\begin{aligned} \Phi_{RW}(t = 0, r) &= 0\,, \\ \dot{\Phi}_{RW}(t = 0, r) &= A\, e^{(r-r_0)^2/\sigma^2} \end{aligned} \tag{134}$$

[4]When constructing initial data for the $3+1$ quantities, one also needs to take time derivatives of the four-metric; where second time derivatives of Φ_{RW} appear, one uses the RW equation to trade these for space derivatives.

with parameters r_0 and σ. This corresponds to a Gaussian pulse of width σ centered at $r = r_0$.

Under the assumption that one can Taylor–expand (a suitable norm of) the discrete non-linear constraints in terms of the perturbation amplitude A for any fixed grid spacing h, one has

$$\mathcal{C}(A,h) = \mathcal{C}(A,h)|_{A=0} + A \left.\frac{\partial \mathcal{C}(A,h)}{\partial A}\right|_{A=0} + \frac{A^2}{2} \left.\frac{\partial^2 \mathcal{C}(A,h)}{\partial A^2}\right|_{A=0} + \mathcal{O}(A^3)\,. \tag{135}$$

Since in the continuum the linearized constraints are satisfied, the first two terms in the above expansion vanish for $h \to 0$, but otherwise are of the order of the truncation error. For small enough A the first term (that is, the background contribution) dominates, and the term $C(A,h)$ appears to be independent of A. For large enough A, on the other hand, the quadratic term in the expansion given by Eq. (135) will dominate.

Fig. 22 presents numerical evidence that this expected behavior is indeed the case. Numerical data are set up according to Eq. (134), with perturbation amplitudes A between 10^{-6} and 10^{-1}. The radial domain extent is $1.8 \leq r \leq 7.8$, the perturbation is centered around $r_0 = 4.8\,M$ and has a width of $\sigma = 1.0\,M$. The discrete Hamiltonian and momentum constraints $\mathcal{H}$ and $\mathcal{M}^i$ for these initial data sets are then computed, using the same (high) resolution, namely 109×109 grid points on each block in the angular direction and 406 points in the radial direction, corresponding to $\Delta r \approx 0.0148\,M$. Due to the symmetry of the six-block structure and the axisymmetry of the initial data, two components of the discrete momentum constraints coincide, $\mathcal{M}^x = \mathcal{M}^y$, and the latter is therefore not shown. The behavior of the constraints in the L_2 and the L_∞ (not shown in the figure) norms agrees with Eq. (135): for small amplitudes A, the discrete constraints at a fixed resolution appear to be independent of A, while for large amplitudes they show the expected quadratic dependence on A. Also shown is that the discrete constraint violations of the initial data sets have the expected dependence on resolution. For small

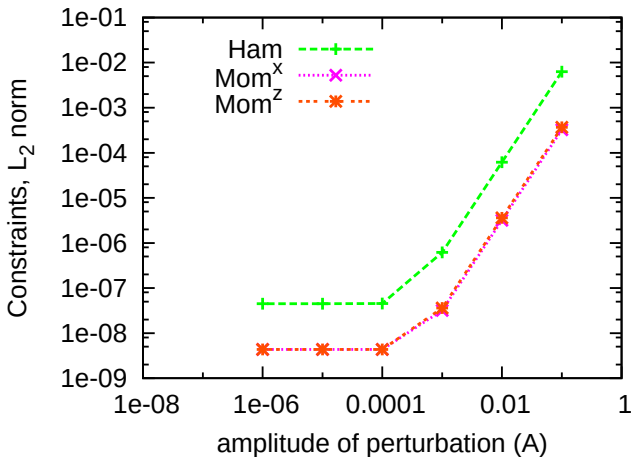

Figure 22: Discrete constraint violations for various perturbation amplitudes A at a fixed (high) resolution. Shown is the L_2 norm for the Hamiltonian constraint and for two components (x and z) of the momentum constraint (which turn out to be very close to each other, as the plot shows). The numerical resolution is 109×109 grid points per block in the angular directions and $\Delta r \approx 0.0148$ in the radial direction. The behavior is as expected and as described in the body of this thesis: for sufficiently small amplitudes, the background contribution dominates the discretization error in the constraints, which then appear to be independent of A. For large enough amplitudes, the constraint violation has a quadratic dependence on A (with an exponent of 2.01 ± 0.01 for the resolution shown in this figure), since for the initial data only the linearized constraints (around Schwarzschild) are satisfied.

amplitudes and coarse resolutions, the contribution of the quadratic term in Eq. (135) is sufficiently small, so that the constraints seem to converge towards zero. However, for any given amplitude A a fine enough resolution h reveals that the convergence is actually towards a small but non-zero value, determined by the quadratic term in the expansion Eq. (135). This behavior is shown in Fig. 23. As an illustration a convergence test is shown for $\mathcal{H}$ by comparing initial data for different resolutions. The highest resolutions are identical to those used in Fig. 22. The other four resolutions shown are $73 \times 73 \times 271$, $49 \times 49 \times 181$, $25 \times 25 \times 91$, and $17 \times 17 \times 61$ grid points per block, corresponding to $\Delta r \approx 0.0222\,M$, $0.0333\,M$, $0.0667\,M$, and $0.1\,M$, respectively.

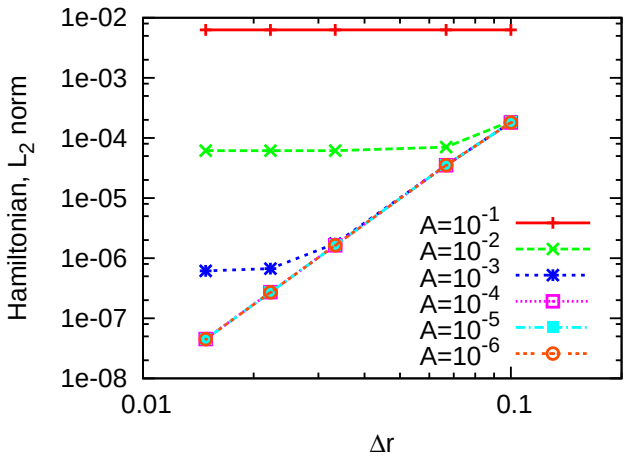

Figure 23: L_2 norm of the Hamiltonian constraint for different amplitudes A of the perturbation and for different numerical resolutions h. The coarsest resolution uses 17×17 points per block in the angular directions and $\Delta r = 0.1\,M$ in the radial direction. The resolution in all directions is increased up to 109×109 points in the angular directions and $\Delta r \approx 0.0148\,M$ in the radial direction. Since only the linearized constraints are satisfied, the non-linear constraints do not converge to zero. For sufficiently large perturbation amplitudes and for sufficiently fine resolutions, the non-linear effects become visible, and the constraint violations converge to a constant value which depends on the amplitude A. As shown in Fig. 22, this dependence is quadratic, as expected.

5.6 Description of the Simulations

The D_{8-4} operator constructed in Chap. 3 is used, a summation by parts operator [53, 54] which is eighth order accurate in the interior and fourth order accurate at the boundaries, optimized to minimize its spectral radius and boundary truncation errors. Fifth order global convergence is expected [147, 57]. The integration in time is done with a fourth order Runge–Kutta integrator with adaptive time stepping as described in Chap. 2.4 and [64]. To guarantee well posedness and numerical stability, maximally dissipative outer boundary conditions are applied. These boundary conditions are not physical in the sense that they violate the constraints and do not include back-scattered radiation from outside of the simulation domain. For that reason in the simulations shown below, the outer boundaries are placed at large enough distances so that the extracted waves are causally disconnected from boundary effects.

In order to test both the long term stability and the convergence of the code, first a Kerr black hole in Kerr–Schild coordinates with spin $j = 0.5$ is evolved. Fig. 24 shows the L_2 norm of the Hamiltonian constraint vs. time for two different resolutions. The radial domain extent is $1.8\,M < r < 11.8\,M$. The coarse resolution corresponds to $\Delta r = 0.2\,M$ and 16×16 points per block in the angular directions, and the fine resolution increases the number of points in all directions by a factor of 1.5. Approximate fifth order convergence is seen, as expected.

In the simulations discussed below, the inner boundary is placed at $r = 1.8\,M$ and the outer boundary at $r = 251.8\,M$. This allows for observer locations up to $r = 80\,M$, which are still causally disconnected from the outer boundary for times long enough to follow the ringdown, namely up to $t = 280\,M$. Initial data are set up according to Eq. (134) with $A = 0.01$, $\sigma = 1.0\,M$, and $r_0 = 20\,M$, where M is the mass of the black hole when the perturbation is switched off. The coarse resolution uses 16×16 points per block in the angular directions and 1251 points in the radial direction, corresponding to $\Delta r = 0.2\,M$. The fine resolution uses 1.4 times as many grid points in all directions.

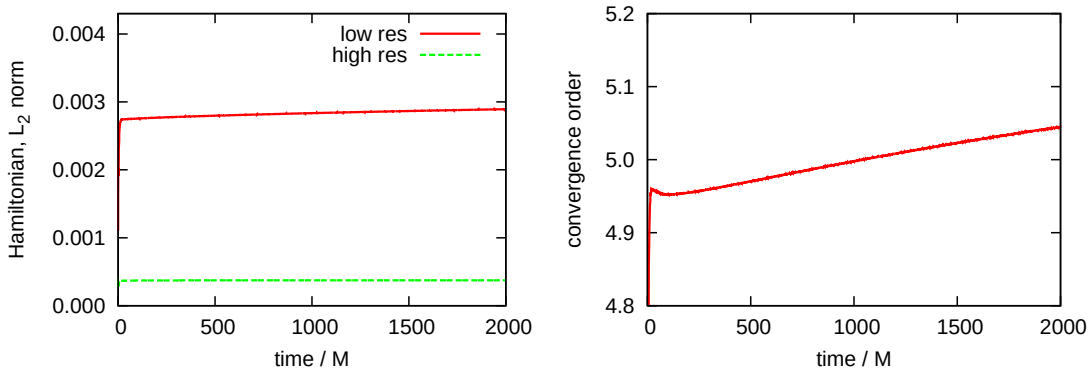

Figure 24: L_2 norm (top panel) and convergence factor (bottom panel) for the Hamiltonian constraint for evolutions of a Kerr black hole with spin $j = 0.5$. The coarse resolution corresponds to 16×16 points per block in the angular directions and $\Delta r = 0.2\,M$ in the radial direction. The fine resolution a factor of 1.5 higher in all directions. Fifth order convergence is seen, as expected for the difference operators used.

One of the goals of the analysis that follows is to study the effect of the choice of the background metric on the accuracy of the waveforms. Since for this scattering problem solutions in closed form are not known, the waves which we extract from the three-dimensional simulations are compared to results obtained with an independent fourth order accurate one-dimensional code which solves the Regge-Wheeler Eq. (132). These 1D results were obtained with a resolution of $\Delta r = 0.0125\,M$. The relative difference in this Regge-Wheeler function to a result from twice this resolution lies roughly between roundoff error and 10^{-7}, which is far below the numerical errors that are expected from the 3D simulations. Therefore, one can consider these 1D results in the following to be exact for all practical purposes.

5.7 The Standard and Generalized RW Approaches: Numerical Comparisons

Now the results of evolving distorted black holes as described above and extracting gravitational waves with different methods can be analyzed.

Fig. 25 shows Regge-Wheeler functions for observers at $r = 20\,M$, $40\,M$, and $80\,M$, extracted with both the generalized approach and the standard one. The data have been

scaled by a factor of 100 to normalize to an initial data amplitude $A = 1$ in Eq. (134). Recall that weak waves of amplitude $A = 0.01$ were used for these simulations to avoid non-linear effects, and to be able to compare with the exact solution, which is only known in the linear regime.

Five waves are shown in Fig. 25 for each observer location. Apart from the exact solution, two results obtained from the generalized approach are shown, which coincide with each other in the continuum limit. They differ in how the background metric is computed: in one case the exact expressions for the Kerr–Schild background is used, and in the other case these coefficients were numerically calculated by extracting the $\ell = 0$ part of the metric, as explained in sect. 5.4.

Finally, two waveforms were extracted using the standard approach with two different assumptions for the background, as found in the literature: a Minkowski space-time in Minkowski coordinates, and a Schwarzschild space-time in Schwarzschild coordinates. An interesting feature which can easily be seen in eq. (131) should be highlighted. For any observer location, the waves extracted with these two background should differ only by a factor which is constant in time:

$$\Phi^{\rm Min}_{RW} \;=\; \kappa \Phi^{\rm Sch}_{RW}\,, \tag{136}$$

where $\kappa^2 = g^{\rm Sch}_{rr}$ is radial component of the Schwarzschild metric in Schwarzschild coordinates. Such a simple relationship is a direct consequence of the vanishing radial shift for these backgrounds. This expected behavior is confirmed numerically with high accuracy: at all times and for all observers one recovers this expected ratio between the two waves to double precision roundoff error.

Figure 25 suggests that, as expected, the differences between waves extracted with different methods decrease as the extraction radius increases. At $r = 80\,M$, the curves show excellent agreement and cannot be distinguished by eye. For a more thorough com-

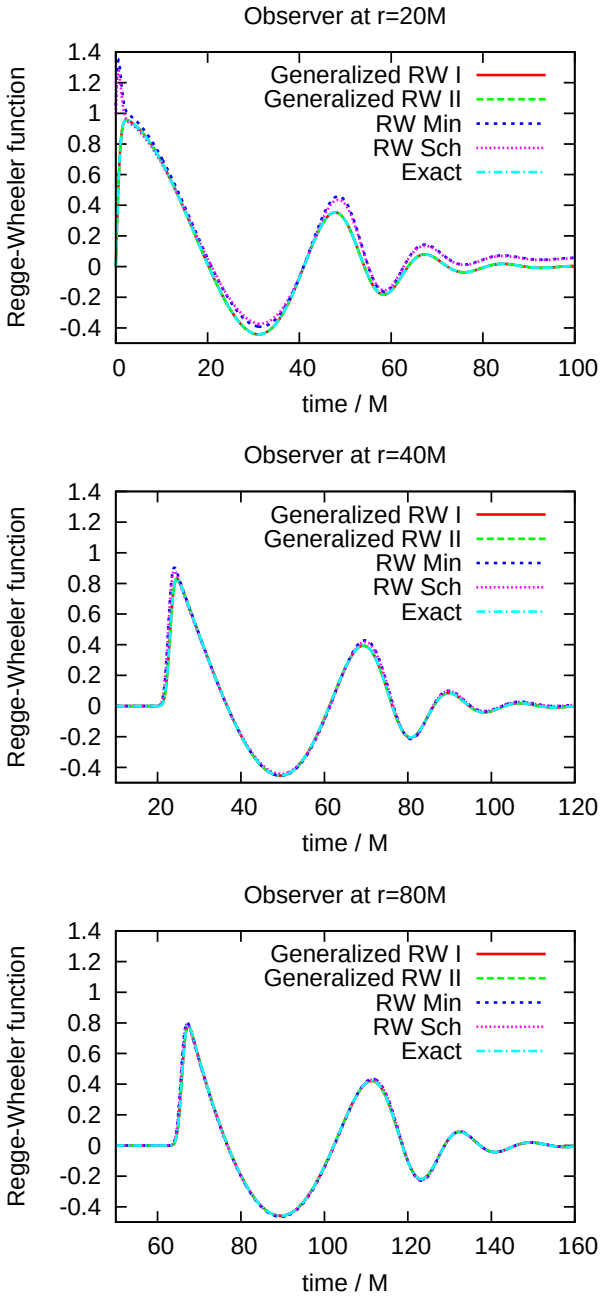

Figure 25: Extracted waveforms for observers at $20\,M$, $40\,M$, and $80\,M$. Shown is the Regge-Wheeler function obtained from the standard RW approach and the generalized one. For the former both a Minkowski background and a Schwarzschild background in Schwarzschild coordinates were assumed, labeled as *RW Min* and *RW Sch*, respectively. For the generalized approach the results for two cases, in which the background metric is dynamically computed from the numerical solution (*Generalized RW I*), and where it is prescribed analytically (*Generalized RW II*) are shown. Also shown is the exact waveform. These simulations were performed with a resolution of 16×16 grid points in the angular directions on each block and $\Delta r = 0.2\,M$ in the radial direction. See the main text for more details.

parison, one looks at the differences between the extracted waves and the exact solution in Fig. 26. For consistency with Fig. 25, the errors were also scaled relative to the initial amplitude of the perturbation.

Perhaps the most notable feature in Fig. 26 is that the differences between the waves obtained from generalized approach either with a numerically obtained background metric or with the exact (Kerr–Schild) background metric are smaller than the difference to the exact solution. For all practical purposes one can therefore consider them identical to each other, and for the rest of this chapter the latter is left out of the discussion.

Fig. 26 also shows that the standard approach—with either a Minkowski or Schwarzschild background—leads to errors which are considerably larger than the errors in the generalized approach, even for an observer at $r = 80\,M$. For the specific resolution that was used for Fig. 26, the errors at $r = 20\,M$ with the standard method are roughly three orders of magnitude larger than the errors with the generalized method. For $r = 40\,M$ and $80\,M$, the ratio of the errors is of the order 10^3 to 10^1 and 10^2 to 10^0, respectively.

The previous discussion only analyzes the errors introduced by the standard method at a fixed resolution. Next the dependence of these results on the resolution is discussed. It turns out that the difference between the different methods is even more striking for higher resolutions. By construction, the generalized wave extraction method should give the exact waveform in the continuum. At the discrete level, its associated errors should converge away with increasing resolution. Fig. 27 shows that this is actually the case. On the other hand, the errors in the standard approach do *not* converge to zero, as shown in Fig. 27. In other words, the accuracy of the extracted waves with the standard method is dominated by the extraction procedure and not by the numerical resolution.

Fig. 27 as well as the second panel of Fig. 26 show another interesting feature. Contrary to expectation, assuming Schwarzschild–like coordinates instead of a Minkowski background does not necessarily lead to smaller errors in the waveforms. For example, for

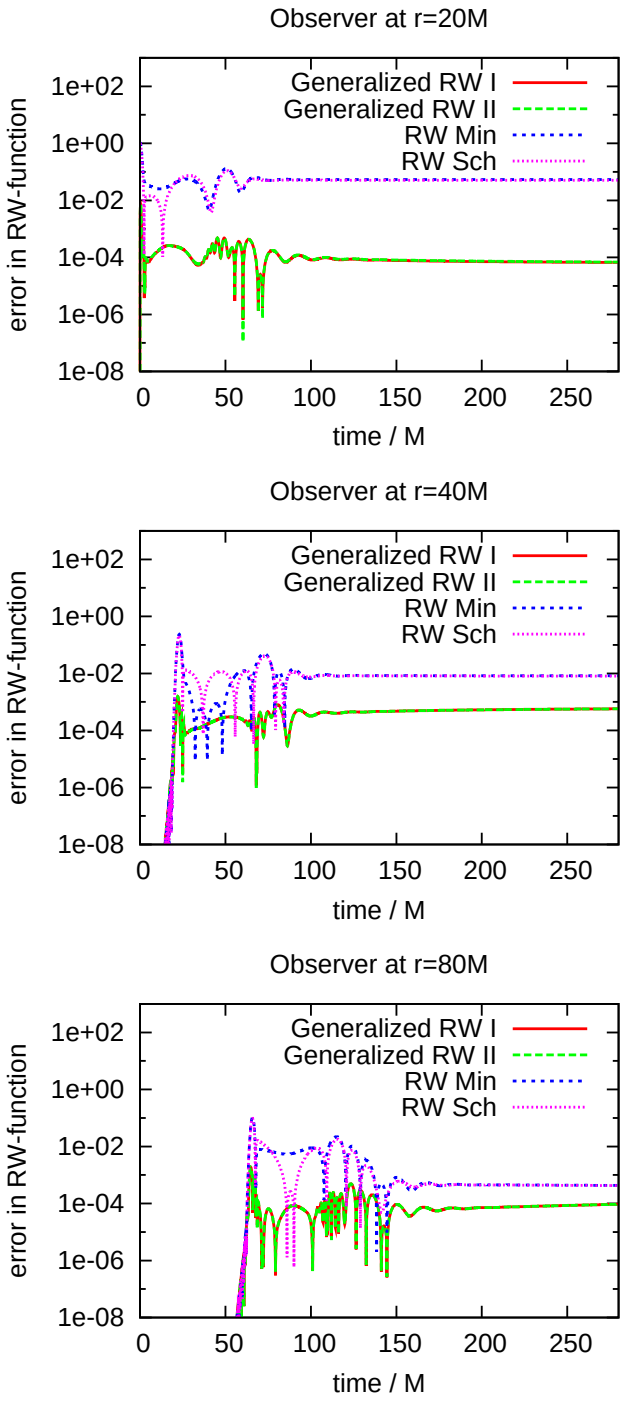

Figure 26: Errors for the waveforms shown in Fig. 25.

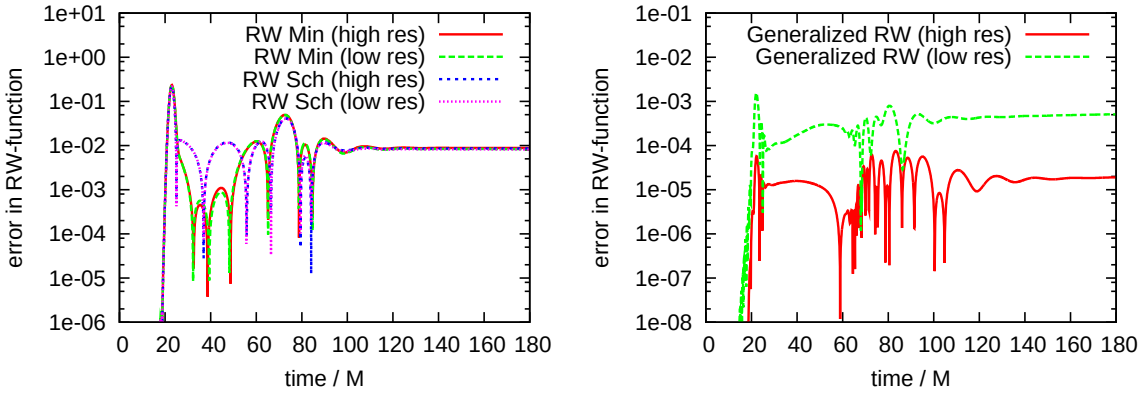

Figure 27: Shown is a convergence test for the simulations presented in the previous two figures. The plots labeled with "low res" coincide with the ones shown in the previous figures, while the plots labeled with "high res" correspond to 1.4 times that resolution. The error in the generalized wave extraction method, which by design gives the correct waveform in the continuum for these simulations, converges towards zero as expected. On the other hand, the errors in the standard wave extraction method are almost unaffected by the increased resolution. This indicates that these errors are dominated by the extraction method itself, not by the numerical truncation error. These results correspond to an observer at $40\,M$, but they look similar for the other extraction radii that are considered in this thesis.

an observer at $r = 40M$ and during the time interval of about $25M < t < 50M$, the errors are actually up to one order of magnitude larger for the Schwarzschild–like coordinates. However, as can be seen from Fig. 26, this feature depends on the observer location. One can assume that this feature is only a coincidence.

The plateau in the errors seen in the last $100\,M$ to $200\,M$ in Fig. 26 is due to an offset in the waveform. It is found that, once the wave function decays to a small enough amplitude, it no longer oscillates around zero, but instead oscillates around a certain offset. This can be seen more clearly from the top panel in Fig. 25. This offset is present for both the standard and the generalized extraction methods; however, there are important differences. The first is that the offset for the generalized extraction the offset converges to zero with increasing resolution, unlike for the standard method. The other is that the offset for generalized method is orders of magnitude smaller than for the standard method. As it will be discussed in the next subsection, that has direct consequences when

attempting to extract quasinormal frequencies. This offset is reminiscent of the one that is present in RWZ waveforms when there is spin [148, 149].

The oscillatory feature of the wave can be followed for a longer time if the offset is subtracted from the waveform by hand, that is, if the wave is shifted along the vertical axis so that it oscillates around zero at late times. This is done by fitting the data to an exponentially decaying wave with an offset. (Details about the fit are given in the following subsection) The actual values that were determined for the offset are given in Tab. 8. As expected, the offset is decreasing with increasing radius for both standard RW wave extraction methods. This offset is mainly a result of the wrong assumption about the background metric, not of numerical error. There is no such clear dependence on the radius when using the new generalized extraction. Here the offset originates solely from truncation error, and converges to zero with increasing resolution. This behavior can also be seen in Fig. 27.

Table 8: Values of the offset for different wave extraction methods and observers at $20M$, $40M$ and $80M$.

Extraction Method	Observer	Offset
Generalized RW	$20M$	-7.1×10^{-5}
Generalized RW	$40M$	5.6×10^{-4}
Generalized RW	$80M$	8.9×10^{-5}
RW Min	$20M$	-5.4×10^{-2}
RW Min	$40M$	-8.3×10^{-3}
RW Min	$80M$	-4.4×10^{-4}
RW Sch	$20M$	-5.1×10^{-2}
RW Sch	$40M$	-8.1×10^{-3}
RW Sch	$80M$	-4.3×10^{-4}

Fig. 28 shows the difference between the waveforms shifted by different offset values and the exact solution, for the same observers as before. As can be seen from the figure, the qualitative statements about the accuracies of the different wave extraction methods remain unchanged, if you consider the time span during which the amplitude of the wave

is significant.[5] It is concluded that the main errors in Fig. 26 are *not* caused by an overall offset in the whole waveform.

5.8 Quasinormal Frequencies

Now attention is turned to extracting quasinormal frequencies from the waveforms just discussed. The primary goal is to find out whether these frequencies are affected by the choice of a specific wave extraction method, which may have some presumably small but non-vanishing systematic error for any finite extraction radius, and if so, by how much. Data from the lower resolution run that we already analyzed in the previous chapter are used. The accuracy of the frequency does not change significantly if one uses the higher resolution run instead.

The angular part of the initial data is a pure $\ell = 2$, $m = 0$ mode. Since the background has no angular momentum, there is no mode–mode coupling at the linear level, while non-linear coupling can be neglected for the current study, because only weak perturbations are evolved. Therefore the only dominant multipole mode present in the data at all times should be the one injected initially. At the numerical level, $\ell = 4$ modes can be generated by the six-block grid structure. However, in Chap. 4 it was found that in the absence of angular momentum, these modes not only converge to zero with resolution, but are also very small for the resolutions considered in this chapter. In the above reference and in [83] it was also shown that overtones are not significantly excited unless the black hole is very rapidly rotating. Based on all this, the fit is done only for a single $\ell = 2$, $m = 0$ mode:

$$\Psi_{RW}^{fit} = \mathcal{A} \sin(\omega_r t + \chi)\, e^{\mathrm{i}\omega_i (t - t_0)} - \xi \tag{137}$$

where $\mathcal{A}$ is the excitation amplitude, $\omega = \omega_r + \mathrm{i}\omega_i$ is the complex quasinormal mode frequency, χ is a phase shift, ξ is the offset and t_0 is the starting time of the quasinormal ringing regime. The latter is not unambiguously defined (the so called *time-shift problem*),

[5] Of course, because the offset is subtracted by hand to decrease the errors at late times, one can naturally follow the oscillatory part of the wave for longer times before.

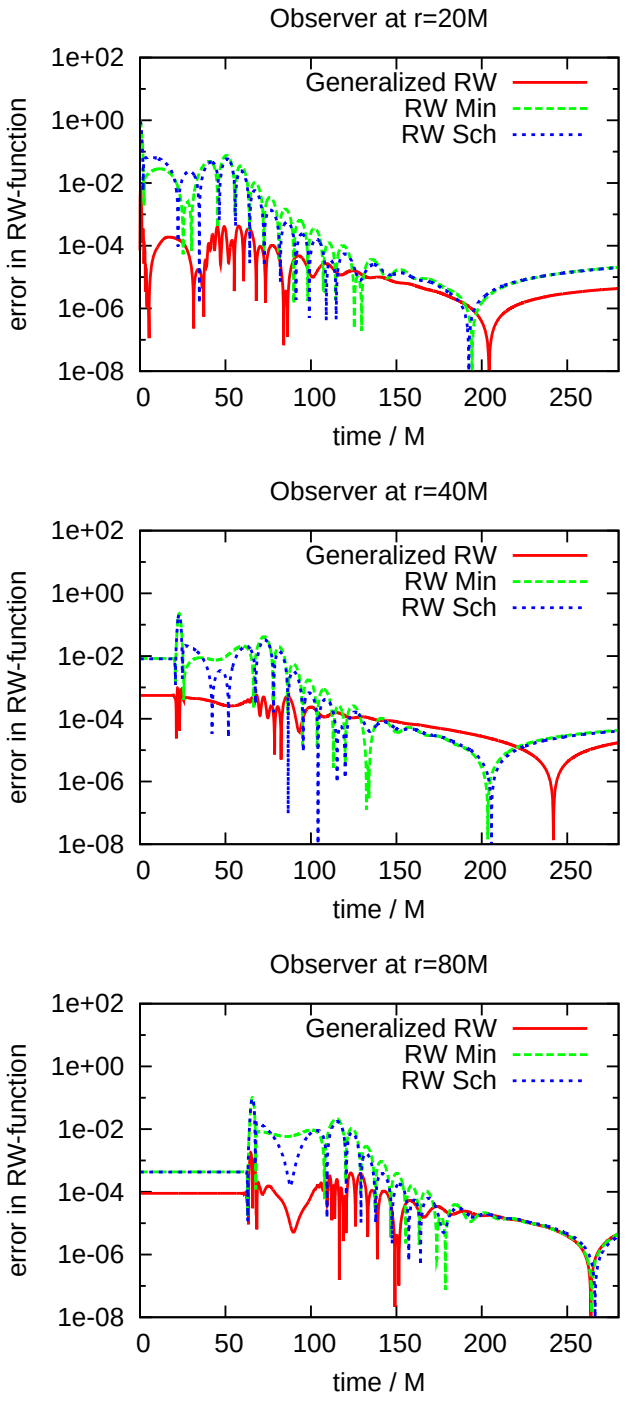

Figure 28: Shown are the same quantities as in Fig. 26, except that an offset is subtracted from each waveform before calculating the errors. See the main text for details.

and as a consequence neither are the amplitudes of quasinormal modes. In Chap. 4 it was proposed to minimize the uncertainties due to this time-shift problem by looking at carefully chosen relative amplitudes. In order to fit numerical data to Eq. (137), one fixes t_0 to an educated guess[6] and then fit for ω, $\mathcal{A}$, χ, and ξ. Any difference in t_0 is absorbed in $\mathcal{A}$ (in which is not important at this point) and does not change the other extracted parameters. One finds the time-window of optimal fitting by looking for a local minimum in the relative residual between the original waveform and its fit. In Chap. 4.9 it was found that such a local minimum is usually quite sharp and therefore gives a good criteria for choosing the window of time where the quasinormal ringing dominates. Similarly, the uncertainties in this minimum are used to quantify the errors in the parameters obtained in the fit. More details about the fitting procedure that is used to extract quasinormal parameters are given in Chap. 4.

The previous subsection discussed the presence of an offset in the extracted waves with the standard method. If such an offset is not taken into account when fitting for the quasinormal frequencies (i.e., for a fixed $\xi = 0$), Eq. (137) does not represent the behavior of the numerical data well enough, and no reasonable results can be obtained from the fit. This is especially the case at medium to late time intervals when the amplitude becomes smaller than the offset, so that the wave does not cross zero any more. When one tries to fit for these cases, the obtained frequency has no relation at all to the correct QNM frequency. For example, at $r = 20M$ the offset in the waves obtained from the standard RW wave extraction is of order 10^{-2} for both a Minkowski background and for Schwarzschild–like coordinates. Without taking the offset into account, the value of ω_r that the fit determines lies between 10^{-14} and 10^{-4}, and ω_i is of order 10^{-3} to 10^{-6}. In contrast, the offset resulting from the generalized RW wave extraction is of order 10^{-5}

[6]For example, taking into account where the initial data and observer are located, and assuming a propagation speed of one

for this resolution. This is small enough that the problems described above do not play a noticeable role.

Table 9: Quasinormal frequencies of the $\ell = 2, m = 0$ mode as measured by an observer at $r = 20\,M$. Results are given for waveforms resulting from the different extraction methods used. The predicted frequency from perturbation theory, which it is assumed to be exact because the perturbation amplitude is small, is $\omega_{\rm exact} = 0.37367 - 0.08896\mathrm{i}$ [87]. The uncertainties in the extracted frequencies originate from variations in them depending on which interval of the waveform is used for the fit. The relative error is defined as $|(\omega - \omega_{\rm exact})/\omega_{\rm exact}|$.

Extraction Method	ω	relative error
Generalized RW	$0.3736 - 0.0890\mathrm{i} \pm (3 + 3\mathrm{i}) \times 10^{-4}$	$1.9 \times 10^{-4} + 4.5 \times 10^{-4}\mathrm{i}$
RW Min	$0.3733 - 0.0889\mathrm{i} \pm (3 + 3\mathrm{i}) \times 10^{-4}$	$9.9 \times 10^{-4} + 6.7 \times 10^{-4}\mathrm{i}$
RW Sch	$0.3733 - 0.0889\mathrm{i} \pm (3 + 3\mathrm{i}) \times 10^{-4}$	$9.9 \times 10^{-4} + 6.7 \times 10^{-4}\mathrm{i}$

Tab. 9 shows the complex quasinormal frequencies that were obtained from the generalized and from the standard RW methods. As mentioned above and discussed in detail in ref. [150], the error bars are estimated from changes in the frequency when changing the time interval that is used for the fit of the waveform. It is assumed that the predicted frequency from perturbation theory for the fundamental $\ell = 2$, $m = 0$ mode is exact because a small amplitude for the perturbation is used. This frequency is known to be $\omega_{\rm exact} = 0.37367 - 0.08896\mathrm{i}$ (see for example [87]). The frequency obtained from the new generalized wave extraction is consistent with this exact value within the accuracy to which one can obtain these numbers from the fit itself. For the standard wave extraction method, one only finds agreement to three significant digits in the real part, but better agreement with the exact value in the imaginary part of the waveform. Note that, since the waveforms only differ by a constant factor (see Chap. 5.7), the frequencies obtained with a Minkowski and a Schwarzschild background agree to roundoff error. The reason for the lower accuracy in the real part of ω might be due to the fact that the waveforms are slightly distorted due to the wrong assumption for the background metric. This causes a larger residual between the data and the fit—it is about a factor of two larger than with

the generalized wave extraction—and some degradation in how accurately certain fitting unknowns like ω can be determined. That may also explain the larger relative error for the waves extracted with the standard RW wave method, which is shown in the right column of the same table. There the relative error is defined as $|(\omega - \omega_{\text{exact}})/\omega_{\text{exact}}|$.

5.9 Summary

The question was addressed how certain approximations that are commonly done in wave extraction algorithms affect the accuracy of the extracted waveforms. It was studied how sensitive results are to the location of the observer and to certain assumptions made about the background geometry. The question was posed if one can locate observers far enough away from the radiation source, so that the total errors in the waveforms are dominated by numerical truncation error, instead of systematic errors from the wave extraction method.

To avoid some of the complexities in asking these kind of questions, a very specific physical system was looked at, a perturbed Schwarzschild black hole, where the perturbation is of odd parity. It can be argued that statements made in this chapter have some relevance for more complicated cases, like black hole binaries, since many of such systems develop into a single perturbed black hole.

The wave extraction methods that were compared are based on the Regge-Wheeler formalism which was used in it's standard form, assuming Minkowski and Schwarzschild background geometries and in a generalized covariant form for which the black hole parameters were extracted directly from the numerically computed metric.

It was found that for the standard RW wave extraction method even at observer locations of $r = 80M$ the errors are indeed of systematic nature. By doing tests with different resolutions it was possible to show that they do not converge to zero with decreasing grid spacing. On the other hand, the errors in the waves extracted using the generalized formalism showed numerical convergence which indicates that they originate from the discretization. It should be stressed that even for the standard method the errors in the waveforms are small enough so that the method can give useful results. Also one needs

fairly accurate numerical methods to see the effects that were presented. Nonetheless it is important to notice that there is a fundamental limit in accuracy that cannot be overcome by refining the numerics beyond a certain point when using the traditional RW wave extraction. The errors decay with increasing the extraction radius, but in a very slow way, typically with $1/r$ (which is in fact the decay found in the simulations). For example, in order to decrease the systematic errors for an observer at $40\,M$ shown in Fig. 27 by, say, two orders of magnitude, by just moving the observer out and extracting at a single extraction radius, the latter would have to be located at $\simeq 4,000\,M$. This means that, if similar uncertainties show up in other simulations, as the results of this chapter suggest (and which can be tested), then decreasing those uncertainties by moving the observer further out does not seem feasible, and other ideas would have to be explored.

The generalized formalism that was used here solved that problem in the specific setup of a single black hole. This is no surprise since it is adapted to exactly that situation. For more general cases like spinning black holes or even binaries, the errors with this formalism will be larger, but it can be argued that at least for the ring-down phase of the black hole, it will give more accurate results than the traditional approach.

What is not clear, however, is whether the wave zone resolution currently used by mesh refinement codes is sufficient to see the differences that were demonstrated in this chapter. For example, the spatial resolutions in the wave zone of current binary black hole inspiral and coalescence simulations are usually much coarser than the resolutions that were used above. Some radial resolutions h in the wave zone of binary black hole system simulations are: [151] $h = 0.5\,M$, [113] $h = 0.5\,M$ (but the extraction is performed very close in at $R = 16M$) [152] $h = 0.75\,M$ (but $h = 1.5\,M$ for calculating the radiated angular momentum J), [153] $h = 0.85\,M$, [154] $h = 0.87\,M$ [117] $h = 0.82\,M$, [118]

$h = 0.56\,M$, [155] $h = 0.56\,M$. Some of these codes are 4th order accurate, but many have at least certain components that are only 2nd order accurate.[7]

By subtracting offsets in the waveforms via postprocessing, the quasi normal modes could be extracted using a fitting procedure. For all extraction methods they agreed to high accuracy with the expected values. However it was demonstrated that the largest errors in the waveforms were not due to an overall offset in the whole wave. Even after removing the offset by hand, at early and intermediate times in the ringing regime the errors remained at roughly the same order. It should be stressed that for the postprocessing some a priori knowledge about the waveforms was used, namely that they should oscillate around zero. In more general scenarios such features might not be known and a similar method might not be applicable.

[7]While it is currently common practice to report the finest resolution (near the horizons) and the coarsest resolution (near the outer boundary) in such simulations, the resolution in the wave zone, i.e., at the location where the gravitational waves are extracted, is often not explicitly listed, and can sometimes not be inferred. Some publications also do not report at which coordinate radius the wave information is extracted.

6 Conclusions

This thesis presented a careful study of some aspects of gravitational wave physics. First a description of a new multi-block infrastructure for numerical relativity was given and numerical evidence was shown that it is suitable for highly accurate and efficient simulations. The primary reason for this new code to be that successful is that it gives the opportunity to better adapt coordinates to the specific physical systems that are modeled. Also by using and extending very recently developed techniques in numerical analysis, it is guaranteed that the code is numerically stable for arbitrary high order schemes. In the specific case of single perturbed black holes, computational performance and accuracy was gained because of the possibility to choose angular and radial resolution independently. This is a feature that can not be achieved with mesh refinement codes that are based on cartesian grids and coordinates. The multi-block method also provides spherical excision and outer boundaries. In the work done here, no attention was payed to the construction of physical outer boundary conditions, since it was possible to have them causally disconnected from the regions from which the physical information was extracted. Instead in most simulations maximally dissipative boundary conditions were applied to guarantee well posedness and therefore numerical stability. The excision boundary condition could be set in a very straightforward way due to its spherical shape. The choice of a six block system also simplified wave extraction on the technical side, since the necessary integrations could be done on constant coordinate radius spheres without the need for interpolation. These advantages are so striking that the author is convinced that the effort to develop such an infrastructure and numerical methods will pay off in the long term and make numerical relativity more efficient, accurate and robust.

The new infrastructure was used for a numerical study of quasinormal mode excitation of Kerr black holes. The relative excitation strength of co- and counter-rotating modes, and how they depend on the shape of the initial perturbation was investigated. A quantitative analysis of linear mode-mode coupling due to the spin of the black hole

was given. Finally the excitation of overtones for rapidly rotation black holes with spin up to $j = 0.98$ was looked at. For analyzing the data in a precise and correct way, a well defined procedure to extract frequencies and excitation amplitudes from the numerical waveform was proposed, which is based on fitting the data to a superposition of exponentially decaying sine functions with different frequencies and decay rates. It was found that the general correctness and accuracy of the results as well as the number of modes that can be extracted from the data depend in a sensitive way on how this fit is done in detail, for example on the number of modes that one is fitting at the same time and on the time interval of the data that is used for the analysis. A detailed description of all the related issues that were encountered was given. Furthermore the so called *time shift problem* was identified, a conceptual problem in giving a precise definition for the excitation amplitudes. The tests were designed in a way that the effect of this problem is minimal. The details of the fitting procedure, especially finding an optimal time window for it, as well as the time shift problem have been widely ignored in all numerical studies to date. A comparison between the quasinormal frequencies computed with the new multi-block code and independent perturbative predictions was done to test the accuracy of the methods. By comparing excitation amplitudes computed by both methods it could be tested to what extend assumptions that are required by the perturbative predictions hold.

Then the problem of wave extraction in full non-linear evolutions of the Einstein equations was looked at. For that a generalized harmonic evolution system was implemented and initial data that represent a single distorted Schwarzschild black hole were evolved. Odd parity waves were extracted using the standard and a generalized covariant Regge-Wheeler formalism at a number of different extraction radii between $r = 20M$ and $r = 80M$. The errors with respect to the exact solution were investigated and how they depend on the observer location and the assumption about the background metric. It was

found that even at large radii, the systematic errors due to the assumption of a wrong background dominate over numerical discretization error.

There are many directions in which the research presented here could be continued. The multi-block infrastructure as well as the generalized harmonic code are in a fairly complete state and should in principle be capable of doing binary black hole simulations. There are several approaches for doing that. One can use a global coordinate frame that rotates in a way that the two black holes are kept fixed on the numerical grid [39]. This has the advantage of avoiding moving excision regions, a concept that is somewhat difficult to realize with the touching grids method implemented for this thesis. During the merger, one could simply drop some of the grids in the center of the multi-block system to get a single spherical excision region. A more straight forward way to treat binaries might be to build on the expertise from recent successful moving puncture evolutions and evolve the black holes on a central cartesian block which is then surrounded by a number of blocks so that at larger radii the coordinates become almost spherical. This would preserve the advantage of constant angular and radial resolution at least in the wave zone, simplified wave extraction and smooth outer boundaries. However, one would loose the adapted grid structure close to each black hole. As a result, in order for the simulations to be accurate one would need mesh refinement in the central block. In principle this could be done with the code described in this thesis, since Carpet allows for both.

There is a wide range of different research areas in general relativity and astrophysics that can profit from multi-block methods and also from the specific implementation presented here. Recently attempts were started to apply the new code to general relativistic hydrodynamics simulations, for example of collapsing stars. Other interesting applications are simulations of compactified space-times that include null infinity, which has a spherical topology. In fact for any computation on a manifold with non-trivial topology multi-block or similar methods are necessary.

Predicting excitation amplitudes for quasinormal modes certainly is of interest to the gravitational wave observatories and data analysis efforts. There is a need to further explore the effect of initial configurations on the mode excitation especially for physically relevant situations. An interesting question would be, what the dominant modes in the ringdown waveform after a binary black hole merger are. For that further numerical experiments are necessary and it has to be investigated how they relate to analytical predictions.

The work on quasinormal mode and wave extraction was a step towards a better understanding of how one should analyze numerical waveforms in a systematic way. This is an important issue that is often neglected in numerical relativity. The physical systems investigated here were comparably simple and it is an open question how well the statements made will carry over to more challenging situations, for example nonlinear perturbations or even binary merger cases. In addition to that a study like in Chap. 5 should be repeated for perturbations of even parity and a comparison to extraction methods based on the Weyl scalar Ψ_4 would be important to do.

References

[1] T. Goodale, G. Allen, G. Lanfermann, J. Massó, T. Radke, E. Seidel, and J. Shalf. The Cactus framework and toolkit: Design and applications. In *Vector and Parallel Processing – VECPAR'2002, 5th International Conference, Lecture Notes in Computer Science*, Berlin, 2003. Springer.

[2] Cactus Computational Toolkit home page.

[3] LAPACK: Linear Algebra Package.

[4] BLAS: Basic Linear Algebra Subroutines.

[5] Netlib Repository.

[6] Greg Burns, Raja Daoud, and James Vaigl. LAM: An Open Cluster Environment for MPI. In *Proceedings of Supercomputing Symposium*, pages 379–386, 1994.

[7] Jeffrey M. Squyres and Andrew Lumsdaine. A Component Architecture for LAM/MPI. In *Proceedings, 10th European PVM/MPI Users' Group Meeting*, number 2840 in Lecture Notes in Computer Science, pages 379–387, Venice, Italy, September / October 2003. Springer-Verlag.

[8] LAM: LAM/MPI Parallel Computing.

[9] W. Gropp, E. Lusk, N. Doss, and A. Skjellum. A high-performance, portable implementation of the MPI message passing interface standard. *Parallel Computing*, 22(6):789–828, September 1996.

[10] William D. Gropp and Ewing Lusk. *User's Guide for* `mpich`*, a Portable Implementation of MPI.* Mathematics and Computer Science Division, Argonne National Laboratory, 1996. ANL-96/6.

[11] MPICH: ANL/MSU MPI implementation.

[12] MPI: Message Passing Interface Forum.

[13] Albert Einstein. Zur algemeinen relativitätstheorie. *Preuss. Akad. Wiss. Berlin, Sitzungsber.*, pages 778–786, 1915.

[14] Albert Einstein. Die feldgleichungen der gravitation. *Preuss. Akad. Wiss. Berlin, Sitzungsber.*, pages 844–847, 1915.

[15] LIGO - http://www.ligo.caltech.edu/.

[16] LISA - http://lisa.nasa.gov/.

[17] Emanuele Berti and Kostas D. Kokkotas. Quasinormal modes of Kerr–Newman black holes: Coupling of electromagnetic and gravitational perturbations. *Phys. Rev. D*, 71:124008, 2005.

[18] Cactus Computational Toolkit. `http://www.cactuscode.org`.

[19] Adaptive mesh refinement with Carpet. `http://www.carpetcode.org/`.

[20] Erik Schnetter, Peter Diener, Nils Dorband, and Manuel Tiglio. A multi-block infrastructure for three-dimensional time-dependent numerical relativity. *Class. Quantum Grav.*, 23:S553–S578, 2006.

[21] Paolo Secchi. The initial boundary value problem for linear symmetric hyperbolic systems with characteristic boundary of constant multiplicity. *Differential Integral Equations*, 9:671–700, 1996.

[22] L. Rezzolla, A. M. Abrahams, Richard A. Matzner, M. E. Rupright, and Stuart L. Shapiro. Cauchy-perturbative matching and outer boundary conditions: computational studies. *Phys. Rev. D*, 59:064001, 1999.

[23] S. Brandt, R. Correll, Roberto Gómez, Mijan F. Huq, P. Laguna, Luis Lehner, P. Marronetti, R. A. Matzner, D. Neilsen, J. Pullin, E. Schnetter, D. Shoemaker, and Jeffrey Winicour. Grazing collisions of black holes via the excision of singularities. *Phys. Rev. Lett.*, 85:5496–5499, 2000.

[24] Jonathan Thornburg. Coordinates and boundary conditions for the general relativistic initial data problem. *Class. Quantum Grav.*, 4(5):1119–1131, September 1987.

[25] Gioel Calabrese and David Neilsen. Excising a boosted rotating black hole with overlapping grids. *Phys. Rev. D*, 71:124027, 2005.

[26] Luis Lehner, Oscar Reula, and Manuel Tiglio. Multi-block simulations in general relativity: high order discretizations, numerical stability, and applications. *Class. Quantum Grav.*, 22:5283–5322, 2005.

[27] Jonathan Thornburg. Black hole excision with multiple grid patches. *Class. Quantum Grav.*, 21(15):3665–3691, 7 August 2004.

[28] Deirdre Shoemaker, Kenneth L. Smith, Ulrich Sperhake, Pablo Laguna, Erik Schnetter, and David Fiske. Moving black holes via singularity excision. *Class. Quantum Grav.*, 20:3729–3744, 2003. gr-qc/0301111.

[29] Miguel Alcubierre et al. Testing excision techniques for dynamical 3d black hole evolutions. 2004.

[30] Ulrich Sperhake, Bernard Kelly, Pablo Laguna, Kenneth L. Smith, and Erik Schnetter. Black hole head-on collisions and gravitational waves with fixed mesh-refinement and dynamic singularity excision. *Phys. Rev. D*, 71:124042, 2005.

[31] F. Bassi and S Rebay. High-order accurate discontinuous finite element solution of the 2d euler equations. *J. Comput. Phys.*, 138:251, 1997.

[32] Jonathan Thornburg. *Numerical Relativity in Black Hole Spacetimes*. PhD thesis, University of British Columbia, Vancouver, British Columbia, 1993.

[33] Roberto Gómez, Luis Lehner, Philippos Papadopoulos, and Jeffrey Winicour. The eth formalism in numerical relativity. *Class. Quantum Grav.*, 14(4):977–990, 1997.

[34] Roberto Gómez, Luis Lehner, R.L. Marsa, Jeffrey Winicour, A. M. Abrahams, A. Anderson, Peter Anninos, Thomas W. Baumgarte, N. T. Bishop, S. R. Brandt, J. C. Browne, K. Camarda, M. W. Choptuik, Gregory B. Cook, R. Correll, C. R. Evans, L. S. Finn, G. C. Fox, T. Haupt, M. F. Huq, L. E. Kidder, S. A. Klasky, P. Laguna, W. Landry, J. Lenaghan, J. Masso, R. A. Matzner, S. Mitra, Philippos Papadopoulos, M. Parashar, L. Rezzolla, M. E. Rupright, F. Saied, P. E. Saylor, Mark A. Scheel, E. Seidel, Stuart L. Shapiro, D. Shoemaker, L. Smarr, B. Szilágyi, Saul A. Teukolsky, M. H. P. M. van Putten, P. Walker, and J. W. York Jr. Stable characteristic evolution of generic three-dimensional single-black-hole spacetimes. *Phys. Rev. Lett.*, 80:3915–3918, 1998.

[35] Christian Reisswig, Nigel T. Bishop, Chi Wai Lai, Jonathan Thornburg, and Bela Szilagyi. Numerical relativity with characteristic evolution, using six angular patches. 2006.

[36] Lawrence E. Kidder, Harald P. Pfeiffer, and Mark A. Scheel. private communication, 2005.

[37] Mark A. Scheel, Adrienne L. Erickcek, Lior M. Burko, Lawrence E. Kidder, Harald P. Pfeiffer, and Saul A. Teukolsky. 3D simulations of linearized scalar fields in Kerr spacetime. *Phys. Rev. D*, 69:104006, 2004.

[38] Lawrence E. Kidder, Lee Lindblom, Mark A. Scheel, Luisa T. Buchman, and Harald P. Pfeiffer. Boundary conditions for the Einstein evolution system. *Phys. Rev. D*, 71:064020, 2005.

[39] Mark A. Scheel et al. Solving einstein's equations with dual coordinate frames. *Phys. Rev.*, D74:104006, 2006.

[40] Gioel Calabrese and David Neilsen. Spherical excision for moving black holes and summation by parts for axisymmetric systems. *Phys. Rev. D*, 69:044020, 2004.

[41] Masaru Shibata and Takashi Nakamura. Evolution of three-dimensional gravitational waves: Harmonic slicing case. *Phys. Rev. D*, 52:5428, 1995.

[42] Thomas W. Baumgarte and Stuart L. Shapiro. On the numerical integration of Einstein's field equations. *Phys. Rev. D*, 59:024007, 1999.

[43] M. Carpenter, D. Gottlieb, and S. Abarbanel. Time-stable boundary conditions for finite-difference schemes solving hyperbolic systems. methodology and application to high-order compact schemes. *J. Comput. Phys.*, 111:220–236, 1994.

[44] Mark H. Carpenter, Jan Nordström, and David Gottlieb. A stable and conservative interface treatment of arbitrary spatial accuracy. *Journal of Computational Physics*, 148(2):341–365, 1999.

[45] J. Nordström and M. Carpenter. High-order finite difference methods, multidimensional linear problems and curvilinear coordinates. *J. Comput. Phys.*, 173:149–174, 2001.

[46] GridPro Program Development Company.

[47] C. Ronchi, R. Iacono, and P.S. Paolucci. The cubed sphere: A new method for the solution of partial differential equations in spherical geometry. *Journal of Computational Physics*, 124:93–114, 1996.

[48] Bertil Gustafsson, Heinz-Otto Kreiss, and Joseph Oliger. *Time dependent problems and difference methods*. Wiley, New York, 1995.

[49] P. Olsson. Summation by parts, projections, and stability I. *Math. Comp.*, 64:1035–1065, 1995.

[50] P. Olsson. *Math. Comp.*, 64:S23, 1995.

[51] P. Olsson. Summation by parts, projections, and stability II. *Math. Comp.*, 64:1473–1493, 1995.

[52] M. Svärd. On coordinate transformations for summation-by-parts operators. *J. Sci. Comput.*, 20:1, 2004.

[53] H. O. Kreiss and G. Scherer. Finite element and finite difference methods for hyperbolic partial differential equations. In C. De Boor, editor, *Mathematical Aspects of Finite Elements in Partial Differential Equations*, New York, 1974. Academica Press.

[54] H. O. Kreiss and G. Scherer. On the existence of energy estimates for difference approximations for hyperbolic systems. Technical report, Dept. of Scientific Computing, Uppsala University, 1977.

[55] B. Strand. Summation by parts for finite differencing approximations for d/dx. *J. Comput. Phys.*, 110:47, 1994.

[56] Bertil Gustafsson. The convergence rate for difference approximations to general mixed initial boundary value problems. *SIAM J. Num. Anal.*, 18:179–190, 1981.

[57] Bertil Gustafsson. The convergence rate for difference approximations to mixed initial boundary value problems. *Mathematics of Computation*, 29(130):396–406, 1975.

[58] Burkhard Zink, Peter Diener, Enrique Pazos, and Manuel Tiglio. Cauchy-perturbative matching reexamined: Tests in spherical symmetry. *Phys. Rev. D*, 73:084011, 2006.

[59] H. O. Kreiss and Liwin Wu. On the stability definition of difference approximations for the initial boundary value problem. *Applied Numerical Mathematics*, 12:213–227, 1993.

[60] Peter Diener, Ernst Nils Dorband, Erik Schnetter, and Manuel Tiglio. New, efficient, and accurate high order derivative and dissipation operators satisfying summation by parts, and applications in three-dimensional multi-block evolutions. gr-qc/0512001, 2005.

[61] M. Svärd, K. Mattsson, and J. Nordström. Steady state computations using summation by parts operators. *J. Sci. Comput.*, 24:79–95, 2005.

[62] K. Mattsson, M. Svärd, and J. Nordström. Stable and accurate artificial dissipation. *J. Sci. Comput.*, 21:57–79, 2004.

[63] Heinz-Otto Kreiss and Joseph Oliger. *Methods for the approximate solution of time dependent problems*, volume 10. World Meteorological Organization, International Council of Scientic Unions, 1973.

[64] W. H. Press, B. P. Flannery, Saul A. Teukolsky, and W. T. Vetterling. *Numerical Recipes*. Cambridge University Press, Cambridge, England, 1986.

[65] Erik Schnetter. Carpet: A Mesh Refinement driver for Cactus.

[66] Cactus benchmarking results.

[67] Luis Lehner, David Neilsen, Oscar Reula, and Manuel Tiglio. The discrete energy method in numerical relativity: Towards long-term stability. *Class. Quantum Grav*, 21:5819–5848, 2004.

[68] Gioel Calabrese, Luis Lehner, David Neilsen, Jorge Pullin, Oscar Reula, Olivier Sarbach, and Manuel Tiglio. Novel finite-differencing techniques for numerical relativity: application to black hole excision. *Class. Quantum Grav.*, 20:L245–L252, 2003.

[69] J. A. H. Futterman, F. A. Handler, and R. A. Matzner. *Scattering from black holes*. Cambridge University Press, Cambridge, Englands, 1988.

[70] C. V. Vishveshwara. Scattering of gravitational radiation by a Schwarzschild black-hole. *Nature*, 227:936, 1970.

[71] W. H. Press. Long wave trains of gravitational waves from a vibrating black hole. *Astrophys. J.*, 170:L105, 1971.

[72] R. Price. Nonspherical perturbations of relativistic gravitational collapse. I. Scalar and gravitational perturtbations. *Phys. Rev. D*, 5:2419, 1972.

[73] F. Echeverría. Gravitational-wave measurements of mass and angular momentum of a black hole. *Phys. Rev. D*, 40:3194, 1989.

[74] Lee Samuel Finn. Detection, measurement, and gravitational radiation. *Phys. Rev. D*, 46:5236, 1992.

[75] E. Berti, V. Cardoso, and C. M. Will. On gravitational-wave spectroscopy of massive black holes with the space interferometer LISA. *Phys. Rev. D*, 73:064030, 2006.

[76] Olaf Dreyer, Bernard Kelly, Badri Krishnan, Lee Samuel Finn, David Garrison, and Ramon Lopez-Aleman. Black hole spectroscopy: Testing general relativity through gravitational wave observations. *Class. Quantum Grav.*, 21:787, 2004.

[77] E. E. Flanagan and S.A. Hughes. Measuring gravitational waves from binary black hole coalescences. I. Signal to noise for inspiral, merger, and ringdown. *Phys. Rev. D*, 57:4535, 1998.

[78] E. Berti, A. Buonanno, and C. M. Will. Estimating spinning binary parameters and testing alternative theories of gravity with LISA. *Phys. Rev. D*, 71:084025, 2005.

[79] M. Luna and A. M. Sintes. Parameter estimation of compact binaries using the inspiral and ringdown waveforms. 2006.

[80] K. D. Kokkotas and B. G. Schmidt. Quasi-normal modes of stars and black holes. *Living Rev. Relativity*, 2:2, 1999.

[81] H.-P. Nollert. Quasinormal modes: The characteristic "sound" of black holes and neutron stars. *Class. Quantum Grav.*, 16:R159, 1999.

[82] E. Berti. Black hole quasinormal modes: Hints of quantum gravity? 2004.

[83] Emanuele Berti and Vitor Cardoso. Quasinormal ringing of kerr black holes. I: The excitation factors. *Phys. Rev. D*, 74:104020, 2006.

[84] E. Berti, V. Cardoso, and C. M. Will. Considerations on the excitation of black hole quasinormal modes. 2006.

[85] William Krivan, Pablo Laguna, and Philippos Papadopoulos. Dynamics of scalar fields in the background of rotating black holes. *Phys. Rev. D*, 54:4728–4734, 1996.

[86] William Krivan, Pablo Laguna, Philippos Papadopoulos, and Nils Andersson. Dynamics of perturbations of rotating black holes. *Phys. Rev. D*, 56:3395–3404, 1997.

[87] E.W. Leaver. An analytic representation for the quasi-normal modes of Kerr black holes. *Proc. R. Soc. London, Ser. A*, 402:285–298, 1985.

[88] K. D. Kokkotas and B. G. Schmidt. Quasi-normal modes of stars and black holes. *Living Rev. Relativity*, 2:2, 1999. `http://www.livingreviews.org/lrr-1999-2`.

[89] H.-P. Nollert. Quasinormal modes of schwarzschild black holes: The determination of quasinormal frequencies with very large imaginary parts. *Phys. Rev. D*, 47:5253–5258, June 1993.

[90] Hans-Peter Nollert. *Astrophysik in der Schwarzschildmetrik am Beispiel von Quasi-Normalmoden schwarzer Löcher und Lichtablenkung bei Röntgenpulsaren*. PhD thesis, Universität Tübingen, Tübingen, Germany, 1990.

[91] Emanuele Berti, Vitor Cardoso, and Marc Casals. Eigenvalues and eigenfunctions of spin-weighted spheroidal harmonics in four and higher dimensions. *Phys. Rev. D*, 73:024013, 2006.

[92] William H. Press and Saul A. Teukolsky. Perturbations of a rotating black hole. II. Dynamical stability of the Kerr metric. *Astrophys. J.*, 185:649–674, 1973.

[93] Y. Zlochower, R. Gómez, S. Husa, L. Lehner, and J. Winicour. Mode coupling in the nonlinear response of black holes. *Phys. Rev. D*, 68:084014, 2003.

[94] G. Allen, K. Camarda, and E. Seidel. Evolution of distorted black holes: A perturbative approach. 1998.

[95] Nils Andersson. Excitation of Schwarzschild black-hole quasinormal modes. *Phys. Rev. D*, 51:353, 1995.

[96] Ernst Nils Dorband and Manuel Tiglio. in preparation, 2006.

[97] Jeffrey Winicour. Characteristic evolution and matching. *Living Rev. Relativity*, 1:5, 1998. [Online article].

[98] Peter Hübner. From now to timelike infinity on a finite grid. *Class. Quantum Grav.*, 18:1871–1884, 2001.

[99] T. Regge and J. Wheeler. Stability of a Schwarzschild singularity. *Phys. Rev.*, 108(4):1063–1069, 1957.

[100] F. J. Zerilli. Effective potential for even-parity Regge-Wheeler gravitational perturbation equations. *Phys. Rev. Lett.*, 24(13):737–738, 1970.

[101] Andrew Abrahams and C. Evans. Reading off gravitational radiation waveforms in numerical relativity calculations: Matching to linearised gravity. *Phys. Rev. D*, 37:318–332, 1988.

[102] Andrew Abrahams. Analytic-numerical matching for gravitational waveform extraction. In C. Evans, L. Finn, and D. Hobill, editors, *Frontiers in Numerical Relativity*. Cambridge University Press, Cambridge, England, 1989.

[103] Andrew Abrahams and C. Evans. Gauge invariant treatment of gravitational radiation near the source: Analysis and numerical simulations. *Phys. Rev. D*, 42:2585–2594, 1990.

[104] A. Abrahams, D. Bernstein, D. Hobill, E. Seidel, and L. Smarr. Numerically generated black hole spacetimes: Interaction with gravitational waves. *Phys. Rev. D*, 45:3544–3558, 1992.

[105] Alessandro Nagar and Luciano Rezzolla. Gauge-invariant non-spherical metric perturbations of schwarzschild black-hole spacetimes. *Class. Quantum Grav.*, 22:R167, 2005.

[106] K. Camarda and E. Seidel. Numerical evolution of dynamic 3D black holes: Extracting waves. *Phys. Rev. D*, 57:R3204, 1998.

[107] K. Camarda and E. Seidel. Three-dimensional simulations of distorted black holes: Comparison with axisymmetric results. *Phys. Rev. D*, 59:064019, 1999.

[108] S. Brandt, J. A. Font, J. M. Ibáñez, Joan Massó, and E. Seidel. Numerical evolution of matter in dynamical axisymmetric black hole spacetimes. I. method and tests. *Comp. Phys. Comm.*, 124:169–196, 2000.

[109] Miguel Alcubierre, G. Allen, B. Brügmann, G. Lanfermann, E. Seidel, W.-M. Suen, and M. Tobias. Gravitational collapse of gravitational waves in 3D numerical relativity. *Phys. Rev. D*, 61:041501 (R), 2000.

[110] J. Baker, S. R. Brandt, M. Campanelli, C. O. Lousto, E. Seidel, and R. Takahashi. Nonlinear and perturbative evolution of distorted black holes: Odd-parity modes. *Phys. Rev. D*, 62:127701, 2000. gr-qc/9911017.

[111] Miguel Alcubierre, Bernd Brügmann, Denis Pollney, Edward Seidel, and Ryoji Takahashi. Black hole excision for dynamic black holes. *Phys. Rev. D*, 64:061501(R), 2001.

[112] Miguel Alcubierre, Bernd Brügmann, Peter Diener, Frank Herrmann, Denis Pollney, Edward Seidel, and Ryoji Takahashi. Testing excision techniques for dynamical 3D black hole evolutions. 2004.

[113] Frank Herrmann, Deirdre Shoemaker, and Pablo Laguna. Unequal-mass binary black hole inspirals. 2006.

[114] M. Shibata and K. Uryū. Gravitational waves from the merger of binary neutron stars in a fully general relativistic simulation. *Prog. Theor. Phys.*, 107:265, 2002.

[115] Masaru Shibata and Yu-ichirou Sekiguchi. Three-dimensional simulations of stellar core collapse in full general relativity: Nonaxisymmetric dynamical instabilities. *Phys. Rev. D*, 71:024014, 2005.

[116] Matthew D. Duez, Stuart L. Shapiro, and Hwei-Jang Yo. Relativistic hydrodynamic evolutions with black hole excision. *Phys. Rev. D*, 69:104016, 2004.

[117] Alessandra Buonanno, Gregory B. Cook, and Frans Pretorius. Inspiral, merger and ring-down of equal mass black-holes binaries. 2006.

[118] Bernd Brügmann et al. Calibration of moving puncture simulations. 2006.

[119] Manuela Campanelli, Bernard J. Kelly, and Carlos O. Lousto. The Lazarus project II: Space-like extraction with the quasi-Kinnersley tetrad. *Phys. Rev. D*, 73:064005, 2006.

[120] John Baker, Manuela Campanelli, and Carlos O. Lousto. The Lazarus project: A pragmatic approach to binary black hole evolutions. *Phys. Rev. D*, 65:044001, 2002.

[121] Y. Zlochower, J. G. Baker, M. Campanelli, and C. O. Lousto. Accurate black hole evolutions by fourth-order numerical relativity. *Phys. Rev. D*, 72:024021, 2005.

[122] David R. Fiske, John G. Baker, James R. van Meter, Dae-Il Choi, and Joan M. Centrella. Wave zone extraction of gravitational radiation in three-dimensional numerical relativity. *Phys. Rev. D*, 71:104036, 2005. gr-qc/0503100.

[123] Helmut Friedrich. Hyperbolic reductions for Einstein's equations. *Class. Quantum Grav.*, 13:1451–1469, 1996.

[124] M. Campanelli and C. O. Lousto. Second order gauge invariant gravitational perturbations of a Kerr black hole. *Phys. Rev. D*, 59:124022, 1999.

[125] Christopher Beetle, Marco Bruni, Lior M. Burko, and Andrea Nerozzi. Towards wave extraction in numerical relativity: Foundations and initial-value formulation. *Phys. Rev. D*, 72:024013, 2005.

[126] Andrea Nerozzi, Christopher Beetle, Marco Bruni, Lior M. Burko, and Denis Pollney. Towards wave extraction in numerical relativity: The quasi-Kinnersley frame. *Phys. Rev. D*, 72:024014, 2005.

[127] Lior M. Burko, Thomas W. Baumgarte, and Christopher Beetle. Towards a novel wave–extraction method for numerical relativity: III. analytical examples for the Beetle–Burko radiation scalar. *Phys. Rev. D*, 73:024002, 2006.

[128] Olivier Sarbach and Manuel Tiglio. Gauge invariant perturbations of Schwarzschild black holes in horizon-penetrating coordinates. *Phys. Rev. D*, 64:084016, 2001.

[129] U. Gerlach and U. Sengupta. Gauge-invariant perturbations on most general spherically symmetric space-times. *Phys. Rev. D.*, 19:2268–2272, 1979.

[130] Karl Martel and Eric Poisson. Gravitational perturbations of the schwarzschild spacetime: A practical covariant and gauge-invariant formalism. *Phys. Rev. D*, 71:104003, 2005.

[131] Enrique Pazos, Ernst Nils Dorband, Alessandro Nagar, Carlos Palenzuela, Erik Schnetter, and Manuel Tiglio. How far away is far enough for extracting numerical waveforms, and how much do they depend on the extraction method? gr-qc/0612149, 2006.

[132] David Garfinkle. Harmonic coordinate method for simulating generic singularities. *Phys. Rev. D*, 65:044029, 2002.

[133] B. Szilágyi, B. Schmidt, and Jeffrey Winicour. Boundary conditions in linearized harmonic gravity. *Phys. Rev. D*, 65:064015, 2002.

[134] B. Szilágyi and Jeffrey Winicour. Well-posed initial-boundary evolution in general relativity. *Phys. Rev. D*, 68:041501, 2003.

[135] Maria C. Babiuc, Béla Szilágyi, and Jeffrey Winicour. Testing numerical relativity with the shifted gauge wave. *Class. Quantum Grav.*, 23:S319–S342, 2006.

[136] H. Friedrich. On the hyperbolicity of Einstein's and other gauge field equations. *Comm. Math. Phys.*, 100:525–543, 1985.

[137] Frans Pretorius. Evolution of binary black hole spacetimes. *Phys. Rev. Lett.*, 95:121101, 2005.

[138] Carsten Gundlach, Jose M. Martin-Garcia, G. Calabrese, and I. Hinder. Constraint damping in the Z4 formulation and harmonic gauge. *Class. Quantum Grav.*, 22:3767–3774, 2005.

[139] O. Brodbeck, S. Frittelli, P. Hübner, and O. A. Reula. Einstein's equations with asymptotically stable constraint propogation. *J. Math. Phys.*, 40:909–923, 1999.

[140] Lee Lindblom, Mark A. Scheel, Lawrence E. Kidder, Robert Owen, and Oliver Rinne. A new generalized harmonic evolution system. *Class. Quantum Grav.*, 23:S447–S462, 2006.

[141] Helmut Friedrich. On the non-linearity of the subsidiary systems. *Class. Quant. Grav.*, 22:L77, 2005.

[142] O. Sarbach and M. Tiglio. Boundary conditions for Einstein's field equations: analytical and numerical analysis. *Journal of Hyperbolic Differential Equations*, 2:839–883, 2005.

[143] C. Bona, T. Ledvinka, C. Palenzuela-Luque, and M. Zacek. Constraint-preserving boundary conditions in the Z4 numerical relativity formalism. *Class. Quantum Grav.*, 22:2615–2634, 2005.

[144] G. Calabrese, J. Pullin, O. Reula, O. Sarbach, and M. Tiglio. Well posed constraint-preserving boundary conditions for the linearized Einstein equations. *Communications in Mathematical Physics*, 240:377–395, 2003.

[145] G. Calabrese, L. Lehner, and M. Tiglio. Constraint-preserving boundary conditions in numerical relativity. *Phys. Rev. D*, 65:104031, 2002.

[146] Maria C. Babiuc and J.Winicour. Constraint-preserving sommerfeld conditions for the harmonic einstein equations. *submitted to Phys. Rev. D*, 2006.

[147] Bertil Gustafsson. On the convergence rate for difference approximations to mixed initial boundary value problems. Technical Report 33, Department of Computer Science, Uppsala University, May 1971.

[148] Miguel Alcubierre, W. Benger, B. Brügmann, G. Lanfermann, L. Nerger, E. Seidel, and R. Takahashi. 3D Grazing Collision of Two Black Holes. *Phys. Rev. Lett.*, 87:271103, 2001.

[149] S. Brandt and E. Seidel. Evolution of distorted rotating black holes II: Dynamics and analysis. *Phys. Rev. D*, 52(2):870–886, 1995.

[150] Ernst Nils Dorband, Emanuele Berti, Peter Diener, Erik Schnetter, and Manuel Tiglio. A numerical study of the quasinormal mode excitation of Kerr black holes. *Phys. Rev. D*, 74:084028, 2006.

[151] John G. Baker, Joan Centrella, Dae-Il Choi, Michael Koppitz, and James van Meter. Gravitational wave extraction from an inspiraling configuration of merging black holes. *Phys. Rev. Lett.*, 96:111102, 2006.

[152] John G. Baker, Joan Centrella, Dae-Il Choi, Michael Koppitz, and James van Meter. Binary black hole merger dynamics and waveforms. *Phys. Rev. D*, 73:104002, 2006.

[153] Frans Pretorius. Simulation of binary black hole spacetimes with a harmonic evolution scheme. *Class. Quantum Grav.*, 23:S529–S552, 2006.

[154] Ulrich Sperhake. Binary black-hole evolutions of excision and puncture data. 2006.

[155] Jośe A. González, Ulrich Sperhake, Bernd Brügmann, Mark Hannam, and Sascha Husa. Total recoil: the maximum kick from nonspinning black-hole binary inspiral. 2006. gr-qc/0610154.

[156] Heinz Otto Kreiss and J. Lorenz. *Initial-Boundary Value Problems and the Navier-Stokes Equations*. Academic Press, New York, 1989.

[157] Richard Arnowitt, Stanley Deser, and Charles W. Misner. The dynamics of general relativity. In L. Witten, editor, *Gravitation: An introduction to current research*, pages 227–265. John Wiley, New York, 1962.

[158] James W. York. Kinematics and dynamics of general relativity. In Larry L. Smarr, editor, *Sources of gravitational radiation*, pages 83–126. Cambridge University Press, Cambridge, UK, 1979.

[159] Robert M. Wald. *General relativity*. The University of Chicago Press, Chicago, 1984.

[160] G. Calabrese, J. Pullin, O. Sarbach, and M. Tiglio. Convergence and stability in numerical relativity. *Phys. Rev. D*, 66:041501, 2002.

[161] Thomas W. Baumgarte and Stuart L. Shapiro. Numerical relativity and compact binaries. *Physics Reports*, 376(2):41–131, March 2003.

[162] Horst Beyer and Olivier Sarbach. On the well posedness of the Baumgarte-Shapiro- Shibata-Nakamura formulation of Einstein's field equations. *Phys. Rev. D*, 70:104004, 2004.

Appendix A Energy Method

This appendix sketches out how – in the continuum – well posedness of first order linear symmetric hyperbolic systems of partial differential equations (PDEs) are analyzed using the energy method and how boundary conditions are constructed in a stable manner. Details can be found for example in [48] and [156]. Equations of the form

$$\partial_t u^\alpha = A^{i\alpha}{}_\beta \partial_i u^\beta + B^\alpha{}_\beta u^\beta + C^\alpha \tag{138}$$

are studied, where $u^\alpha = u^\alpha(\mathbf{x}, t)$ is the state vector and Greek indices label evolution variables while Latin indices correspond to the spatial coordinates. A, B and C are functions of u^α but not it's derivatives. A system like this is called quasi linear, since it is linear in the first derivatives. Virtually all of the basic mathematical properties regarding well posedness of a system like this are encoded in the principal part, i.e. the first term on the right hand side of the previous equation. The lower order terms function as source terms and can be ignored in the following discussion.

To analyze hyperbolicity, one picks an arbitrary unit normal vector n_i, $n_j n^j = 1$ and project the partial derivatives onto that vector. The principal part of Eq. (138) becomes

$$\partial_t u^\alpha = A^{n\alpha}{}_\beta \partial_n u^\beta \tag{139}$$

where one uses the notation $\partial_n \equiv n^i \partial_i$ and $A^{n\alpha}{}_\beta \equiv A^{i\alpha}{}_\beta n_i$. The same notation will be used for all vectors and matrices that are projected onto n_i.

If for any unit normal vector n_i the eigenvalues of $A^{n\alpha}{}_\beta$ are real and if $A^{n\alpha}{}_\beta$ is symmetric, Eq. (138) is called symmetric hyperbolic. Symmetric hyperbolic systems are convenient for numerical methods because they are known to be well posed. Further, the numerical approach described in this thesis makes use of symmetric hyperbolicity to construct multi-block schemes of arbitrary high order that are guaranteed to be numerically stable. Well

posedness, roughly speaking means the solutions at any time depend continuously on the initial data. A consequence of well posedness is that norms of the solution $||u||$ grow in a way that is bounded, with the same bound for all initial data. This obviously does not guarantee long term stability, but it is quite obvious that it is a necessary condition for a convergent numerical method.

The stability of the system of equations written down in Eq. (138) is not only determined by it's principal part – it was already mentioned that a symmetric hyperbolic system is convenient – but also by the boundary conditions. The importance of the boundary conditions is not surprising, since through them energy can dissipate out of or be injected into the domain of the solution.

For constructing boundary conditions, the so called characteristic modes play a crucial role. Following is a brief description of the construction of these modes how they enter the stability analysis of partial differential equations.

One looks for a way to express Eq. (139) in terms of variables $v = v(u)$ for which (139) takes the form of k of decoupled advection equations, where k is the number of primary variables u. The principal part of the transformed PDEs would be diagonal, and each diagonal element a real number, either positive, negative or zero, corresponding to characteristic modes propagating in the direction or the opposite direction of n_i, and orthogonal to n_i, respectively.

A transformation like that can always be found for symmetric hyperbolic systems of equations. Let Λ be the diagonalizer for A^n. For readability indices of A^n are suppressed. One multiplies Λ and its inverse into Eq. (139) in strategic places to get

$$\partial_t(\Lambda^{-1}u) = \Lambda^{-1}A^n\Lambda\partial_n(\Lambda^{-1}u) \tag{140}$$

$$\partial_t v = \hat{A}^n\partial_n v. \tag{141}$$

The assumption that Λ does not explicitly depend on the coordinates and on time is used and one introduces the definitions $v \equiv \Lambda^{-1}u$ and $\hat{A}^n \equiv \Lambda^{-1}A^n\Lambda$. $\hat{A}^n$ is diagonal and the diagonal elements are the eigenvalues of A^n. The diagonalizer is a matrix constructed from the eigen-vectors $e_\alpha^{(\kappa)}$ of A^n. The upper index (κ) labels the κ-th eigen-vector, α labels each vectors components. The diagonalizer is given explicitly as $\Lambda^\kappa{}_\alpha = \left(e_\alpha^{(\kappa)}\right)$.

It was described how to write a symmetric hyperbolic system in terms of its characteristic variables. Now it will be shown how boundary conditions are applied to these variables at the continuum in a way that makes the system well posed and stable.

The following description is only a sketch of some ideas and methods and is in no sense a complete discussion. More details can be found in [48] and [156]. For simplicity from here on only a one dimensional system of equations is discussed and the spatial domain is chosen to be $0 \leq x \leq 1$. One considers the principal part of the same first order evolution system as above for fields $u = (u^1...u^m)$ and in the one dimensional case it is written as

$$\partial_t u = A\partial_x u, \tag{142}$$

where A is a matrix with $m \times m$ entries. For readability indices running over the field variables u^α are suppressed.

As shown above, one can diagonalize the system using a matrix Λ, composed of the eigen-vectors of A to get

$$\Lambda^{-1}A\Lambda = \hat{A} = \begin{pmatrix} \hat{A}^I & 0 & 0 \\ 0 & \hat{A}^{II} & 0 \\ 0 & 0 & \hat{A}^{III} \end{pmatrix} \tag{143}$$

with $\hat{A}^I = \text{diag}\,(\lambda_1, ..., \lambda_r)$, $\hat{A}^{II} = \text{diag}\,(\lambda_{r+1}, ..., \lambda_{m-s})$ and $\hat{A}^{III} = 0$. λ_i are the eigenvalues or characteristic speeds of A and are numbered in a way that $\lambda_i > 0$ for $i = 1, ..., r$, $\lambda_i < 0$ for $i = r+1, ..., m-s$ and $\lambda_i = 0$ for $i > m-s$.

The characteristic fields are

$$v = \Lambda^{-1} u \tag{144}$$

and the evolution system in terms of these fields is a system of m decoupled equations

$$\partial_t v = \hat{A} \partial_x v. \tag{145}$$

To understand how one has to apply boundary conditions to the characteristic variables, one groups these evolution equations into a part with modes that have positive speed, one with negative speed modes and in one that describes the zero speed modes.

$$\partial_t v^I = \hat{A}^I \partial_x v^I \tag{146}$$

$$\partial_t v^{II} = \hat{A}^{II} \partial_x v^{II} \tag{147}$$

$$\partial_t v^{III} = 0. \tag{148}$$

Fig. A gives an intuitive geometric picture of how to apply boundary conditions to the characteristic variables. v^I represents the modes with a negative characteristic speed, v^{II} the ones with a positive speed. Zero speed modes can be left out of the discussion since they do not cross the boundaries. At the lower boundary $x = 0$ v^I is outgoing and no boundary condition needs to be applied to it. v^{II} is ingoing and can in principle be specified arbitrarily. For example if it is known that in the physics that is modeled there exists no incoming radiation, all v^{II} would be set to zero. If an analytic solution at the boundary is known it can be imposed through the incoming modes. Another widely used option is to choose them in a way that freezes the time derivative of the incoming mode. That will keep the boundary points at the value they are given in by the initial data. The analog situation with v^I and v^{II} interchanged is found at the upper boundary $x = 1$.

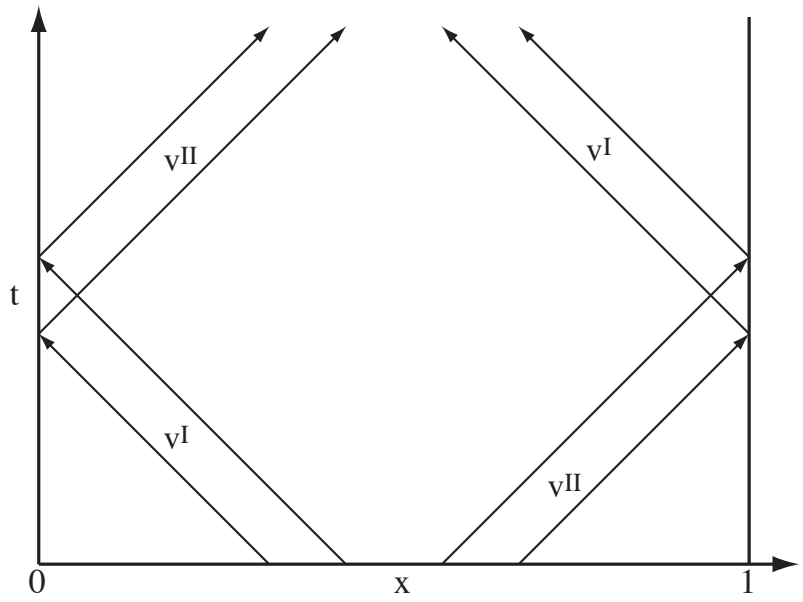

Figure 29: Geometric interpretation of the characteristic modes. v^I represents the modes with a negative characteristic speed, v^{II} the ones with a positive speed. Zero speed modes do not play a role in this picture. At the lower boundary $x = 0$ v^I is outgoing and no boundary condition needs to be applied to it. v^{II} is ingoing and can in principle be specified arbitrarily. For example if it is known that in the physics that is modeled there exists no incoming radiation, all v^{II} would be set to zero. The same situation with v^I and v^{II} interchanged is found at the upper boundary $x = 1$.

Following is a discussion about the stability for the characteristic evolution system of Eq. (148). For that one needs to define a L_2 scalar product of two fields and norm as

$$\langle v, w \rangle \equiv \int_\Omega \bar{v} w d\Omega \tag{149}$$

$$||v|| = \langle v, v \rangle^{1/2} = \left(\int_\Omega |v|^2 d\Omega \right)^{1/2} \tag{150}$$

where $\bar{v}$ is the complex conjugate of v and the integration is done over the whole domain Ω. One also needs an Euclidian scalar product and norm for finite dimensional vector spaces. In an m-dimensional vector space consisting of all $u = (u^1, ..., u^m)^T$ the scalar product and norm is defined by

$$(u, v) = \sum_{j=1}^{m} \bar{u}^j v^j \tag{151}$$

$$|u| = (u, u)^{1/2}. \tag{152}$$

Two useful properties of these norms are

$$\langle u, A v_x \rangle = - \langle u_x, A v \rangle - \langle u, A_x v \rangle + [(u, Av)]_0^1 \tag{153}$$

and

$$|\langle u, Av \rangle| \leq ||A||_\infty \, ||u|| \, ||v||. \tag{154}$$

It is used that $||A||_\infty = \sup_x |A|$. Eq. (153) simply is the integration by parts rule, Eq. (154) follows from the definition of the scalar product.

The idea of proving stability with the energy method is to define an energy norm $\mathcal{E} =< u, \sigma u >$ and compute its time derivative. One can then see if the energy growth is bounded and how boundary conditions have to be chosen to gain stability. Finding a good energy norm is specific to the evolution system and since here it is just sketched

briefly how this mechanism works, only the simple case of $\sigma = I$ is discussed, I being the unit matrix.

The time derivative of the energy norm is

$$\begin{aligned}
\dot{\mathcal{E}} = ||v||_t^2 &= \langle v_t, v\rangle + \langle v, v_t\rangle \\
&= \left\langle \hat{A}v_x, v\right\rangle + \left\langle v, \hat{A}v_x\right\rangle \\
&= -\left\langle v, \hat{A}_x v\right\rangle + \left[\left(v, \hat{A}v\right)\right]_0^1 \\
&\leq ||\hat{A}||_\infty \, ||v||^2 + \left[\left(v, \hat{A}v\right)\right]_0^1 . \qquad (155)
\end{aligned}$$

Eq. (153) has been used to get from the second to the third line, and Eq. (154) to find the final inequality. The role of the boundary conditions for stability is clear form the expression above. To study boundary effects, one expresses the boundary conditions on the incoming modes in terms of the outgoing ones:

$$\begin{aligned}
v^{II}(0,t) &= R^I(t) v^I(0,t) \qquad (156) \\
v^I(1,t) &= R^{II}(t) v^{II}(1,t). \qquad (157)
\end{aligned}$$

$R^I(t)$ and $R^{II}(t)$ are arbitrary functions of t. With these boundary conditions, the minuend and subtrahend encoded in the last term of equation (155) become respectively

$$\begin{aligned}
\left(v(1,t), \hat{A}(1,t)v(1,t)\right) &= \left(v^I(1,t), \hat{A}^I(1,t)v^I(1,t)\right) + \\
&\quad \left(v^{II}(1,t), \hat{A}^{II}(1,t)v^{II}(1,t)\right) \\
&= \left(v^{II}(1,t), C^{II}(1,t)v^{II}(1,t)\right) \\
\left(v(0,t), \hat{A}(0,t)v(0,t)\right) &= \left(v^I(0,t), C^I(0,t)v^I(0,t)\right) \qquad (158)
\end{aligned}$$

where

$$C^{II}(1,t) = \hat{A}^{II}(1,t) + \bar{R}^{II}(t)\hat{A}^{I}(1,t)R^{II}(t) \quad (159)$$

$$C^{I}(0,t) = \hat{A}^{I}(0,t) + \bar{R}^{I}(t)\hat{A}^{II}(0,t)R^{I}(t). \quad (160)$$

Now, if possible R^I and R^{II} are chosen suitably small so that $\dot{\mathcal{E}} \leq 0$ to get a bounded energy norm and therefore a globally stable evolution system. These boundary conditions are called maximally dissipative.

Appendix B Notes on Comparing Numerical Results from Chap. 4 with the Semi-Analytic Predictions

To compare the numerical results with predictions from perturbation theory a switch from the usual Boyer-Linquist coordinates (as used, for example, in [83]) to the Kerr-Schild coordinates used in the code has to be done. Let $(r_*,\, t)$ denote the Boyer-Lindquist radial tortoise coordinate and time, and $(\bar{r},\, \bar{t})$ the Kerr-Schild coordinates. The transformation needed is given by

$$t(\bar{t}, \bar{r}) = \bar{t} - \Omega(\bar{r}) + \tilde{t}\,, \tag{161}$$

$$r_*(\bar{r}) = \bar{r} + \Omega(\bar{r})\,, \tag{162}$$

with the definitions

$$\Omega(r) = \frac{2Mr_+}{r_+ - r_-} \ln\left(\frac{r - r_+}{2M}\right) - \frac{2Mr_-}{r_+ - r_-} \ln\left(\frac{r - r_-}{2M}\right)\,, \tag{163}$$

$$r_+ = M + \sqrt{M^2 - a^2}\,, \tag{164}$$

$$r_- = M - \sqrt{M^2 - a^2}\,. \tag{165}$$

$$\tag{166}$$

The reference time $\tilde{t}$ can in principle be freely chosen and is used to define where $t(\bar{r}, \bar{t})$ crosses zero. It is fixed here by the condition that in both coordinate systems the initial pulse is at the same physical distance from the black hole, i.e. $t(\bar{t} = 0, \bar{r} = \bar{r}_0) = 0$:

$$\tilde{t} = \Omega(\bar{r}_0)\,. \tag{167}$$

The location of the initial pulse in these coordinates becomes

$$r_0 = \bar{r}_0 + \Omega(\bar{r}_0). \tag{168}$$

For consistency, the value of σ has to be adjusted to tortoise coordinates. As a rough approximation

$$\sigma = \frac{1}{2}\left[r_*(\bar{r}+\bar{\sigma}) - r_*(\bar{r}-\bar{\sigma})\right] \tag{169}$$

is set.

From Eq. 72 and 82 one reads of the exponential decay of each modes amplitude in Boyer-Lindquist coordinates and then substitute them by the Kerr-Schild coordinates. $t_0 = r_* + r_0$ is chosen.

$$\mathcal{A}_{\ell mn} e^{t-r_*-r_0} = \mathcal{A}_{\ell mn} e^{-2\Omega(\bar{r})\mathcal{I}(\omega_{lmn})} e^{\bar{t}-\bar{r}-\bar{r}_0} \equiv \bar{\mathcal{A}}_{\ell mn} e^{\bar{t}-\bar{r}-\bar{r}_0} \tag{170}$$

This equation relates the amplitudes as seen in Boyer-Lindquist coordinates $\mathcal{A}_{\ell mn}$ with the ones found in the simulations that were done in Kerr-Schild coordinates $\bar{\mathcal{A}}_{\ell mn}$.

Appendix C 3+1 Split

The Einstein equations describe the dynamics of space-time in the form of four dimensional second order covariant partial differential equations for a metric $g_{\mu\nu}$ which quantifies the infinitesimal distance of points on a manifold $\mathcal{M}$. The effect of matter or fields (for example electro-magnetic fields) can be taken into account by coupling the space-time equations to the so-called stress energy tensor which again incorporates the equation of state for the matter or fields. The concern here are vacuum space-times and any discussion involving stress energy tensors is left out.

A commonly used and very intuitive way to solve the Einstein equations numerically is the Cauchy approach, which is often referred to as the $3+1$ split and was first formulated by Arnowitt, Deser and Misner in 1962 [157] in an attempt to quantize gravity. The space-time equations are described as an initial value problem. The initial data are set on a three dimensional purely space like hypersurface and have to satisfy four elliptic partial differential equations, namely the scalar Hamiltonian constraint $\mathcal{H}$ and the vector momentum constraint $\mathcal{M}^i$, $i = 1, 2, 3$. Initial data, given everywhere on the three dimensional hypersurface, fully determine the metric on all other space-like slices and therefore the whole four dimensional space-time. The different slices are connected via a set of hyperbolic equations, the evolution equations, that tell how the intrinsic quantities of each slice evolve along a time like vector.

In this chapter a more precise description of how this mechanism works is given and the involved equations are given in a very basic form, the so called Arnowitt, Deser, Misner (ADM) formulation [157]. Here the very detailed treatment of the 3+1 split given by York [158] is followed loosely.

The full four dimensional space-time $(\mathcal{M}, g_{\mu\nu})$ is foliated into three dimensional space like hypersurfaces Σ labeled by a number t. t can be interpreted as a time coordinate and each of the slices represents the space-time at a constant time. On each point of

each of the hypersurfaces a normal vector $\bar{n}^\mu$ can be defined, which is time like and in the convention used here points in the future direction.

For a given foliation Σ a complete description of the space-time $(\mathcal{M}, g_{\mu\nu})$ can be given by three dimensional tensor quantities intrinsic to the space like slices. These are the three metric γ_{ij} that defines the geometry on each hypersurface and the so called extrinsic curvature K_{ij} that describes the embedding of the three dimensional manifolds in the four dimensional one.

These tensors are constructed using a projection operator $h_{\mu\nu}$ which is defined as

$$h_{\mu\nu} \equiv g_{\mu\nu} - \bar{n}_\mu \bar{n}_\nu. \tag{171}$$

It is symmetric in its two indices, purely space like $h_{\mu\nu} n^\mu = 0$ and has the desired property to project all four dimensional geometric objects into the hypersurface. This can be seen easily by projecting $h_{\mu\nu}$ on $\bar{n}^\mu$:

$$\begin{aligned} \bar{n}^\mu \bar{n}_\nu h^\nu{}_\sigma &= \bar{n}^\mu \bar{n}_\nu g^\nu{}_\sigma - \bar{n}^\mu \bar{n}_\nu \bar{n}^\nu \bar{n}_\sigma \\ &= \bar{n}^\mu \bar{n}_\sigma - \bar{n}^\mu \bar{n}_\sigma = 0. \end{aligned}$$

The three metric simply is the projection of the four metric

$$\gamma_{ij} = h^\mu{}_i h^\nu{}_j g_{\mu\nu} \tag{172}$$

where as usual Latin indices label space like coordinates x^1, x^2 and x^3. The inverse of the three metric is defined through $\gamma^{ij}\gamma_{jk} = \delta^i{}_k$ and the three metric is used to raise and lower indices of three dimensional vectors and tensors on the three manifold.

Since the normal vector $\bar{n}^\mu$ is defined on all points in the four dimensional space-time it fully determines the embedding of the slicing. The shape or the extrinsic curvature of a surface in a higher dimensional space is described by the infinitesimal change of between

the normal vectors on two neighboring points on the manifold. This can be expressed in a covariant, i.e. coordinate independent way by the covariant derivative $\nabla_\nu \bar{n}^\mu$ which again can be projected into the hypersurfaces to get the definition of the extrinsic curvature tensor

$$K_{ij} \equiv h^\mu{}_i h^\nu{}_j \nabla_\nu \bar{n}_\mu. \tag{173}$$

The extrinsic curvature can be rewritten as

$$K_{ij} = -\frac{1}{2}\mathcal{L}_{\bar{n}} \gamma_{ij}, \tag{174}$$

where $\mathcal{L}_{\bar{n}}$ is the Lie derivative with respect to the normal vector $\bar{n}^\mu$. This relation suggests to interpret K_{ij} as a generalized time derivative or momentum of the three metric and in fact in many formulations the evolution equation for the three metric is a direct result of Eq. (174). Also in analogy to classical mechanical systems that are determined by specifying for example positions and momenta of particles at an initial time t_0, it intuitively makes sense that on an initial slice, the metric and the curvature has to be specified.

Until now a given foliation Σ of space-time was assumed. The actual choice of a foliation does not change the physical content of the space-time but rather corresponds to the coordinate freedom present in general relativity. Constructing a good slicing is of crucial importance to numerical simulations. The construction is done by introducing a time direction $t^\mu = \partial_t$ and its projections on the hypersurface and the normal vector:

$$\beta^\mu = h^\mu{}_\nu t^\nu \tag{175}$$

$$\alpha = \bar{n}_\mu t^\mu. \tag{176}$$

t^μ expressed in terms of these projections is

$$t^\mu = \alpha \bar{n}^\mu + \beta^\mu. \tag{177}$$

Fig. 30 illustrates the geometrical meaning of these quantities. α, usually called lapse function or simply lapse carries the information about the proper distance between neighboring slices, β^μ, the shift vector, encodes how coordinate points move when going from one slice to the next in time. It has to be stressed again, that lapse and shift are pure gauge functions that specify a coordinate system and can be chosen freely. Since $\beta^\mu \bar{n}_\mu = 0$, it is usually expressed as a three dimensional vector β^i.

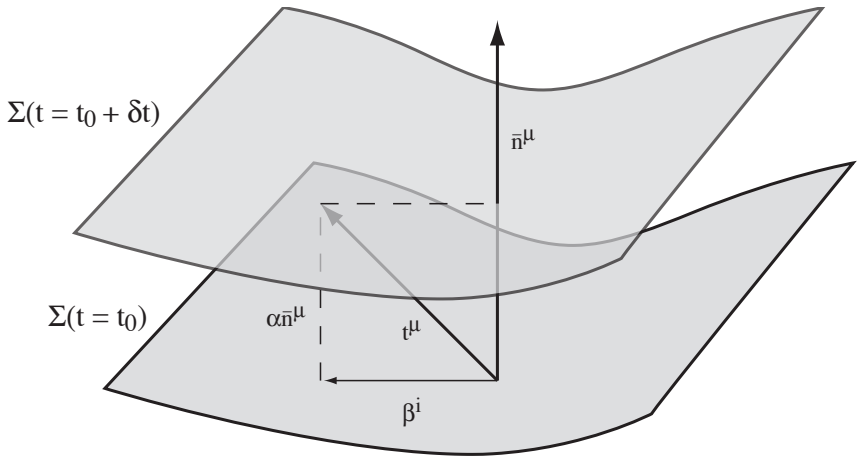

Figure 30: Illustration of the quantities involved in the 3+1 split of a space-time. Shown are two slices at consecutive times t_0 and $t_0 + \delta t$. The lapse α measures the distance between the two slices along the normal $\bar{n}^\mu$. The shift β^i is space like and moves coordinate points within a hyper surface. Also shown is the time direction t^μ.

The gauge functions α and β^i together with the three metric g_{ij} and the extrinsic curvature K_{ij} are often called $3+1$ quantities. The full four dimensional metric expressed

in terms of these quantities is

$$ds^2 = -(\alpha dt)^2 + \gamma_{ij}(dx^i + \beta^i dt)(dx^j + \beta^j dt) \tag{178}$$

where the notation $dt \equiv dx^0$ is used.

The three metric γ_{ij} determines a natural covariant derivative operator on Σ that is called ${}^{(3)}\nabla_i$ and that is metric compatible, i.e. ${}^{(3)}\nabla_i g_{jk} = 0$. Furthermore three dimensional Christoffel symbols ${}^{(3)}\Gamma^i_{jk}$ and a curvature tensor ${}^{(3)}R_{ijk}{}^l$ can be constructed on Σ, by applying the usual definitions. One now needs to express ${}^{(3)}\nabla_i$ and ${}^{(3)}R_{ijk}{}^l$ in terms of the four dimensional quantities. This relations are the so called Gauss-Codazzi equations.

The covariant derivative operator ${}^{(3)}\nabla_i$ can be written as the projection of the four dimensional covariant derivative onto the three dimensional hypersurface:

$${}^{(3)}\nabla_i T^{\mu_1 \ldots \mu_k}{}_{\nu_1 \ldots \nu_l} = h^{\mu_1}{}_{\eta_1} \ldots h^{\mu_k}{}_{\eta_k} h_{\nu_1}{}^{\sigma_1} \ldots h_{\nu_l}{}^{\sigma_l} h_i{}^{\rho} \nabla_\rho T^{\eta_1 \ldots \eta_k}{}_{\sigma_1 \ldots \sigma_l} \tag{179}$$

It is straight forward to show that this derivative operator is indeed the covariant derivative compatible with the three metric (see for example [159]). For that the property

$${}^{(3)}\nabla_i h_{jk} = h^l{}_i h^m{}_j h^o{}_k \, {}^{(3)}\nabla_l (\gamma_{mo} - \bar{n}_m \bar{n}_o) = 0 \tag{180}$$

is used.

The curvature tensor on Σ is defined in the same way the curvature tensor of the four dimensional space-time is often introduced. If ω_i is a dual vector field on Σ, one defines

$${}^{(3)}R_{ijk}{}^l \omega_l = {}^{(3)}\nabla_i \, {}^{(3)}\nabla_j \omega_k - {}^{(3)}\nabla_j \, {}^{(3)}\nabla_i \omega_k. \tag{181}$$

The partial derivatives on the right hand side are replaced by Eq. (179) and the relation

$$h^j{}_i h^l{}_k \, {}^{(3)}\nabla_j h^m_l = K_{ik}\bar{n}^m \tag{182}$$

is used which follows directly from the definition of the extrinsic curvature (173). One then arrives at

$${}^{(3)}R_{\ ijk}{}^{l} = h_i{}^{\mu} h_j{}^{\nu} h_k{}^{\eta} h^l{}_{\rho} R_{\mu\nu\eta}{}^{\rho} - K_{ik}K_j{}^{l} + K_{jk}K_i{}^{l}. \tag{183}$$

In a similar manner starting from the left hand side doing similar substitutions one can derive the relation

$${}^{(3)}\nabla_j K^j{}_i - \ {}^{(3)}\nabla_i K^j{}_j = R_{\mu\nu}\bar{n}^{\nu} h^{\mu}{}_i. \tag{184}$$

Eq. (183) and (184) are the Gauss Codazzi relations mentioned above.

Inserting the Gauss Codazzi relations into the Einstein equations, a simple formulation of the latter in terms of the 3+1 quantities can be written down. These equations are the so called ADM equations. They are a set of 16 partial differential equations, four of elliptic type and 12 of hyperbolic type. They are explicitly given by

$$\mathcal{H} \equiv {}^{(3)}R + K^2 - K^{ij}K_{ij} = 0 \tag{185}$$

$$\mathcal{M}^i \equiv {}^{(3)}\nabla_j (K^{ij} - \gamma^{ij}K) = 0 \tag{186}$$

and

$$\frac{d}{dt}\gamma_{ij} = -2\alpha K_{ij} \tag{187}$$

$$\frac{d}{dt}K_{ij} = -\ {}^{(3)}\nabla_i \ {}^{(3)}\nabla_j \alpha + \alpha(\ {}^{(3)}R_{ij} + K K_{ij} - 2K_{ik}K^k_{\ j}). \tag{188}$$

The time derivative operators on the left hand sides of these equations are defined as

$$\frac{d}{dt} = \frac{\partial}{\partial t} - \mathcal{L}_{\beta}. \tag{189}$$

${}^{(3)}R$ is the scalar curvature constructed from the three metric γ_{ij}.

Eq. (185) and (186) do not contain second derivatives in time and therefore are not evolution equations. They are elliptic and can be treated as a boundary value problem on each three dimensional hyper surface. They impose constraints on the system, namely the hamiltonian constraint $\mathcal{H}$ and the momentum constraints $\mathcal{M}^i$. Using the contracted Bianchi identities it can be shown that if the constraints are satisfied on one time slice, the same will be the case for all times, i.e. on all other slices of the space-time. In numerical simulations due to discretization errors and their propagation properties, the constraints will be violated either at the initial time or after evolving for one time step. In many cases the constraint violation are used to measure the error that is done during the simulation. Even though there is no general rule telling how much accuracy is lost in the numerical data, when a certain level of constraint violation is present, generally the constraint violations will indicate how far the numerical solution is drifting away from physical solutions, i.e. solutions that satisfy the Einstein equations. The elliptic equations defining the constraints can also be solved at each time step to ensure that the constraints stay at zero. In that case one speaks about *constraint enforcement*.

Eq. (187) and (188) are the actual evolution equations for the three metric and the extrinsic curvature. They are in hyperbolic form. Because of the constraints, initial data cannot be chosen freely but they need to satisfy Eq. (185)–(186).

It has been explicitly shown in [160] that the ADM formulation is not stable for numerical evolutions. The reason is that the evolution equations are only weakly hyperbolic. The instability of the ADM system was noted in countless simulations even before it was formally proved. This spawned a whole industry of reformulating the equations to make them suitable for stable numerical schemes. One of the more successful reformulations is the so called Baumgarte-Shapiro-Shibata-Nakamura (BSSN) system, a second order in space formulation of the Einstein equations [41, 42], and its advantages have been shown numerically first before attempts to analyze the equations themselves have been under-

taken (see [161] and references given there). In [162] the well posedness of the BSSN system is investigated. A different approach is to formulate the equations in the better understood first order form and modify it by adding constraints to the evolution equations in a way that the system is symmetric hyperbolic. The first order generalized harmonic system described in Chap. 5 is an example for that approach. Even though at this time it is not known what the best formulation is, it is understood well enough how to formulate the evolution equations to suppress instabilities so that they are no longer the limiting factor in numerical simulations.

Appendix D Vector and Tensor Harmonics

This appendix describes how vectors and tensors are expanded into spherical harmonics. In what follows the methodology is developed for vector fields and then generalized to the case of tensor fields. As in Chap. 5, capital Latin indices denote angular coordinates and objects with a hat (for example $\hat{\nabla}$) are two dimensional objects on S^2.

A vector field V_A defined on a manifold $\mathcal{S}^2$ can be decomposed into spherical harmonics using the expression

$$V_A = \sum_{\ell=1}^{\infty} \sum_{m=-\ell}^{+\ell} \alpha^{(\ell,m)} Y_A^{(\ell,m)} + \beta^{(\ell,m)} S_A^{(\ell,m)} \tag{190}$$

where $Y_A^{(\ell,m)}$ are the even and $S_A^{(\ell,m)}$ the odd parity basis vectors tangent to the manifold. The explicit form of the basis vectors is

$$Y_A^{(\ell,m)} = \hat{\nabla}_A Y^{(\ell,m)} \tag{191}$$

$$S_A^{(\ell,m)} = \hat{\epsilon}_A^B \hat{\nabla}_B Y^{(\ell,m)} \tag{192}$$

and called *vector spherical harmonics*. They satisfy the orthogonality relations

$$\int \hat{g}^{AB} \bar{Y}_A^{(\ell,m)} Y_B^{(\ell',m')} d\Omega = \ell(\ell+1)\delta_{ll'}\delta_{mm'} \tag{193}$$

$$\int \hat{g}^{AB} \bar{S}_A^{(\ell,m)} S_B^{(\ell',m')} d\Omega = \ell(\ell+1)\delta_{ll'}\delta_{mm'} \tag{194}$$

where the integration is done over the unit sphere and $d\Omega = \sin\theta d\theta d\phi$. From Eq. (190) and (194) the multipole modes are computed to

$$\alpha^{(\ell,m)} = \frac{1}{\ell(\ell+1)} \int \hat{g}^{AB} V_A \bar{Y}_B^{(\ell m)} d\Omega \tag{195}$$

$$\beta^{(\ell,m)} = \frac{1}{\ell(\ell+1)} \int \hat{g}^{AB} V_A \bar{S}_B^{(\ell m)} d\Omega. \tag{196}$$

The discussion about vector fields is completed by showing the explicit expression for the multi pole expansion in spherical coordinates. The components of the even vector spherical harmonics are $Y_\theta^{(\ell,m)} = \partial_\theta Y^{(\ell,m)}$ and $Y_\phi^{(\ell,m)} = \partial_\phi Y^{(\ell,m)}$. Accordingly for the odd sector one gets $S_\theta^{(\ell,m)} = -\sin^{-1}\theta \partial_\theta Y^{(\ell,m)}$ and $S_\phi^{(\ell,m)} = \sin\theta \partial_\phi Y^{(\ell,m)}$. Expanding in these components yields

$$\alpha^{(\ell,m)} = \frac{1}{\ell(\ell+1)} \int V_\theta \bar{Y}_\theta^{(\ell,m)} + \frac{1}{\sin^2\theta} V_\phi \bar{Y}_\phi^{(\ell,m)} d\Omega \tag{197}$$

$$\beta^{(\ell,m)} = \frac{1}{\ell(\ell+1)} \int \frac{1}{\sin\theta} \left(V_\phi \bar{Y}_\theta^{(\ell,m)} - V_\theta \bar{Y}_\phi^{(\ell,m)} \right) d\Omega. \tag{198}$$

One can now generalize the previous definitions to tensor fields. For simplicity of notation and because it is sufficient for the problems that are studied in this thesis, the discussion is restricted to tensors with two components. Let V_{AB} be a tensor on $\mathcal{S}^2$. The multipole decomposition into the tensor spherical harmonics $Y_{AB}^{(\ell,m)}$, $S_{AB}^{(\ell,m)}$ and the standard spherical harmonics $Y^{(\ell,m)}$ is written as

$$V_{AB} = \sum_{\ell=2}^{\infty} \sum_{m=-\ell}^{+\ell} \kappa^{(\ell,m)} \hat{g}_{AB} Y^{(\ell,m)} + \gamma^{(\ell,m)} Y_{AB}^{(\ell,m)} + \eta^{(\ell,m)} S_{AB}^{(\ell,m)}. \tag{199}$$

The first two terms in the sum of the previous expression is the even part of the expansion, the third term corresponds to the odd part. The tensor spherical harmonics are defined as

$$Y_{AB}^{(\ell,m)} = \hat{\nabla}_A \hat{\nabla}_B Y^{(\ell,m)} + \frac{1}{2}\ell(\ell+1)\hat{g}_{AB} Y^{(\ell,m)} \tag{200}$$

$$S_{AB}^{(\ell,m)} = \frac{1}{2}\left(\hat{\nabla}_A S_B^{(\ell,m)} + \hat{\nabla}_B S_A^{(\ell,m)} \right). \tag{201}$$

The orthogonality relations for these objects are

$$\int \hat{g}^{AC} \hat{g}^{BD} \bar{Y}_{CD}^{(\ell,m)} \bar{Y}_{AB}^{(\ell' m')} d\Omega = \frac{1}{2}\ell(\ell-1)(\ell+1)(\ell+2)\delta_{\ell\ell'}\delta_{mm'} \tag{202}$$

$$\int \hat{g}^{AC}\hat{g}^{BD}\bar{S}^{(\ell,m)}_{CD}\bar{S}^{(\ell'm')}_{AB}d\Omega = \frac{1}{2}\ell(\ell-1)(\ell+1)(\ell+2)\delta_{\ell\ell'}\delta_{mm'}. \quad (203)$$

As in the case of vector fields, one computes the multipole modes using the expansion in spherical harmonics together with the orthogonality relations and get

$$\kappa^{(\ell m)} = \frac{1}{2}\int V_{AB}g^{AB}\bar{Y}^{(\ell m)}d\Omega \quad (204)$$

$$\gamma^{(\ell m)} = \frac{2}{\ell(\ell-1)(\ell+1)(\ell+2)}\int \hat{g}^{AC}\hat{g}^{BD}V_{AB}\bar{Y}^{(\ell,m)}_{CD}d\Omega \quad (205)$$

$$\eta^{(\ell m)} = \frac{2}{\ell(\ell-1)(\ell+1)(\ell+2)}\int \hat{g}^{AC}\hat{g}^{BD}V_{AB}\bar{S}^{(\ell,m)}_{CD}d\Omega. \quad (206)$$

Finally again the expansion is given explicitly for the case of standard spherical coordinates. The components of the basis are

$$Y^{(\ell,m)}_{\theta\theta} = \frac{1}{2}W^{(\ell,m)} \quad (207)$$

$$Y^{(\ell,m)}_{\theta\phi} = \frac{1}{2}X^{(\ell,m)} \quad (208)$$

$$Y^{(\ell,m)}_{\phi\phi} = -\frac{1}{2}\sin^2\theta W^{(\ell,m)} \quad (209)$$

$$S^{(\ell,m)}_{\theta\theta} = -\frac{1}{2\sin\theta}X^{(\ell,m)} \quad (210)$$

$$S^{(\ell,m)}_{\theta\phi} = \frac{1}{2}\sin\theta W^{(\ell,m)} \quad (211)$$

$$S^{(\ell,m)}_{\phi\phi} = \frac{1}{2}\sin\theta X^{(\ell,m)}. \quad (212)$$

Here the definitions

$$W^{(\ell,m)} = 2\left[\partial^2_\theta + \frac{1}{2}\ell(\ell+1)\right]Y^{(\ell,m)} \quad (213)$$

$$X^{(\ell,m)} = 2\partial_\phi\left(\partial_\theta - \cot\theta\right)T^{(\ell,m)} \quad (214)$$

were used.

For the physical situations that are of interest in this thesis, it is safe to assume V_{AB} to be a symmetric tensor, namely the three metric or the extrinsic curvature. Introducing $L = \ell(\ell-1)(\ell+1)(\ell+2)$ one gets the multi pole components in the fairly simple form

$$\kappa^{(\ell,m)} = \frac{1}{2}\int \left(V_{\theta\theta} + \frac{V_{\phi\phi}}{\sin^2\theta}\right)\bar{Y}^{(\ell,m)}d\Omega \tag{215}$$

$$\gamma^{(\ell,m)} = \frac{1}{L}\int V_{\theta\theta}\bar{W}^{(\ell,m)} + \frac{1}{\sin^2\theta}\left(2V_{\theta\phi}\bar{X}^{(\ell,m)} - V_{\phi\phi}\bar{W}^{(\ell,m)}\right)d\Omega \tag{216}$$

$$\eta^{(\ell,m)} = \frac{1}{L}\int \frac{V_{\phi\phi}}{\sin^3\theta}\bar{X}^{(\ell,m)} + 2\frac{V_{\theta\phi}}{\sin\theta}\bar{W}^{(\ell,m)} - \frac{V_{\theta\theta}}{\sin\theta}\bar{X}^{(\ell,m)}d\Omega. \tag{217}$$

On the $\mathcal{S}^2$ manifold the $Y^{(\ell,m)}$ are normalized with respect to the two metric $\hat{g}_{AB}$ for all $\ell \geq 2$. For $\ell = 1$

$$\int Y^{(1,m)}\bar{Y}^{(1,m)}d\Omega = \frac{4\pi}{3} \tag{218}$$

and for $\ell = 0$

$$\int Y^{(0,0)}\bar{Y}^{(0,0)}d\Omega = 1 \tag{219}$$

is chosen.

Vita

Ernst Nils Dorband was born in Werneck, Germany, on January 27th, 1977, as the son of Monika and Immo Dorband. He did his undergraduate program at the Julius-Maximilians Universität in Würzburg, Germany, from 1997 to 2000. After that he went to Rutgers, The State University of New Jersey, and graduated with a Master of Science degree in physics in 2001 (Thesis title: *Systolic and Hypersystolic Algorithms for the Gravitational NBody Problem*). His adviser there was David Merritt. From 2001 to 2003 he did research at the Max Planck Institut für Gravitationsphysik, Albert Einstein Institut in Potsdam, Germany, under the supervision of Ed Seidel. In 2003 Ernst Nils Dorband joined the graduate school of Louisiana State University, doing research for his doctoral degree with Manuel Tiglio as his main adviser. Publications include:

- E. N. Dorband, M. Hemsendorf, D. Merritt, *Systolic and Hyper-Systolic Algorithms for the Gravitational N-Body Problem, with an Application to Brownian Motion.* J. Comput. Phys. 185:484-511, 2003
- P. Diener, E. N. Dorband, E. Schnetter, M. Tiglio, *New, Efficient and Accurate High Order Derivative and Dissipation Operators Satisfying Summation by Parts and Applications in Three-Dimensional Multi-Block Evolutions* `arXiv:gr-qc/0512001`, accepted by "Journal of Scientific Computing"
- E. Schnetter, P. Diener, E. N. Dorband, M. Tiglio, *A Multi-Block Infrastructure for Three-Dimensional Time-Dependent Numerical Relativity.* Class,Quant.Grav.23:S553-S578, 2006
- E. N. Dorband, E. Berti, P. Diener, E. Schnetter, M. Tiglio, *Numerical Study of the Quasinormal Mode Excitation of Kerr Black Holes.* Phys.Rev.D74:084028, 2006
- E. Pazos, E. N. Dorband, A. Nagar, C. Palenzuela, E. Schnetter, M. Tiglio, *How Far Away is Far Enough for Extracting Numerical Waveforms, and How Much Do They Depend on the Extraction Method?* `arXiv:gr-qc/0612149`, submitted to "Class,Quant.Grav."